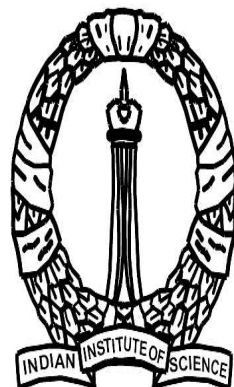


Studies of Static and Dynamic Multiscaling in Turbulence



*A thesis submitted for the degree of
Doctor of Philosophy*
in the Faculty of Science

By
Dhrubaditya Mitra



Department of Physics
Indian Institute of Science
Bangalore - 560 012
India

► *Front-cover figure: Turbulence in West and East.*

The figure on left is a photograph of a page of the diary of Leonardo da Vinci, depicting a turbulent flow. A translation of the text accompanying this picture follows: "Observe the motion of the surface of the water, which resembles that of hair, which has two motions, of which one is caused by the weight of the hair, the other by the direction of the curls; thus the water has eddying motions, one part of which is due to the principal current, the other to random and reverse motion." Quoted from J.L. Lumley, Phys. Fluids. A, 4, 203 (1997).

The figure on the right is a photograph of a Woodblock print by Japanese artist Hokusai. This picture is called "The Breaking Wave Off Kanagawa". Also called "The Great Wave". This print is from Hokusai's series "Thirty-six Views of Fuji". The original is at the Hakone Museum in Japan.

DECLARATION

The work presented in this thesis is original and was done by me at the Department of Physics, Indian Institute of Science, Bangalore, under the guidance of Prof. Rahul Pandit

The thesis has not formed the basis for the award of any degree, diploma, fellowship, associateship or similar title of any university or institution.

Dhrubaditya Mitra

September, 2004

Department of Physics,
Indian Institute of Science,
Bangalore - 560012,
India.

Acknowledgements

This thesis is the end result of works done over last six years. Most of these works have been done jointly with Rahul. He has not only been my thesis advisor, but also a friend and a mentor. Most of the physics I know, I owe to my discussions with him and other members of the theory group. My discussions with Sriram and Chandan have been very useful. I have learnt a lot from the course given by them and also from the courses of BSS, Venkat, and Sanjay Jain. I have learnt all my statistical physics by attending and grading courses given by Rahul, Sriram and BSS. But I have learnt most from my interactions with other students of theory group. Particularly Ashwin, Chinmay, Prabuddha and Pinaki. My first hesitant steps in the "turbulence-land" were guided by Ashwin. Chinmay introduced me to parallel programming and Prabuddha taught me Fortran 90. The tex file of this thesis was made from a template provided by Chinmay. Every discussion with Pinaki, physics or otherwise has been a pleasure, although we rarely concluded. All the past and present members of the theory group, in particular Alex, Anirban, Abhik, Buddho, Ronojoy, Karan, Hassan, Apratim, Toby, Aditi, Pai, Subhra and last but not the least Nandan have been my teachers in some way or the other. At present the young turks Chirag, Smarajit, Shajahan, Debarshini, Vijay and Ganapati are holding fort. Outside the theory group I had fruitful discussions with Debjanis (Pal and Bagchi), Rumi, Rangeet, Kantimoy and Joy. The last two have always been a great sources of inspiration. Discussion with Sitabhra and Abhishek were always useful.

A large part of this thesis is about dynamic multiscaling in fluid turbulence. One of the first ideas which later blossomed into this thesis came out of my discussion with C. Jayaprakash (Ohio University).

A part of the work reported in this thesis was done while I was in Observatoire

de la Cote d'Azur in Nice. Over there my advisor was Uriel Frisch. It was really a fascinating experience to work with Uriel. All I know about Burgers turbulence was taught to me by Uriel and Jeremie (Bec). Uriel also introduced me to the fascinating world of distribution theory. He has influenced directly or indirectly all the major results in this thesis. In Nice I also did some joint work with Thomas Gilbert only a part of which are reported here. I not only learnt a lot of physics out of our collaboration, but also appreciated the Thomas's approach to physics. I wish I could learn more of that from him. The discussion with Massimo Vergasolla and Yannik Ponti are gratefully acknowledged. Special thanks are due to Takeshi (Matsumoto). He not only read my papers with great care, but also gave me pointers to a new and fantastic random number generator. My discussion with Andreii (Sobolebski) were of immense help too.

I would also take this privilege to thank two people I have never met. Steve Johnson and Matt Figo who wrote FFTW and made it freely available to the scientific community.

My research work has been mostly computational in nature. It would have been impossible without active help and advice from our system administrator Srinivas. Several years back Pinaki, Ronojoy and myself started working with Srinivas to manage our collection of PCs, workstations and later clusters. After Ronojoy has left, Smarajit has joined our team. After surviving several crashes and hacking attempts together, Srinivas is now not only my respected colleague but also a dear friend. This thesis owes its existence to his able skills.

Some of my computations were done in SERC. I thankfully acknowledge the help I received from Siddhu and Sujana in the earlier days and later from Dr Lakshmi, Kiran and Deepak.

Ms Shantakumari, Ms Prashanti and the staff in the physics office were forever helpful.

My life in this Institute in particular and in Bangalore in general would have been a dull existence without my family and friends. "Addas" with Malabika, Pinaki, Sitabhra, Joy-Moumita and Kanti-Debjani helped me survive the last three years. *Bordi* was there whenever I needed help. Subhra has always remained a great friend. It was a pleasure to have Niruj and Chaitra around. In more recent days, the new IPhd kids Sumilan, Samriddhi, Purbasha, Sankhasubhra, Debraj and others have kept the atmosphere of Raman Building worth living. In earlier days I spent most of my time with my IPhd class mates: Sandeep, Rangeet, Prabuddha, Pinaki, Subhra, Ayash, Nandan and of course Sundar. And finally I, *ITP*, thank all the other *TPs* for stimulating intellectual discussions in TMSC.

About eight years back Biswajit first showed me the popular science book *Chaos* by James Gleick and raised my curiosity about nonlinear physics. I take this chance to thank him and the other member of *BhaBNa*.

My stay in Nice was made enjoyable by the company of Archana, Andreii, Takeshi and Jeremie. Uriel and Helene made me feel at home in Nice. I thank Mitchell Henon for lending me books from his fantastic collection of science fictions, while I was in Nice. Long walks in the mountains with John may never be forgotten. Secretarial helps of Ms Victorial Pelegrini are gratefully acknowledged.

This thesis would never have been possible without my family's help and support. The thesis really belongs to them. My wife, Malabika, has supported me through thick and thin, in illness and in good health. The encouragement from my parents kept me going through difficult times.

Preface

The physics of turbulence is the study of the chaotic and irregular behaviour driven fluids. It is ubiquitous in cosmic, terrestrial and laboratory environments. To describe how the properties of a simple incompressible fluid it is sufficient to know its velocity at all points in space and as a function of time. The equation of motion for the velocity of such a fluid is the incompressible Navier–Stokes equation. In more complicated cases, for example if the temperature of the fluid also fluctuates in space and time, the Navier–Stokes equation must be supplemented by additional equations. Incompressible fluid turbulence is the study of solutions of the Navier–Stokes equation at very high Reynolds numbers, Re , the dimensionless control parameter for this problem. The chaotic nature of these solutions leads us to characterise them by their statistical properties. For example, statistical properties of fluid turbulence are characterised often by structure functions of velocity. For intermediate range of length scales, that is the *inertial range*, these structure functions show multiscaling. Most studies concentrate on equal-time structure functions which describe the equal-time statistical properties of the turbulent fluid. Dynamic properties can be measured by more general time-dependent structure functions. A major challenge in the field of fluid turbulence is to understand the multiscaling properties of both the equal-time and time-dependent structure functions of velocity starting from the Navier–Stokes equation. In this thesis we use numerical and analytical techniques to study scaling and multiscaling of equal-time and time-dependent structure functions in turbulence not only in fluids but also in advection of passive-scalars and passive vectors, and in randomly forced Burgers equation. The thesis is organised as follows:

- In Chapter 1 we give an overview of the physics of homogeneous and isotropic

turbulence. We describe some of the progresses made in experimental, theoretical and computational studies. We begin by summarising the scaling theory of structure functions, originally proposed by A.N. Kolmogorov in 1941. We further discuss recent experimental and numerical evidence in favour of multiscaling. We give a short introduction to the multifractal model. We also introduce turbulence in the passive-scalar problem and in the Burgers equation.

- In Chapter 2 we present our new results on dynamic multiscaling in fluid turbulence. We show that different ways of extracting time scales from time-dependent velocity structure functions lead to different dynamic-multiscaling exponents in fluid turbulence. These exponents are related to equal-time multiscaling exponents by different classes of bridge relations which we derive. We check this explicitly by detailed numerical simulations of the GOY shell model for fluid turbulence.
- In Chapter 3 we study dynamic multiscaling for passive-scalar and passive-vector turbulence. An example of a passive-scalar field is the temperature field in the fluid, if the gradients of temperature are small, such that the effects of convection in the system are negligible. By using analytical methods, we find simple dynamic scaling for the Kraichnan model for passive scalar advection and also for a Kraichnan-type shell model for passive-scalar turbulence. Although the passive-scalar field in the Kraichnan case is known to show equal-time multiscaling for structure functions, we find simple dynamic scaling of the time-dependent structure function. These results are further supported by our numerical simulations on the shell models. In the Kraichnan model the advecting velocity is a random Gaussian variable which is white-in-time. We also consider a passive-scalar shell model advected by velocity from the GOY shell model of fluid turbulence.

In this case the advecting velocity field is not Gaussian but has multifractal properties and we find dynamic multiscaling for the time-dependent passive-scalar structure functions. We discuss the implication of our study for passive-vector turbulence. We also touch upon the issues of the kinematic dynamo in the context of passive-vector shell models.

- In Chapter 4 we present preliminary results from our study of dynamic multiscaling for time-dependent velocity structure functions obtained from the Navier–Stokes equation. We present the first numerical algorithm for a pseudo-spectral, direct numerical simulation that yields quasi-Lagrangian velocity. We calculate the equal-time, quasi-Lagrangian velocity structure functions from 512^3 and 256^3 , two-third dealiased pseudo-spectral simulations. We also present preliminary data for time-dependent Eulerian and quasi-Lagrangian structure functions.
- In Chapter 5 we study turbulence in the one-dimensional Burgers equation with a white-in-time, Gaussian random force that has a Fourier-space spectrum $\sim 1/k$, where k is the wave number. From very-high-resolution numerical simulations, in the limit of vanishing viscosity, we provide strong evidence for multiscaling of velocity structure functions, as opposed to bifractal scaling suggested by earlier, low-resolution studies. We discuss possible artifacts that can make bifractal scaling appear like genuine multiscaling and show that they are not present in our work. We discuss the implications of our study for multiscaling in fluid turbulence.

Contents

1	Introduction	1
1.1	What is turbulence?	1
1.2	Symmetries of Navier–Stokes equation	3
1.3	Homogeneous and isotropic turbulence	5
1.4	Richardson-Kolmogorov phenomenology of turbulence	8
1.5	Experimental tests of K41	10
1.6	A closer look at K41	13
1.6.1	The velocity correlation function	13
1.6.2	The Zeroth-law of turbulence	14
1.6.3	The Von Kármán–Howarth relation	15
1.7	Multiscaling	16
1.7.1	Experimental evidence of multiscaling	16
1.7.2	Direct numerical simulations	17
1.7.3	Extended Self Similarity (ESS)	17
1.7.4	Multifractal model	18
1.7.5	Exact results on multiscaling	20
1.7.6	She-Leveque formula	21
1.8	Shell models	21
1.9	Passive-scalar turbulence	23
1.9.1	Kraichnan model	24
1.10	Dynamics of turbulence	28

1.10.1	Critical dynamics	29
1.10.2	Time-dependent structure functions	30
1.10.3	Eulerian versus Lagrangian	32
1.10.4	Lagrangian measurements	33
1.11	Burgulence	35
1.11.1	Introduction	35
1.11.2	Basic tools	37
1.11.3	Structure functions	40
1.12	Summary	41
2	The varieties of dynamic multiscaling	49
2.1	Introduction	49
2.2	Dynamic structure functions	52
2.3	Multifractal formalism for dynamic multiscaling	54
2.3.1	Several time-arguments	57
2.4	GOY shell model	58
2.4.1	Multiscaling of equal-time structure functions	58
2.4.2	Extended Self Similarity	59
2.4.3	Time-dependent structure functions	60
2.4.4	Exit-time analysis	61
2.5	Dynamic ESS	69
2.6	Conclusion	69
3	Dynamic scaling and multiscaling in passive-scalar and passive-vector turbulence	75
3.1	Introduction	75
3.2	Kraichnan model (Model A)	79
3.3	Kraichnan type passive-scalar shell model(Model B)	84

3.3.1	Analytical calculation	85
3.3.2	Numerical Simulations	86
3.4	A passive-scalar shell model advected by turbulent velocity field	90
3.4.1	Multifractal analysis	90
3.4.2	Numerical Simulation	93
3.4.3	Derivative time scales	94
3.4.4	Integral time scale	95
3.5	Passive vector models	97
3.6	Conclusion	101
4	Dynamic multiscaling in the Navier–Stokes Equation	115
4.1	Review of earlier studies	116
4.2	Quasi-Lagrangian algorithm	121
4.3	Results	123
4.4	Conclusion and future studies	126
5	Multiscaling in the Stochastically Forced Burgers Equation	139
5.1	Introduction	139
5.2	Review of earlier work	142
5.3	Algorithm and numerical details	147
5.4	Results	152
5.5	Tests of multiscaling	153
5.5.1	Von Kármán–Howarth relation	153
5.5.2	Log-corrected bi-fractality ?	154
5.5.3	Steady-state or transients ?	155
5.5.4	Slowly-receding bifractality ?	156
5.6	Consequences of multiscaling	156
5.7	Conclusion	158

A Adams-Bashforth scheme of integration	179
B Numerical scheme for the Kraichnan shell model	181
C Gaussian averaging of stochastic differential equations	185
D Von Kármán–Howarth relation in Kicked "Burgulence"	189

Chapter 1

Introduction

1.1 What is turbulence?

The flow of fluids, in particular water, is a fascinating subject. We have all watched with amazement complicated flow patterns in streams, waterfalls, and whirlpools. When a flow pattern looks irregular and chaotic we call it *turbulent*. From our experience we know that a turbulent flow generally consists of many vortices, big and small, which form and disappear in the course of time. Hence, as physicists, we expect the physics of turbulence to be a *many-body phenomenon*.

To describe the motion of a fluid mathematically we must give its properties at every point in space. For example, at different places the fluid is moving with different velocities. The velocity, however, is not the only property that the fluid has, which varies from point to point. Other such quantities are pressure, density and temperature. If the velocity of the fluid is much less than the velocity of sound in the fluid medium, the fluid is practically *incompressible*. For an incompressible fluid, the density does not vary from one place to another. The flow of such a fluid is described by the Navier–Stokes equation:

$$\frac{\partial \vec{u}}{\partial t} + (\vec{u} \cdot \vec{\nabla}) \vec{u} = \nu \nabla^2 \vec{u} + \vec{\nabla} p + \vec{f}; \quad (1.1)$$

where we use units in which the density $\rho = 1$, the Eulerian velocity at point \vec{x} and time t is $\vec{u}(\vec{x}, t)$, the kinematic viscosity is ν , the pressure is p , and \vec{f} denotes an

external body force (per unit volume) imposed on the fluid. The incompressibility condition is enforced by:

$$\nabla \cdot \vec{u}(\vec{x}, t) = 0, \quad (1.2)$$

which can be used to eliminate the pressure from Eq. (1.1). Equations (1.1) and (1.2) shall together be referred to as the *incompressible Navier–Stokes* equation.

If the temperature variation from one point of the fluid to another is not large, the flow of the fluid is, to a first approximation, not influenced by the temperature. But the temperature is indeed advected by the flow. In such a case the temperature is called a *passive-scalar*. Other examples of passive-scalar includes pollutants or dyes being advected by the fluid. The chaotic and irregular variation of such an advected passive-scalar as a function of space and time is called passive-scalar turbulence.

In addition, the fluid may also be a conductor and carry an electric current whose density varies from point to point in magnitude and direction. There are interesting phenomenon where currents and magnetism play an important role in determining the behaviour of the fluid; this subject is called *magnetohydrodynamics*.

In this thesis we shall be primarily interested in turbulence as described by the incompressible Navier–Stokes equation (Chapters 2 and 4). We shall also discuss passive-scalar turbulence in Chapter 3. Turbulence in the Burgers equation, or the study of random solutions of the Burgers equation, will be discussed in Chapter 5.

In the remaining part of this Chapter we shall give a short introduction to those aspects of turbulence which have a direct bearing on the problems we address. In particular, we shall introduce elementary symmetries of the Navier–Stokes equations and thence the Reynolds number, some notions about and statistical properties of homogeneous, isotropic fluid turbulence, such as the Richard-

son cascade, the Kolmogorov scaling of velocity structure functions, and the subsequent elucidation of their multiscaling. The relation of such multiscaling with multifractal behaviour will also be explored particularly with a view to its implications for time-dependent structure functions.

A more detailed accounts of *homogeneous and isotropic* turbulence are available in the books by Frisch [1], Bohr, Jensen, Paladin, and Vulpiani [2], and the classic texts by Batchelor [3] and by Monin and Yaglom [4].

1.2 Symmetries of Navier–Stokes equation

We take our first steps in turbulence by examining the symmetries of the Navier–Stokes equation. In this Section we follow Ref [1] closely.

By symmetries we mean any discrete or continuous invariance groups of a dynamical theory. Let \mathbf{G} denote a group of transformations acting on space-time functions $\vec{u}(\vec{x}, t)$, which are divergence-less. We also assume periodic boundary conditions over a cubic box of side L . Then \mathbf{G} is said to be the symmetry group of the Navier–Stokes equation if, for all $\vec{u}(\vec{x}, t)$ s that are solutions of the Navier–Stokes equation, and all $g \in \mathbf{G}$, the function $g\vec{u}(\vec{x}, t)$ is also a solution.

A look at the Navier–Stokes equation convinces us that space and time translation falls within the symmetry group of the equation. So do Galilean transformations. This just means that the phenomenon of fluid turbulence does not change when viewed from a uniformly moving frame. We shall have more to say about Galilean transformations later. Invariance under parity(i.e. space inversion) holds only if the non-linear term is neglected. Rotational invariance is not consistent with our boundary condition unless we take the limit $L \rightarrow \infty$. All the above symmetries are just macroscopic consequence of the basic symmetries of Newton’s equation governing microscopic molecular motion (in the classical approximation).

One additional symmetry particular to this equation is invariance under the following scaling transformations:

$$g_{\lambda}^{\text{scal}} : t, \vec{x}, \vec{u} \mapsto \lambda^{(1-h)}t, \lambda\vec{x}, \lambda^h\vec{u}, \quad \lambda \in \mathbb{R}_+, h \in \mathbb{R} \quad (1.3)$$

Under scaling, t is changed into $\lambda^{1-h}t$, \vec{x} is changed to $\lambda\vec{x}$, and \vec{u} to $\lambda^h\vec{u}$, so all the terms in the Navier–Stokes equation are multiplied by λ^{2h-1} except the viscous term which is multiplied by λ^{h-2} . Thus, for a finite viscosity, only $h = -1$ is permitted. This symmetry tells us that we can combine the viscosity, the characteristic length (say L) and the characteristic velocity (say V) of the flow to construct a dimensionless control parameter, the Reynolds number, which is

$$\text{Re} \equiv \frac{LV}{\nu}. \quad (1.4)$$

And two flows with the same Reynolds number are just scaled versions of each other. This is the well-known *similarity principle* of fluid dynamics. The Reynolds number measures how large is the effect of nonlinear term compared to the viscous dissipation in a particular flow. For high Reynolds numbers the solutions are strongly affected by the nonlinearity, and the actual flow pattern is *turbulent*.

For example, consider a flow parallel to the x -axis, incident from the left on a cylinder (infinite in the z direction), of circular cross-section, as sketched in Fig (1.1). Here the characteristic length can be taken to be the diameter of the cylinder; and the velocity of the fluid far away from the cylinder is taken to be the characteristic velocity of the flow. The space-time nature of the flow is determined by the Reynolds number alone. At low Reynolds numbers the velocity at any point in space is constant in time. This is called a *laminar* flow [Fig. (1.2)]. As the Reynolds number increases the flow velocity becomes more and more chaotic in both space and time [Fig. (1.3)]. This qualitative phenomenon is true for all flows obeying the incompressible Navier–Stokes equation, although different flows remain laminar up to vastly different Reynolds number. At very high

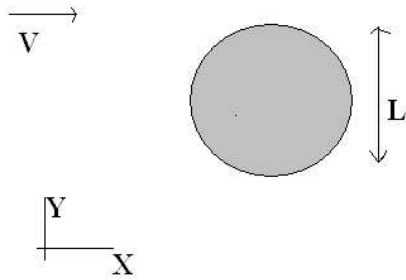


Figure 1.1: A schematic diagram showing a flow about a cylinder infinite in z direction. The velocity far away from the cylinder is $(V,0,0)$.

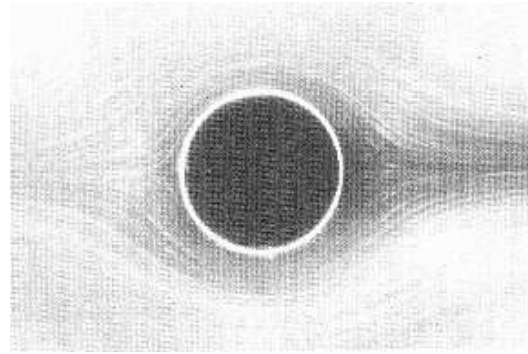


Figure 1.2: Laminar flow about a cylinder for the geometry sketched in Fig. (1.1). At any point in space the flow-velocity is constant in time. Photo taken from Ref. [5]. ($Re = 0.16$)

Reynolds numbers the fluid velocity is a rapidly changing function of space and time, and the flow is called *turbulent*. The subject of turbulence is the study of flows at high Reynolds numbers. Let us note here that randomness of the flow at high Reynolds number does not come from randomness in the initial condition or randomness in the forcing. The randomness is generated by the nonlinearities of the Navier–Stokes equation.

1.3 Homogeneous and isotropic turbulence

Next we introduce the notion of homogeneous and isotropic turbulence. By homogeneous turbulence we mean turbulent motion whose statistical properties are independent of position in the fluid. We quote from the classic book by Batchelor [3] on homogeneous turbulence:

” The conception of homogeneous turbulence is idealised, in that there is no known method of realising such a motion exactly. The various methods of producing turbulent motion in a laboratory or in nature all involve discrimination between different parts of the position. However, in certain circumstances this departure from exact independence of position can be made very small, and it is

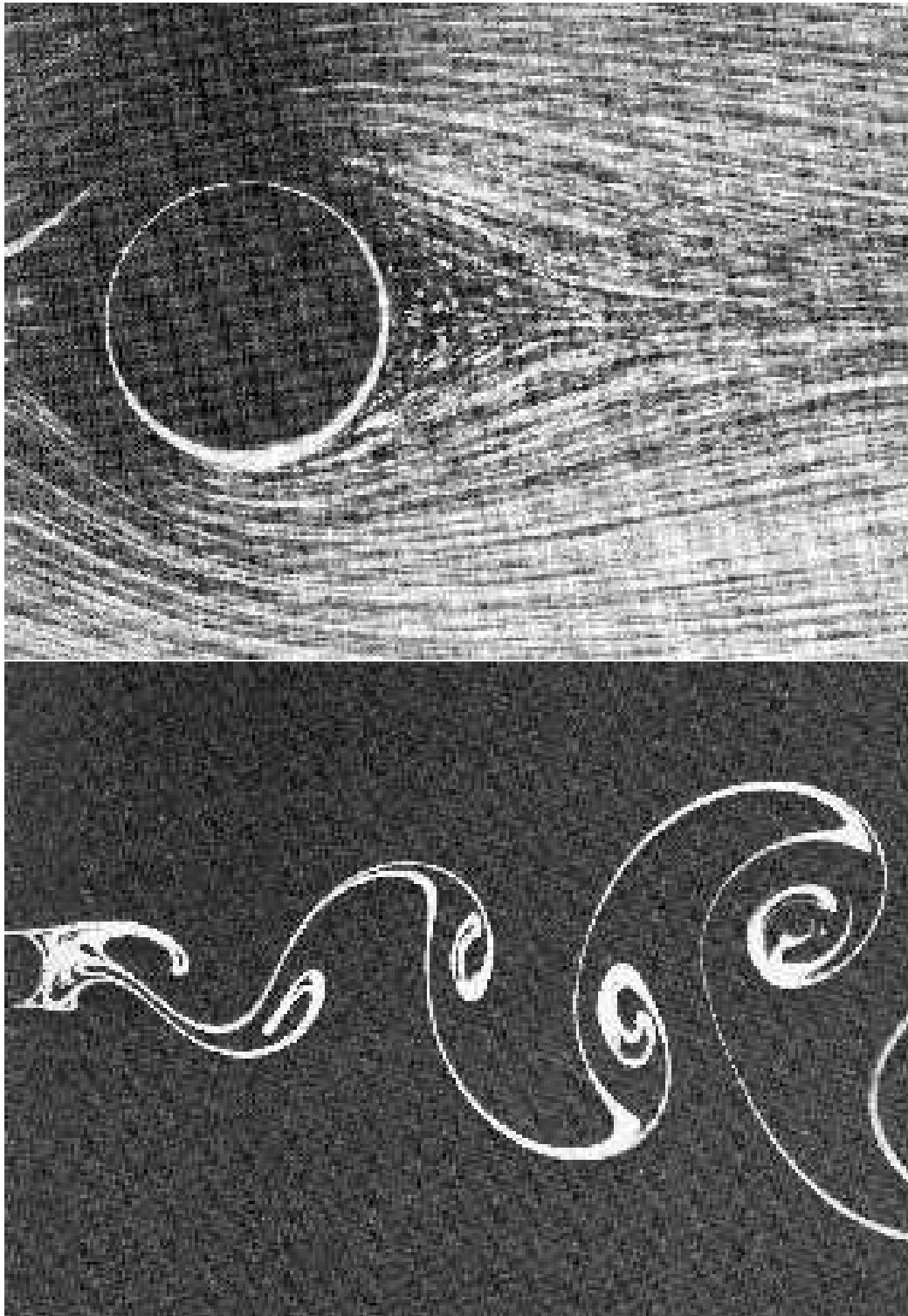


Figure 1.3: Flow about a cylinder for the geometry sketched in Fig. (1.1). The top picture is for $Re = 9.6$ and the bottom one for $Re = 140$. Observe how the chaotic nature of the flow develops with increasing Reynolds number. Compare with Fig. (1.2). Photograph taken from Ref. [5].

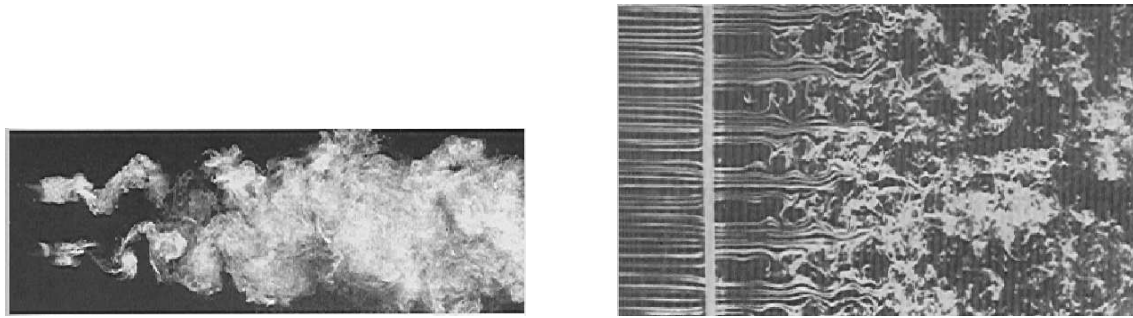


Figure 1.4: The picture on left shows flow behind two cylinders. The picture on right shows flow behind a grid, which is an array of cylinders. This experimental situation comes quite close to homogeneous turbulence as described in text. Photo taken from Ref [5].

possible to get a close approximation to the homogeneous turbulence. It has been found, for instance, that if a uniform stream of fluid passes through a regular array of holes in a rigid sheet, or a regular grid of bars, held at right angles to the stream, the motion downstream of the sheet consists of the same uniform velocity together with a superimposed random distribution of velocity. This random motion dies away with distance from the grid, and to that extent is not statistically homogeneous, but the rate of decay is found to be so small that the assumption of homogeneity of turbulence is valid for most purposes. Thus there is available a convenient laboratory method of producing turbulence which is approximately homogeneous,..... The possibility of carrying out controlled and accurate experiments rapidly has permitted a very fruitful combination of experimental and theoretical research. ”

Figure (1.4) illustrates the experimental situation described by Batchelor. In addition, if we consider ourselves in a frame moving with the mean velocity of the flow, we should observe homogeneous isotropic turbulence. By isotropic we mean that the statistical properties of velocity difference across a length $\vec{\ell}$ depends only on the magnitude of $\ell = |\vec{\ell}|$. This kind of turbulence is also the easiest to study numerically. We shall later discuss in detail direct numerical simulations (DNS for short) of homogeneous, isotropic turbulence in a periodic box.

1.4 Richardson-Kolmogorov phenomenology of turbulence

One of the earliest insights into to the physics of turbulence was obtained by the meteorologist Lewis Fry Richardson: He proposed, what is now known as the cascade picture of turbulence. In this picture the largest eddies¹ in the system are created by instabilities of the mean streamline flow. Examples of large eddies include hurricanes in the atmosphere. They decay giving eddies of smaller size which are also unstable. These in turn decay to even smaller eddies, and so on until the very small stable eddies decay because of viscous damping, converting their energy into heat. From the Navier–Stokes equation it is easy to see that viscous damping is most effective at the smallest length scales as we show below.

This qualitative picture forms the basis of Kolmogorov's [6] *idea of universality* (published in 1941, this theory, which is still the backbone on which modern theories of turbulence are built, shall henceforth be referred as K41). The central idea is that, at very high Reynolds numbers there is a wide separation of spatial scales between the scale of energy input (the scale of the largest eddies i.e. L) and the scales at which energy dissipation becomes significant (say η). Thus one might expect that the statistical properties in the intermediate region, called the *inertial range*, could be *universal*. In a statistically stationary state the rate of energy input is equal to the rate of energy dissipation (say ϵ). It is also equal to the flux of energy through the inertial range. (We have to assumed implicitly that ϵ remains finite as we let the viscosity become very small, or the Reynolds number to become very large.) It is useful to define the order- p , equal-time, longitudi-

¹The concept of *eddy* is often used in phenomenology of turbulence. An "eddy" of size ℓ can be loosely described as the velocity in the Fourier mode with wave-vector $q \sim 1/\ell$.

nal, velocity structure functions,

$$\mathcal{S}_p(\ell) \equiv \langle [\delta \mathbf{u}_{||}(\vec{x}, \ell)]^p \rangle, \quad (1.5)$$

$$\delta \mathbf{u}_{||}(\vec{x}, \ell) \equiv [\vec{\mathbf{u}}(\vec{x} + \vec{\ell}, t) - \vec{\mathbf{u}}(\vec{x}, t)] \cdot \left(\frac{\vec{\ell}}{\ell}\right), \quad (1.6)$$

where the angular brackets denote an ensemble averaging, i.e., an averaging over many statistical realisations of the turbulent velocity field. The concept of universality implies that $\mathcal{S}_p(\ell)$ does not depend on the parameters L and η , for lengths $\eta \ll \ell \ll L$. This assumption means that ℓ is the only available length-scale for the development of dimensional analysis. In addition we one other parameter the ϵ . Simple dimensional analysis then yields

$$\mathcal{S}_p(\ell) \sim (\epsilon \ell)^{\zeta_p^{\text{K41}}}, \quad (1.7)$$

with the K41 exponents

$$\zeta_p^{\text{K41}} = \frac{p}{3}. \quad (1.8)$$

In particular, this theory predicts,

$$\mathcal{S}_2(\ell) \equiv \langle [\delta \mathbf{u}(\vec{x}, \ell)]^2 \rangle \sim (\epsilon \ell)^{2/3}, \quad (1.9)$$

the celebrated *two-thirds law*. The two-thirds law is equivalent to the statement that the shell-averaged energy spectrum in Fourier space $E(k)$ follows²

$$E(k) \sim k^{-5/3}, \quad (1.10)$$

Fourier mode k in inertial range. The usual correspondence between real space and Fourier space tells us that the dissipation range lies at large k and the forcing scales are restricted to small k .

K41 also predicts the range of length scale over which scaling is supposed to hold. The length scale at which viscosity becomes important should be given by

$$\eta \sim \left(\frac{\nu^3}{\epsilon}\right)^{1/4} \quad (1.11)$$

²The Fourier space is of course three dimensional, and energy is a function of the three dimensional vector Fourier mode \vec{q} . $E(k)$ is the energy averaged over all the Fourier modes for which $|\vec{q}| = k$, i.e., averaged over a shell in Fourier space.

This result follows simply by balancing the advection term $\vec{u} \cdot \nabla \vec{u}$ with the viscous term $\nu \nabla^2 \vec{u}$ and using the K41 result $\langle \delta u(\ell) \rangle \sim \ell^{1/3}$. Hence in real space structure functions are expected to show K41 scaling behaviour if $\eta \ll \ell \ll L$; in Fourier space this inertial range is $k_0 \ll k \ll k_d$, here $k_0 \simeq 1/L$, and $k_d = 1/\eta$.

In the next section we compare the predictions of K41 against experimental measurements.

1.5 Experimental tests of K41

Experimental measurements of structure functions to verify the predictions of K41 started almost immediately after this theory was proposed. Early measurements were made on ocean currents and atmospheric turbulence by the Russian school [4]. Modern experimental techniques have yielded data of much better quality. When we consider such experiments we must keep in mind the following important issues:

1. The Reynolds numbers in such experiments should be high to obtain reliable measurements for the exponents ζ_p . The higher the Reynolds number the longer is the inertial scaling range, and the better the estimates for the exponents ζ_p .
2. Lack of perfect homogeneity and isotropy, especially at large length scales, complicates data analysis in very-high-Reynolds-number experiments. Examples of such experiments include atmospheric flows [7] and flows of normal (not superfluid) liquid helium.
3. It is difficult to measure the velocity of the fluid at several different points simultaneously. Experiments are typically done by measuring the time-series of the velocity at one point in the flow. Temporal separations, τ , are then converted to spatial separations, ℓ , by using the mean velocity, u_{mean} of the

flow: $\ell = u_{\text{mean}}\tau$. This is justified by invoking the *Taylor frozen-flow hypothesis*: If the mean flow velocity is so large that eddies of size ℓ do not decay appreciably in the time they take to flow past the probe, then no significant error is made in measurements of the equal-time structure functions up to length-scale ℓ . This linear relation between length and time scales that underlie the Taylor hypothesis will be discussed later in this thesis in the context of dynamic multiscaling.

4. Complications arising from lack of isotropy or the use of the Taylor hypothesis do not arise in direct numerical simulation (DNS) of Navier–Stokes equation with periodic boundary conditions. We shall discuss DNS in great detail later. Here it suffices to mention that even the best DNS of the Navier–Stokes equation can achieve only moderately high Reynolds numbers with great difficulty. Reynolds numbers achieved in experiments are at least one order of magnitude higher than the highest Reynolds number achieved so far in DNS. Of course, much higher Reynolds numbers can be obtained in astrophysical setting. The highest Taylor microscale Reynolds number³ achieved in DNS of homogeneous isotropic turbulence is 732 with 2048^3 number of grid points [8].

With the above mentioned complications in mind, let us look at measurements done in the S1 wind tunnel of ONERA⁴. A schematic diagram of the wind tunnel is given in Fig. (1.5). A hot-wire probe is suspended near the point marked 'M'. It recorded the streamwise (parallel to the mean flow) component of the velocity. The averaging is over time which, assuming ergodicity, should yield the same results as an ensemble average. The Reynolds number is around 10^7 . In Fig. (1.6) we show a log – log plot of the second order structure function, obtained from

³see page 13 for definition

⁴All the data quoted from S1 wind tunnel of ONERA are reproduced from Ref [1].

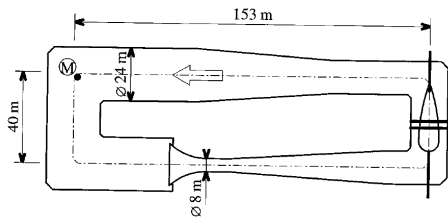


Fig. 5.2. The S1 wind tunnel of ONERA.

Figure 1.5: A schematic diagram, after Ref. [1], showing the S1 wind-tunnel of ONERA. Velocity measurements are made by a hot-wire probe suspended at the point marked M in the diagram. The data collected in the temporal domain was converted to the spatial domain via the Taylor hypothesis.

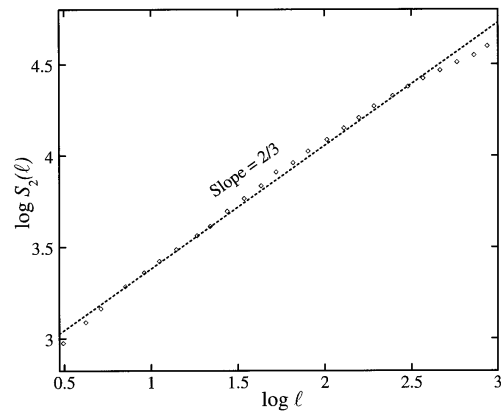


Figure 1.6: A log – log plot of the second order structure function in the time domain for data from S1 wind tunnel of ONERA. Note that the scaling range with scaling exponent of $2/3$ extends for about a decade of length scales.

the wind tunnel S1. For a moderately large scaling range the scaling exponent seems to be quite close to $2/3$.

Although the two-thirds law seems to be plausible from the measurements made in S1 wind tunnel of ONERA, it is certainly not proved beyond doubt. More careful experiments particularly for higher values of p , showed appreciable departures from the predictions of K41. But the measurements of higher order structure functions are quite difficult because they require accurate measurements involving the tail of the probability distribution function for the velocity differences.⁵ The first few experiments which gave convincing proof of deviation of ζ_p values for K41 predictions were done by Anselmet, Gagne, Hopfinger

⁵Let us mention here that there is no a priori evidence that structure functions exists for all values of p . This depends on the shape of the tail of the probability distribution function. Experimental evidence indicates an exponentially decaying tail, which guarantees existence of structure function values for all positive p . But the evidence is far from conclusive.

and Antonia [9]. Their experiments, and more recent ones indicate ζ_p is a convex non-linear function of p . This phenomenon is called *multiscaling*.

Before turning to a detailed discussion of multiscaling and related phenomenon of multifractality, it is useful to have a second look at K41.

1.6 A closer look at K41

In view of the fact that experimental results do not support the K41 theory very strongly, we take a more critical look at it.

1.6.1 The velocity correlation function

We start with the spatial correlation function of the longitudinal component of the velocity define by

$$R(r) \equiv \langle u_{\parallel}(\vec{x})u_{\parallel}(\vec{x} + \vec{r}) \rangle. \quad (1.12)$$

A schematic plot of $R(r)$ is shown in Fig. (1.7). The integral scale can be defined by

$$L \equiv \frac{1}{R(0)} \int_0^{\infty} R(r) dr, \quad (1.13)$$

where the statistical quantities are non-universal and depend on the exact way in which the fluid is forced. The inertial range extends between this integral scale and the dissipation scale. The Taylor-micro-scale is defined by the radius of curvature of $R(r)$ at $r = 0$,

$$\lambda \equiv \left[\frac{1}{R(0)} \frac{\partial^2 R}{\partial r^2} \Big|_{r=0} \right]^{-1/2}. \quad (1.14)$$

From this we can define the oft-used Taylor-micro-scale Reynolds number,

$$Re_{\lambda} \equiv \frac{\lambda u_{rms}}{\nu}, \quad (1.15)$$

where u_{rms} is the root-mean-square velocity of the turbulent flow. It has been shown from experiments and DNS studies that $Re_{\lambda} \sim \sqrt{Re}$, for large values of Re .

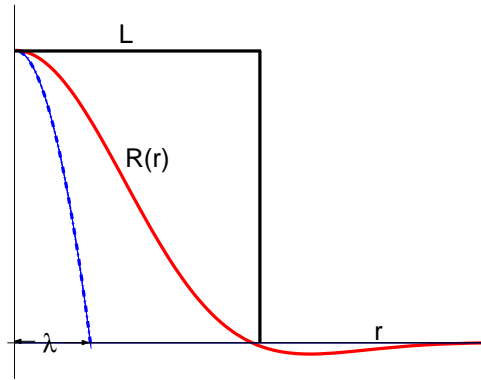


Figure 1.7: A schematic plot of spatial correlation function $R(r)$ of longitudinal component of velocity. The figure schematically show the integral scale L and the Taylor-micro-scale λ .

1.6.2 The Zeroth-law of turbulence

The energy dissipation at a point \vec{x} in the fluid is

$$\epsilon(\vec{x}) = \nu \left[\frac{\partial u_i}{\partial x_j} + \frac{\partial u_j}{\partial x_i} \right]^2, \quad (1.16)$$

where we sum over the repeated indices. One of the fundamental hypotheses used in the K41 theory is that the mean value of $\langle \epsilon \rangle$ remains finite even when the viscosity $\nu \rightarrow 0$. This implies that the non-dimensionalised mean dissipation

$$\frac{\langle \epsilon \rangle L}{u} \rightarrow C \quad \text{as} \quad Re_\lambda \rightarrow \infty, \quad (1.17)$$

where C is an order-unity, universal constant independent of the type of the flow⁶. Experimental results in support of this hypotheses have been collected in Ref. [10]. The results indicate that, irrespective of the type of flow Eq.(1.17) seems to hold if Re_λ is large enough; but the value of Re_λ after which Eq.(1.17) holds is different for different flows. Direct numerical simulation of homogeneous isotropic turbulence with 2048^3 grid points[11], also supports Eq.(1.17), the value of C is close to 0.7.

We call this postulate of K41 the *zeroth law of turbulence*. In the language of field theory this is called *dissipative anomaly*.

⁶In experiments the mean flow velocity is often used in the place of u in Eq.(1.17). In DNS u_{rms} is used.

At present this postulate seems to be absolutely necessary in making an attempt to understand the scaling behaviour of structure functions. A proof of this law from Navier–Stokes equation, when found, is going to be one of the cornerstones of the theory of turbulence. In turbulence in Burgers equation (discussed later) the analogue of zeroth law of turbulence is easily proved (Section 1.11.2).

1.6.3 The Von Kármán–Howarth relation

In addition K41 uses the postulate that, in fully developed turbulence, all the possible symmetries of the Navier–Stokes equation, usually broken by the mechanism producing turbulence, are restored in statistical sense at small scales (i.e. in the inertial and dissipative range) and away from the boundaries. It also assumes that, in this limit, the turbulent flow is self-similar and a scaling exponent h exists, and all the structure functions exists.

To set up a non-equilibrium statistically stationary turbulent state in the Navier–Stokes equation, we have to supply energy at some large spatial length scale to balance the dissipation that is important at small scales. This is modelled by a random stirring force in Eq.(1.1). We assume that, this random stirring force $\vec{f}(\vec{x}, t)$ is stationary, homogeneous (in a statistical sense), and white-in-time. This is the *randomly forced Navier–Stokes equation* . With the additional assumption of isotropy one can prove (see Ref. [1] for a detailed calculation) that,

$$\mathcal{S}_3(\ell) = -\frac{4}{5}\epsilon\ell. \quad (1.18)$$

Or in other words $\zeta_3 = 1$. This is called the *Kolmogorov four-fifths law*, alternatively von Kármán–Howarth relation.

The importance of this law to turbulence research cannot be overstressed. This is one of the few exact relations in turbulence. Experimentalists use this to check the quality of their data and, in particular experimentalists often define the inertial range to be the range of length scales over which $\zeta_3 = 1$. This is also the

basis of a novel way of measuring the exponent ratios ζ_p/ζ_3 as we describe in our discussion of extended self similarity (ESS) later.

In conclusion, we note that, although simple K41 mono-scaling and the two-third law may have corrections, the zeroth law of turbulence and the Kolmogorov four-fifth law need to be include in any future theory of turbulence which aims to explain the scaling behaviour of structure functions.

1.7 Multiscaling

We now give a brief overview of the multiscaling of structure functions in fluid turbulence. All the problems we study in this thesis elucidate different aspects of such multiscaling.

1.7.1 Experimental evidence of multiscaling

In Sec. 1.5 we have already commented on the difficulties involved in accurate measurements of the exponents ζ_p . When it was first observed that $\zeta_p \neq \zeta_p^{K41}$, especially for $p > 3$; two schools of thoughts were developed.

1. The first school argued that the K41 results for ζ_p would be recovered in the limit of $Re \rightarrow \infty$.
2. The second school of thought, which seems to be widely accepted now, is that even at infinite Reynolds number the structure functions show multiscaling.

One of the most convincing pieces of experimental evidence in support of multiscaling was obtained from measurements on atmospheric turbulence in Ref. [7]. Here the Taylor microscale Reynolds number was close to 15,000. The authors showed that the third-order longitudinal structure function obeys scaling with a scaling exponent of unity over more than a decade of length scales. The ζ_p exponents extracted using ESS (see below), also indicated that multiscaling holds

1.7.2 Direct numerical simulations

As early as 1949, J. Von. Neumann [12] suggested that turbulence should be simulated numerically. Direct Numerical Simulation, DNS for short, of homogeneous isotropic turbulence really took off with the work of Orszag and Patterson [13]. on pseudo-spectral DNS. We shall discuss techniques of DNS later in this thesis. The book by Pope [14] also provides a very useful introduction. Let us mention here that to reach high Reynolds numbers high numerical resolution is needed, and, consequently, the numerical difficulties of DNS grows as $Re^{9/4}$. At present the largest Reynolds number reached is 732 in a DNS with 2048^3 Fourier modes by Kaneda et al [11], in the *Earth Simulator*. The same group also did DNS with 4096^3 Fourier modes but the computation was so slow that they failed to get well-averaged data. Notwithstanding the advances made in this area, DNS has been able get a scaling range of at most decade for the shell-averaged energy spectrum. For real-space structure functions, DNS show almost no scaling range. It would have been impossible to conclude anything about multiscaling of structure functions for DNS, had it not been for the useful technique of extended self similarity.

1.7.3 Extended Self Similarity (ESS)

In 1993 the authors of Refs. [15, 16] plotted order- p structure functions as a function of S_3 [S_3 enjoys a special status among all the structure functions, as it follows the von Kármán–Howarth relation, Eq. (1.18).], and obtained a much larger inertial range than in plot of $S_p(r)$ versus r . This phenomenon, which is widely used to find the exponents, is called *extended self similarity (ESS)*. Strictly speaking the slopes of the ESS plots in the extended inertial range yield the exponent ratios ζ_p/ζ_3 ; moreover, since $\zeta_3 = 1$, this is equivalent to finding ζ_p . At present there is no theoretical understanding about why the use of ESS gives an extended scaling

range. If the ESS results are believed, then we find clear evidence of multiscaling.

1.7.4 Multifractal model

Now we take the point of view that there is enough experimental evidence in support of the multiscaling of velocity structure functions, We therefore give a very brief description of those parts of the multifractal model which are directly relevant to the results present in Chapter 2 and 3 of this thesis. Our description of the model follows closely Chapter 8 of Ref. [1].

We start by noticing that, in general, simple scaling trivially implies global scale-invariance and which implies an underlying fractal characteristic. For example, it is now well studied and well understood that the spin-spin correlation function in a two-dimensional Ising model near its critical point shows scaling behaviour. This implies that, near the critical point the up-spin and down-spin regions form fractal clusters. The scaling behaviour is generally cutoff at large length scales, where the fractal clusters reach sizes comparable to the system size, and also for small length scales close to the lattice spacing.

Multiscaling, as observed in turbulence, implies the breakdown of this global scale invariance. For example, assume that there are two interwoven fractal sets \mathcal{S}_1 and \mathcal{S}_2 , with fractal dimensions D_1 and D_2 respectively, embedded in \mathbb{R}^3 . Assume further that the turbulent velocity fluctuation, at point \vec{r} across length scale ℓ , $\delta u_{\vec{r}}(\ell)$ has a scaling exponent h_1 (or h_2) if \vec{r} belongs to \mathcal{S}_1 (or \mathcal{S}_2). The probability $p_1(\ell)$ that a ball of radius ℓ centred at a point \vec{r} , which is uniformly randomly distributed in three dimensional space, will intersect a structure of fractal dimension D_1 is

$$p_1(\ell) \propto \ell^{3-D_1}. \quad (1.19)$$

Hence the order- p velocity structure function,

$$S_p(\ell) \sim \mu_1 \left(\frac{\ell}{\ell_0}\right)^{ph_1} \left(\frac{\ell}{\ell_0}\right)^{3-D_1} + \mu_2 \left(\frac{\ell}{\ell_0}\right)^{ph_2} \left(\frac{\ell}{\ell_0}\right)^{3-D_2} \quad (1.20)$$

where μ_1 and μ_2 are order unity constants. Thus all the structure functions consists of superposition of two power-laws. In the inertial range, i.e. for $\frac{\ell}{\ell_0} \rightarrow 0$ the smallest exponent will dominate. Hence we have

$$\zeta_p = \min(ph_1 + 3 - D_1, ph_2 + 3 - D_2) \quad (1.21)$$

As an illustration consider $D_1 = 3, h_1 = 1/3, 0 < D_2 < 3$ and $h_2 = 1/3 - (3 - D_2)/3$. Then we have

$$\begin{aligned} \zeta_p &= \frac{p}{3}; & \text{for } 0 \leq p \leq 3 \\ &= \frac{p}{3} + \frac{3 - D_2}{1 - p/3}; & \text{for } p \geq 3 \end{aligned} \quad (1.22)$$

Here the parameters have been chosen in such a way that $\zeta_3 = 1$. This behaviour of the multiscaling exponents is called *biscaling*, and the underlying fractal nature is called *bifractal*. In Section(1.11.3) we shall show how bifractality appears in Burgers equation.

Now we take bifractality a step further and assume that the turbulent flow possesses a range of scaling exponents $I = (h_{\min}, h_{\max})$. For each h in this range there is a set $\mathcal{S}_h \subset \mathbb{R}^3$ of fractal dimension $D(h)$, such that as $\ell \rightarrow 0$,

$$\frac{\delta u_{\vec{r}}(\ell)}{u(0)} \left(\sim \frac{\ell}{\ell_0} \right)^h, \quad \vec{r} \in \mathcal{S}_h. \quad (1.23)$$

The exponents h_{\min} and h_{\max} and the function $D(h)$ are postulated to be universal. From this multifractal assumption we obtain the following expression for the structure function

$$\frac{S_p(\ell)}{u^p(0)} \sim \int_I d\mu(h) \left(\frac{\ell}{\ell_0} \right)^{ph+3-D(h)}. \quad (1.24)$$

The above equation is an obvious generalisation of Eq.(1.20). In the limit of $\frac{\ell}{\ell_0} \rightarrow 0$ the power-law with the smallest exponent dominates and we obtain by a steepest descent calculation,

$$\lim_{\ell \rightarrow 0} \frac{\ln S_p(\ell)}{\ln \ell} = \zeta_p \quad (1.25)$$

where

$$\zeta_p = \inf_h [ph + 3 - D(h)]. \quad (1.26)$$

Moreover, there is an additional constraint due to von Kármán–Howarth relation, namely,

$$\zeta_3 = \inf_h [3h + 3 - D(h)] = 1 \quad (1.27)$$

Up to this point the multifractal model just helps in systematising the multiscaling exponents of fluid turbulence. In the next step one uses both the multifractal model and K41 theory to make predictions about other aspects of fluid turbulence. We can then compare those predictions with experiments and direct numerical simulations (DNS) and see whether the K41 phenomenology or the multifractal analysis yields the correct results. In most cases the prediction of K41 and the multifractal model differs for quantities which corresponds to the tail of the PDF of velocity differences (for example higher-order multiscaling exponents), and hence are difficult to measure. One particularly interesting phenomenon is the dynamic scaling of unequal-time structure functions (see Section 1.10), in which case the prediction of the multifractal model are significant for small values of order- p . This is discussed in detail in this thesis in Chapters 2,3 and 4.

1.7.5 Exact results on multiscaling

And finally we list some *exact* relations the multiscaling exponents should satisfy. Consider the two following hypotheses:

1. The leading behaviour of order- p structure functions, in the limit of infinitely large Reynolds number, is power-law scaling with exponent ζ_p .
2. For finite Reynolds number the scaling behaviour holds as intermediate asymptotics over a range of scales,

Using these the following can be proved [1]:

1. Convexity inequality : For any three positive integers $p_1 \leq p_2 \leq p_3$,

$$(p_3 - p_1)\zeta_{2p_2} \geq (p_3 - p_2)\zeta_{2p_1} + (p_2 - p_1)\zeta_{2p_3}. \quad (1.28)$$

2. If there exist two consecutive even number $2p$ and $2p + 2$ such that

$$\zeta_{2p} > \zeta_{2p+2}, \quad (1.29)$$

then the velocity of the flow (measured in the reference frame of the mean flow) cannot be bounded.

1.7.6 She-Leveque formula

The vorticity defined by

$$\vec{\Omega} = \vec{\nabla} \times \vec{u} \quad (1.30)$$

plays a crucial role in the phenomenology of turbulent flows [1]. In DNS studies of fluid turbulence the vorticity field is often determined from the velocity field and iso- $|\Omega|$ plots are made. These plots show typical filamentary structures. These filaments are observed in experiments too [17]. By using a phenomenological model based on these filamentary structure, She and Leveque [18] proposed the following formula for the equal-time multiscaling exponents:

$$\zeta_p = \frac{p}{9} + 2 \left[1 - \left(\frac{2}{3} \right)^{p/3} \right]. \quad (1.31)$$

This formula agrees remarkably well with experimentally obtained values of ζ_p at least up to $p = 8$. We shall often use values for ζ_p from this formula as a convenient parametrisation of experimental results.

1.8 Shell models

Given the fact that DNS and experiments have still been unable to see large enough scaling range for equal-time structure functions, it is useful to work with

simplified models that are physically motivated and capture as many aspects of fluid turbulence as possible. Though such models must, perforce, make several approximations they can allow us to explore large Reynolds number regime and consequently shows much more scaling range for the equal-time structure functions. The most successful models of this type are *shell models*. To understand them better let us first write down incompressible Navier–Stokes equation in Fourier space:

$$[\partial_t + \nu k^2] \tilde{u}_l(\vec{k}, t) = ik_m P_{lj}(\vec{k}) \int_{\vec{p}+\vec{q}=\vec{k}} \tilde{u}_j(\vec{p}, t) \tilde{u}_m(\vec{q}, t) d\vec{p} + \tilde{f}_l(\vec{k}, t), \quad (1.32)$$

Here \tilde{u}_l is the l -th component of velocity in Fourier space. $P_{ij}(\vec{k}) = \delta_{ij} - \frac{k_i k_j}{k^2}$ is the projection operator imposing incompressibility. Observe that the nonlinear term couples every Fourier mode *directly*⁷. One of the most useful shell models, the GOY shell model [19, 20], is inspired by Eq.(1.32).

$$\left[\frac{d}{dt} + \nu k_n^2 \right] u_n = i [a_n u_{n+1} u_{n+2} + b_n u_{n-1} u_{n+1} + c_n u_{n-1} u_{n-2}]^* + f_n. \quad (1.33)$$

Here the complex, scalar velocity u_n , for the shell n , depends on the one-dimensional, logarithmically spaced wave-vectors $k_n = k_0 2^n$, complex conjugation is denoted by $*$, and the coefficients $a_n = k_n$, $b_n = -\delta k_{n-1}$, and $c_n = -(1 - \delta) k_{n-2}$, with $\delta = 1/2$, are chosen to conserve the shell-model analogs of energy and helicity in the inviscid, unforced limit. By construction, the velocity in a given shell is affected directly only by velocities in nearest- and next-nearest-neighbour shells. By contrast, all Fourier modes of the velocity field interact with each other in Eq.(1.32).

The equal-time structure function of order- p and the associated exponent is

⁷This is also the source of *sweeping effect* in which large system size eddies advect the smaller eddies with size corresponding to inertial-range separation, these issues are discussed in detail later.

defined by

$$S_p(k_n) = \langle |u_n|^p \rangle \sim k_n^{-\zeta_p}. \quad (1.34)$$

However, the static solution of Eq.(1.33) exhibits a peculiar 3-cycle with the shell index n , which is effectively filtered out [21] if we use

$$\Sigma_p(k_n) \equiv \langle |\mathcal{J}(u_{n+2}u_{n+1}u_n - (1/4)u_{n-1}u_nu_{n+1})|^{p/3} \rangle \sim k_n^{-\zeta_p}, \quad (1.35)$$

to determine ζ_p . These exponents are in close agreement with those found for homogeneous, isotropic fluid turbulence in three dimension [21]. Further details are discussed in Chapter 2. Here we add that similar models has also been proposed to model passive-scalar turbulence, and magneto-hydrodynamic turbulence.

The simulation of these shell models are computationally much simpler compared to DNS of homogeneous and isotropic turbulence. And the scaling range for the structure functions obtained are close to ten octaves. These models clearly show multiscaling⁸, but they are so removed from the actual Navier–Stokes equation, that this evidence by itself can hardly be considered a convincing proof of multiscaling in fluid turbulence.

1.9 Passive-scalar turbulence

So far we have seen in both experiments and numerical simulations that K41 is possibly not the correct picture, but multiscaling is also not conclusively proved. Moreover a theoretical understanding of multiscaling based on the Navier–Stokes equation is practically non-existing. In this situation it would be helpful to have a simpler, but not too dissimilar, model that is amenable to both numerical and analytical studies, and which conclusively shows multiscaling. The Kraichnan model of passive-scalar turbulence turns out to be just the right model. Here we

⁸These models has been simulated for total number of shell ranging from 20 to 30. It is yet to be seen whether the multiscaling remains unchanged for a much higher number of total number of shells, e.g., 60 or so.

give a very sketchy review of how multiscaling appears in the Kraichnan model of passive-scalar. The methods sketched here will be used in Chapter 3, where we shall consider the dynamics of passive-scalar turbulence. For further details about the equal-time multiscaling in passive-scalar turbulence see Ref. [22].

A passive scalar (e.g., a dye or pollutant in flow) is one which is advected by the flow, but does not act back on the flow. The equation followed by the fluid is still the Navier–Stokes equation, whereas the passive-scalar field (θ), follows the equation,

$$\frac{\partial}{\partial t}\theta + [\vec{u}(\vec{x}, t) \cdot \vec{\nabla}] \theta = \kappa \nabla^2 \theta + f_\theta \quad (1.36)$$

Note the similarity of the advection term to the non-linear term of the Navier–Stokes equation. Observe that this equation is linear in the passive-scalar variable. In its full glory, passive–scalar turbulence is described by two coupled equations, the Navier–Stokes equation, and equation(1.36), and is certainly more complicated than the problem of Navier–Stokes turbulence. A simpler version was proposed by Kraichnan.

1.9.1 Kraichnan model

In the Kraichnan model the velocity $\vec{u}(\vec{x}, t)$ is not generated by the Navier–Stokes equation, but is a random, zero-mean, Gaussian variable and is white-in-time. The co-variance of velocity,

$$\langle u_i(\vec{x}, t) u_j(\vec{x} + \vec{\ell}, t') \rangle = 2D_{ij}(\vec{\ell}) \delta(t - t') \quad (1.37)$$

and the Fourier transform of D_{ij} has the form,

$$\tilde{D}_{ij}(\vec{q}) \propto \left(q^2 + \frac{1}{L^2} \right)^{-\frac{d+\xi}{2}} \exp(-\eta q^2) \left(\delta_{ij} - \frac{q_i q_j}{q^2} \right) \quad (1.38)$$

Here η plays to role of dissipation scale, and L plays to role of large scale of forcing, i.e., the integral scale. The factor inside brackets on the right assures incompressibility. d is the dimensionality of space. In the physical space this takes the

form,

$$D_{ij}(\vec{\ell}) = D_o \delta_{ij} - \frac{1}{2} d_{ij}(\vec{\ell}), \quad (1.39)$$

and in the limit of $L \rightarrow \infty$ and $\eta \rightarrow 0$ we get the scaling form

$$d_{ij} = D_1 \ell^\xi \left((d-1+\xi)\delta_{ij} - \xi \frac{\ell_i \ell_j}{\ell^2} \right). \quad (1.40)$$

D_1 is a normalisation constant. The parameter ξ plays a crucial role in this model. $0 < \xi < 2$ this model shows multiscaling for equal-time p -th order structure functions. But first define p -th order correlation function,

$$C_p(\vec{x}_1, \dots, \vec{x}_p) \equiv \langle \theta(\vec{x}_1, t) \theta(\vec{x}_2, t) \dots \theta(\vec{x}_p, t) \rangle \quad (1.41)$$

Here the angular brackets denote averaging over the statistics of the velocity and the force. The statistics of velocity and force are assumed to be independent of one another.

For simplicity let us first consider the 2-nd order correlation function,

$$C_2(\vec{\ell}, t) \equiv \langle \theta(\vec{x}, t) \theta(\vec{x} + \vec{\ell}, t) \rangle \quad (1.42)$$

Let us write its equation of motion

$$\partial_t C_2(\vec{\ell}, t) = \langle \partial_t \theta(\vec{x}, t) \theta(\vec{x} + \vec{\ell}, t) \rangle + \langle \theta(\vec{x}, t) \partial_t \theta(\vec{x} + \vec{\ell}, t) \rangle. \quad (1.43)$$

We replace the time derivatives by Eq.(1.36) and after performing Gaussian averaging over the velocity ensemble, we obtain,

$$\partial_t C_2(\ell) = D_1 \ell^{1-d} \partial_\ell [(d-1)\ell^{d-1+\xi} C_2(\ell)] + 2\kappa \ell^{1-d} \partial_\ell [\ell^{d-1} \partial_\ell C_2(\ell)] + \Phi \left(\frac{\ell}{L_I} \right), \quad (1.44)$$

where Φ is the spatial correlation of force. Now we look for stationary state correlation functions of the passive-scalar. In the stationary state the time derivative vanishes, and with the boundary condition that C_2 is zero for $\ell \rightarrow \infty$ and remains finite when $\ell \rightarrow 0$, we have,

$$C_2(\ell) = \frac{1}{(d-1)D_1} \int_\ell^\infty \frac{r^{1-d}}{r^\xi + \ell_d^\xi} dr \int_0^r \Phi \left(\frac{r}{L_I} \right) y^{d-1} dy. \quad (1.45)$$

In the limit $\ell_d \ll \ell \ll L_I$ the second-order structure function has the following scaling form,

$$S_2(\ell) = 2[C_2(0) - C_2(\ell)] \approx \frac{2}{(2 - \xi)(d - 1)D_1} \Phi(0) \ell^{2 - \xi} \quad (1.46)$$

Defining equal-time multiscaling exponents for the passive-scalar in exactly the same way for fluid turbulence, $\zeta_2^0 = 2 - \xi$. Observe that this result follows from dimensional reasoning too. For higher order correlation functions the equivalent of Eq.(1.44) can be symbolically written as,

$$\partial_t C_p = -\mathcal{M}_p C_p + \mathcal{D}_p C_p + \mathcal{F} \otimes C_{p-2}, \quad (1.47)$$

where \mathcal{M}_p is the operator determined by the advection term, \mathcal{D}_p is the dissipative operator, and \mathcal{F} is the spatial correlator of forcing. In the limit of vanishing diffusivity, and in stationary state, Eq.(1.47) reduces to

$$\mathcal{M}_p C_p = \mathcal{F} \otimes C_{p-2} \quad (1.48)$$

The solution of this linear equation is the sum of solution of two equations:

1. Solution of the associated homogeneous equation,

$$\mathcal{M}_p \mathcal{Z}_p = 0 \quad (1.49)$$

2. The solution of the inhomogeneous one, which we denote by $C_p^{\mathcal{I}}$.

Assuming scaling behaviour,

$$C_p^{\mathcal{I}}(\lambda \vec{r}_1, \lambda \vec{r}_2, \dots, \lambda \vec{r}_p) \sim \lambda^{\zeta_p^{\text{dim}}} C_p^{\mathcal{I}}(\vec{r}_1, \vec{r}_2, \dots, \vec{r}_p) \quad (1.50)$$

we can extract the scaling exponent from simple dimensional analysis of Eq.(1.47). to obtain,

$$\zeta_p^{\text{dim}} = \frac{p}{2} (2 - \xi) \quad (1.51)$$

The solution of Eq.(1.49) are called the *zero-modes* of the the operator \mathcal{M}_p . The zero-modes, which would satisfy the boundary conditions and which also have scaling properties, namely,

$$\mathcal{Z}_p(\lambda\vec{r}_1, \lambda\vec{r}_2, \dots, \lambda\vec{r}_p) \sim \lambda^{\zeta_p^{\text{zero}}} \mathcal{Z}_p(\vec{r}_1, \vec{r}_2, \dots, \vec{r}_p), \quad (1.52)$$

have scaling exponents (ζ_p^{zero}) which cannot be determined from dimensional arguments. The exponents ζ_p^{zero} are also called anomalous exponents. And for a particular order- p the actual scaling exponent,

$$\zeta_p = \min(\zeta_p^{\text{dim}}, \zeta_p^{\text{zero}}). \quad (1.53)$$

This is how multiscaling arises in Kraichnan model of passive scalar. The principal difficulty lies in solving Eq.(1.49) with a particular boundary condition. In recent time following result has been obtained [22]: Although the scaling exponents for the zero-modes has not been obtained exactly for any p except for $p = 2$ in which case the anomalous exponent is actually subdominant, perturbative methods have shown the anomalous exponents to have the form,

$$\zeta_p^\theta = \frac{2}{p}(2 - \xi) - \delta_p; \quad (1.54)$$

$$\delta_p \approx \frac{p(p-2)}{2(d+2)}\xi + O(\xi^2) \quad (1.55)$$

$$\delta_p \approx \frac{1}{2d}p(p-2) + O(1/d^2) \quad (1.56)$$

It is clear from the above expression that the multiscaling disappears for $\xi \geq 2$ or $\xi \leq 0$. It has also been shown that although the scaling exponents as given above are universal, the amplitudes depend on the force correlator and hence the structure functions themselves are *not* universal. These results has also been well supported by numerical simulations.

We shall present results about dynamic scaling properties of passive-scalar turbulence in Chapter 3, where we shall show that in the Kraichnan model due to the white-in-time nature of the velocity, *simple dynamic scaling* is obtained.

The Kraichnan model has had a great influence on the way physicist think about multiscaling in turbulence. As the evidence for multiscaling in fluid turbulence is not extremely strong, clear evidence of equal-time multiscaling in the Kraichnan model has been very useful. In research on multiscaling in turbulence, Kraichnan model may eventually have the same status as Onsager's solution of the two dimensional Ising model has in the research of critical phenomenon.

1.10 Dynamics of turbulence

So far we have concentrated on equal-time structure functions in turbulence. A part of the work presented in thesis, namely Chapters 2,3 and 4, is about dynamic phenomenon in turbulence. In this Section we give a short introduction which will be useful in understanding the material presented later in this thesis.

In a qualitative sense the dynamics of turbulence involves the lifetime of eddies in the flow. We expect that eddies of large characteristic length scales decay slowly, i.e., has larger characteristic time scale. This phenomenon is called the *permanence of large eddies*. The equal-time properties of turbulence are studied by equal-time structure functions. In a similar way dynamical properties should be studied by appropriate dynamical structure functions. which we shall define precisely below. But first we make a digression to discuss briefly the dynamics of critical phenomenon. Within this digression we use a set of symbols which are common to the critical phenomenon literature. The reader is cautioned against confusing them with the nomenclature of turbulence. For example, in the following Section ν is a critical exponent not the viscosity as is used in rest of this thesis.

1.10.1 Critical dynamics

Consider a system of spins in d dimensions of space at thermal equilibrium with a heat bath at temperature T . The equal-time statistical properties of this system are described by the spin-spin correlation function defined by:

$$\Gamma(\ell, t, h) = \langle S(\vec{x})S(\vec{x} + \vec{\ell}) \rangle - \langle S(\vec{x}) \rangle \langle S(\vec{x} + \vec{\ell}) \rangle \quad (1.57)$$

Where $h = H/(k_B T_c)$ and H is the external magnetic field. $t = \frac{T-T_c}{T_c}$ the reduced temperature. T_c is the critical temperature and k_B the Boltzmann constant. For T close to T_c the following scaling law is observed,

$$\Gamma(\ell, t, h) \approx \frac{1}{\ell^{d-2+\eta}} \mathcal{F}(t^\nu \ell, h/t^\Delta); \quad (1.58)$$

Here η , ν and Δ are the static critical exponents. \mathcal{F} is the universal scaling function. ξ is called the correlation length, which diverges near the critical point. In Fourier space this scaling law looks like,

$$\tilde{\Gamma}(q, t, h) \approx \frac{1}{q^{2-\eta}} \mathcal{F}(t^\nu q, h/t^\Delta). \quad (1.59)$$

It is well known that if this spin system close to the critical point are disturbed from its equilibrium configuration, the return to the equilibrium is a very slow process, a phenomenon called *critical slowing down*. The dynamics is captured by the frequency(ω) dependent version of $\tilde{\Gamma}(q, t, h)$,

$$\tilde{\Gamma}(q, \omega, t, h) \approx \frac{1}{q^{2-\eta}} \mathcal{G}(q^{-z} \omega, t^\nu q, h/t^\Delta) \quad (1.60)$$

Here z is called the dynamical critical exponent. The phenomenon of critical slowing down is reflected by the fact that the relaxation time diverges as,

$$\tau \sim \xi^z. \quad (1.61)$$

In the language of critical phenomenon, this is power-law behaviour of the characteristic time-scale is called dynamic scaling, and z is called the dynamic scaling exponent.

Now we close our digression, and define dynamic structure functions in turbulence much in the same spirit as the dynamic correlation functions in critical phenomenon.

1.10.2 Time-dependent structure functions

First let us define dynamic longitudinal structure function of order-2, namely,

$$\mathcal{F}_2(\ell, t) = \langle \delta u_{\parallel}(\vec{x}, \ell, 0) \delta u_{\parallel}(\vec{x}, \ell, t) \rangle; \quad (1.62)$$

$$\delta u_{\parallel}(\vec{x}, \ell, t) = [\vec{u}(\vec{x} + \vec{\ell}, t) - \vec{u}(\vec{x}, t)] \cdot \left(\frac{\vec{\ell}}{\ell}\right). \quad (1.63)$$

As usual the angular brackets denote averaging over the statistically stationary state. From this let us extract two different time-scales, and make a scaling ansatz for each one of them:

1. The integral time-scale, of order-2

$$\mathcal{T}_2^I(\ell) = \frac{1}{\mathcal{S}_2(\ell)} \int_0^{\infty} \mathcal{F}_2(\ell, t) dt \sim \ell^{z_2^I} \quad (1.64)$$

2. The curvature time-scale, or in other words derivative time-scale of degree-2, and order-2,

$$\mathcal{T}_{2,2}^D(\ell) = \left[\frac{1}{\mathcal{S}_2(\ell)} \frac{\partial^2 \mathcal{F}_2(\ell, t)}{\partial t^2} \Big|_{t=0} \right]^{(-1/2)} \sim \ell^{z_{2,2}^D} \quad (1.65)$$

In dynamic critical phenomena different ways of extracting time scales from correlation functions lead to the same exponents, therefore we expect

$$z_2^I = z_{2,2}^D. \quad (1.66)$$

although the two time scales extracted would not be equal. We shall show (in later Chapters) that this result will not hold in turbulence. This would also imply that although in critical phenomenon the whole dynamic correlation function will show data collapse if the time axis is scaled in the proper way, no such data

collapse is possible in the case of turbulence. From here we can generalise to dynamic structure functions of order- p

$$\mathcal{F}_p(\ell, t_1, t_2, \dots, t_{p-1}) = \langle \delta u_{\parallel}(\vec{x}, \ell, 0) \delta u_{\parallel}(\vec{x}, \ell, t_1) \dots \delta u_{\parallel}(\vec{x}, \ell, t_{p-1}) \rangle \quad (1.67)$$

Due to stationarity this generalised p -th order structure function contains $p - 1$ time labels. First set m , of these $p - 1$ time labels to 0 and the rest to t . Then we can define varieties of characteristic time scales in exactly the same way we have done for order-2. We also generalise the degree of the structure function ($M > 0$) [23]:

1. Integral time-scale:

$$\mathcal{T}_{p,M}^I(\ell) = \left[\frac{1}{\mathcal{S}_p(\ell)} \int_0^{\infty} \mathcal{F}_p(\ell, t) t^{M-1} dt \right]^{1/(M-1)} \sim \ell^{z_{p,M}^I} \quad (1.68)$$

2. Derivative time-scale:

$$\mathcal{T}_{p,M}^D(\ell) = \left[\frac{1}{\mathcal{S}_p(\ell)} \frac{\partial^M \mathcal{F}_2(\ell, t)}{\partial t^M} \right]^{(-1/M)} \sim \ell^{z_{p,M}^D} \quad (1.69)$$

We shall show later that the scaling behaviour of these time scales does not depend on m . Unlike the critical phenomenon in which $z_{p,M}^I = z_{p,M}^D$ for all p and M , in turbulence all these dynamic scaling exponents are different. We call these phenomenon *dynamic multiscaling*. Time-scales can also be extracted from the most general dynamic structure function we have defined in Eq.(1.67).

We show later that these time scales can be related to the equal-time multiscaling exponents ζ_p by relationships which we call *bridge-relations*(see Chapter 2 and 4). Similar bridge-relations for passive-scalar models are elucidated in Chapter 3. But there are more subtleties in study of dynamic scaling and multiscaling in turbulence.

1.10.3 Eulerian versus Lagrangian

Let us remind our reader that the Navier–Stokes equation is written in terms of fluid velocity at the point \vec{x} and at time t , which is the *Eulerian velocity*. Typical experiments measure this Eulerian velocity and the structure functions are calculated via Taylor’s frozen-flow hypothesis. Taylor’s hypothesis implies that characteristic length and time scales are linearly related, which implies a dynamic exponent equal to unity, for all order and degree. To gain a better understanding, let us try to see what a K41 type argument would imply for dynamic multiscaling.

The characteristic time scale $\mathcal{T}(\ell)$ of an eddy of length-scale ℓ should have the following dimensional form:

$$\mathcal{T}(\ell) \sim \frac{\ell}{\delta u(\ell)} \sim \ell^{2/3} \quad (1.70)$$

as according to K41, the characteristic velocity difference $\delta u(\ell)$ of an eddy of size ℓ scales as $\ell^{1/3}$. This implies $z_p^{\text{K41}} = 2/3$ for all p , which is in contradiction to the prediction from Taylor’s hypothesis prediction of $z_p^{\text{Taylor}} = 1$. Observe that the Taylor’s hypothesis is also valid even when there is no mean flow. Because the large system size eddies are long-lived and they advect the smaller scale eddies. This is called the *sweeping effect*. Hence for time scales not too large, the characteristic velocities of the system size eddies act as the mean flow giving rise to a dynamic scaling exponent of unity.

This paradox is resolved by observing that as long as we use Eulerian velocities *sweeping effect* is always present. But if instead we use Lagrangian velocities the K41 prediction is expected to hold. And if we go beyond K41 (e.g. in the multifractal model) the Lagrangian velocities would show dynamic multiscaling.

The other way to see dynamic multiscaling is to somehow remove the dominant *sweeping effect*. One such way is to use *Quasi-Lagrangian* velocities. Another is to use explicitly Galilean invariant structure functions. This two methods shall

be elucidated in Chapter 4.

1.10.4 Lagrangian measurements

Early measurements of dynamic structure functions of order-2 were done for Eulerian velocities by Come-Bellot and Corrsin (Ref. [24]) from wind-tunnel experiments. The emphasis was on experimental verification of Taylor's hypothesis. Soon dynamic structure function for Lagrangian velocities were done by Shlien and Corrsin(Ref. [25]), and compared with previous Eulerian measurements. The characteristic decay time for Lagrangian velocities were found to be smaller than corresponding Eulerian quantities, but there was no attempt to extract dynamic scaling exponents. More recently, dynamic scaling exponent of order-2 and degree-2, of the derivative type, namely $T_{2,2}^D$, were measured by Kaneda and his group [26] from their DNS calculations with 512^3 grid points. Fig.(1.8) is reproduced from their work, which gives good evidence in favour of the statement that for Eulerian velocities $z_{2,2}^D = 1$ and $z_{2,2}^D = 2/3$ for Lagrangian velocities. But the authors made no attempt to systematically extract dynamic multiscaling exponents.

In recent times experimental measurement of Lagrangian velocities have improved, see for example Ref. [27, 28, 29]. In these experiments a flow (which is unfortunately quite anisotropic) is seeded by millions of passive tracers. If the tracers are small enough and their density is close enough to the density of the fluid, then these tracers approximated well the behaviour of Lagrangian particles. Consider one such Lagrangian particle at the space-point \vec{x}_0 at time t_0 . Let its Lagrangian displacement be $\vec{\rho}(t | \vec{x}_0, t_0)$. The Lagrangian velocity of this particle at time t is defined by

$$\vec{U}(t | \vec{x}_0, t_0) = \frac{\partial}{\partial t} \vec{\rho}(t | \vec{x}_0, t_0), \quad (1.71)$$

i.e the tangent to its Lagrangian path at time t . In experiments the Lagrangian

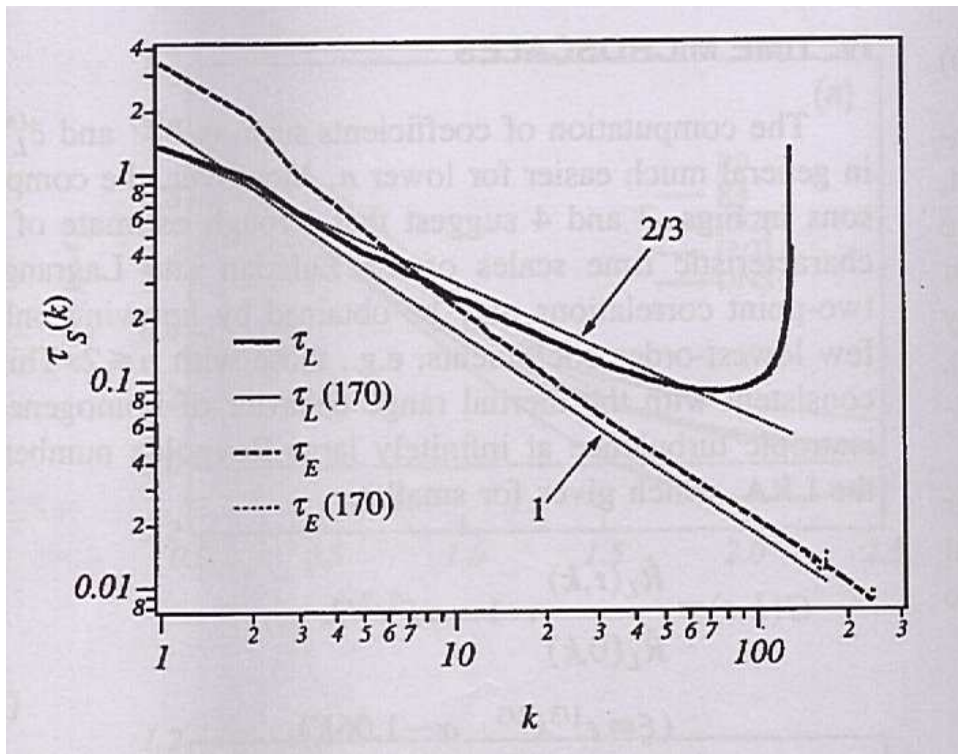


Figure 1.8: A plot showing the extraction of dynamic scaling exponents from the DNS study in Ref. [26] for Eulerian and Lagrangian velocities. The figure plots the characteristic time-scales versus the Fourier k mode, on a log – log scale. A linear least-square fit to this plot in the inertial range gives a slope equal to $-z_{2,2}^D$. The difference in the scaling exponent is clearly visible.

path of the tracer particles are recorded and from them Lagrangian velocity is obtained. It is observed that the Lagrangian acceleration is a very intermittent function of time [28]. Although none of these experiments have attempted to extract the dynamic structure function of Lagrangian velocities as we have defined in Section 1.10

In recent numerical simulation of Lagrangian velocities, [30] Lagrangian structure functions have been measured. These structure functions, defined below,

$$\mathcal{S}_p^{\text{time}}(\tau) \equiv \langle [U_i(t + \tau | \vec{x}_0, t_0) - U_i(t | \vec{x}_0, t_0)]^p \rangle \sim \tau^{\zeta_p^{\text{time}}}. \quad (1.72)$$

also show multiscaling. But these structure functions, which have no Eulerian or quasi-Lagrangian analogue, should not be confused with the dynamic struc-

ture functions we have defined earlier. The multiscaling exponents in the case do not relate characteristic time scales with characteristic length scales, and seems to have no direct connection to the dynamic multiscaling exponents we have defined.

1.11 Burgulence

Till now we have discussed equal-time and dynamic multiscaling in fluid turbulence. The last Chapter of this thesis (Chapter 5) is description of our work in turbulence in stochastically forced Burgers equation. In the rest of this chapter we give a very short introduction this problem. We shall confine ourselves to only those parts of Burgers turbulence which are of direct relevance to us.

Turbulence in Burgers equation is the study of random solution of Burgers equation:

$$\partial_t u + u \partial_x u = \nu \partial_{xx} u. \quad (1.73)$$

The velocity u in d -dimension is prescribed to be irrotational, i.e. $u = -\partial_x \psi$, where ψ is often called the velocity potential. The randomness arises either from random initial conditions $u_0 = -\partial_x \psi_0$ are given or because a random driving force $f = -\partial F$ is added to the RHS of (1.73), or both. When $f = 0$ one speaks about *decaying burgulence*.

1.11.1 Introduction

In this thesis we shall confine our discussions mostly to Burgers equation in one spatial dimension. Our introduction follows very closely the review article by U. Frisch and J. Bec [31].

Burgers equation shares the following properties with the Navier–Stokes equation:

- same type of advective nonlinearity

- presence of a diffusion term from which a Reynolds number may be defined
- many invariance and conservation laws in common: invariance under translations in space and time, parity invariance, conservation of momentum and energy (only for $\nu = 0$ and $d = 1$).

But it was discovered that that the Burgers equation can actually be integrated explicitly [32, 33]. Indeed, an important property of the Navier–Stokes equation, not shared by the Burgers equation, is the sensitivity to small changes in the initial conditions in the presence of boundaries or driving forces and at sufficiently high Reynolds numbers. Hence, the Burgers equation is not a good model for one of the most important aspects of turbulence: the spontaneous generation of randomness by chaotic dynamics.

In spite of this the Burgers equation has found application in diverse field of physics ranging from compressible flow, nonlinear acoustics, condensed matter physics to cosmology.

In particular, in condensed matter physics, a frequently studied problem is the Kardar–Parisi–Zhang or KPZ equation [34] (see also Ref. [35]), which is the equation satisfied by the velocity potential ψ of the Burgers equation.

$$\partial_t \psi = \frac{1}{2} |\nabla \psi|^2 + \nu \nabla^2 \psi + F, \quad (1.74)$$

This equation appears in studying the motion of an interface growing, say, because of deposition of particles. Here, ψ is the vertical displacement of the interface as a function of $d-1$ horizontal coordinates and of the time. It is immediately checked, by taking the horizontal gradient of (1.74), that one obtains the Burgers equation (1.73) with an additional forcing term $\mathbf{f} = -\nabla F$. Burgers equation also arises in studying directed polymers (see, e.g., Refs. [36, 35]), but with the time variable now interpreted as a space variable in the direction of main extension of the polymers.

But the reason for which we concentrate on the Burgers equation is that, because of its known solutions, it is frequently used as a testing ground for Navier–Stokes equation. Indeed, there have been many attempts to tackle the problem of the statistical theory of turbulence by adapting to it tools borrowed from field theory (for reviews, see Refs. [1, 37, 38, 39]). In the past such field-theoretic methods have frequently involved formal expansions in powers of the nonlinearity, with Feynman graphs used for the bookkeeping of all the terms generated after averaging over Gaussian initial conditions and/or random forces. Since the Burgers equation has the same type of nonlinearity as the Navier–Stokes equation such methods are typically also applicable to the Burgers equation. Hence it is possible to find what they predict for the latter and to compare the results with those obtained by more reliable methods. From this point of view, that is of using the Burgers equation as testing ground, it is desirable to know the answers to questions similar to those generally asked about Navier–Stokes turbulence. For example, what are the scaling properties of structure functions? This is the issue we will concentrate on in this thesis. The emphasis will be exclusively on what happens in the real space-time domain in the limit of vanishing viscosity, which is of course not the same as naively putting the viscosity equal to zero.

1.11.2 Basic tools

If in 1.74 with $F = 0$ we set $\psi = 2\nu \ln \theta$ we obtain the 1-dimensional heat equation [32, 33]

$$\partial_t \theta = \nu \nabla^2 \theta, \quad (1.75)$$

which can be solved explicitly if there are no boundaries. One thus obtains

$$\psi(r, t) = 2\nu \ln \left\{ \frac{1}{(4\pi\nu t)^{1/2}} \int \exp \left[\frac{1}{2\nu} \left(\psi_0(\mathbf{a}) - \frac{(r - \mathbf{a})^2}{2t} \right) \right] d^d \mathbf{a} \right\}, \quad (1.76)$$

where $\psi_0(a)$ is the initial potential. The limit of vanishing viscosity ($\nu \rightarrow 0$), obtained by steepest descent, has the following “maximum representation”

$$\psi(r, t) = \max_a \left(\psi_0(a) - \frac{(r - a)^2}{2t} \right). \quad (1.77)$$

If $\psi_0(a)$ is differentiable (i.e. the initial velocity $u_0(a)$ exists as an ordinary function rather than a distribution), the maximum in 1.77 will be achieved at one or several points a where the gradient of the RHS vanishes, that is, where

$$r = a + tu_0(a) \quad (1.78)$$

In other words, r is the position at time t of the fluid particle starting at a and retaining its initial velocity $u_0(a)$. Hence, we can interpret a and r as being, respectively, Lagrangian and Eulerian coordinates. Along this Lagrangian trajectory, the velocity being conserved, we have

$$u(r, t) = u_0(a). \quad (1.79)$$

The map $a \mapsto r$ defined by 1.78 is called the naive Lagrangian map. It is not necessarily invertible: if there are several Lagrangian locations satisfying 1.78 for a given r the only acceptable one is that which maximises the argument on the RHS of 1.77. In one dimension, the time t_* , after which the naive Lagrangian map become non-invertible, is the inverse of the absolute value of the most negative initial velocity derivative $du_0(a)/da$. It is the first time at which the characteristics $x = a + tu_0(a)$ of the hyperbolic inviscid Burgers equation are crossing (Fig. 1.9).

Let us now summarise what we have found about evolution of Burgers equation in the limit of zero viscosity. We start with an initial velocity u_0 and initial potential ψ_0 . Then we want the velocity at any future time t . At time t the fluid particle at location x has come from point a such that a satisfies Eq.1.77. The the velocity at x at t is the the velocity at the point a at the initial time. This allows

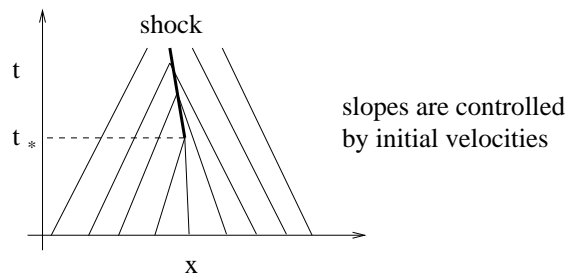


Figure 1.9: Characteristics for the unforced one-dimensional Burgers equation in the (x, t) plane. Figure taken from Ref [31]

us to construct the solution of at any future time t from the initial velocity potential. The crucial step is the process of taking the maximum in Eq.1.77, which is a global process.

We present a geometrical construction to visualise this process of taking maximum, called the “parabola construction”, illustrated in Fig. 1.10: a parabola with apex at x and radius of curvature proportional to t is moved down until it touches the initial potential $\psi_0(a)$ at the Lagrangian location associated to x (or at two such locations if there is a shock).

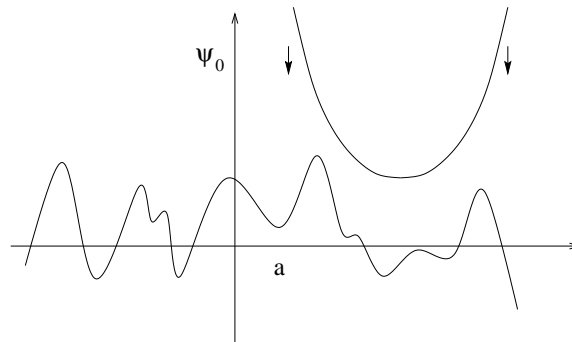


Figure 1.10: Parabola construction of the solution. Picture taken from [31]

There at least four other geometrical methods [31] to help visualise the solution of Burgers equation which we are not going to discuss. Which of the five geometrical methods is more convenient depends on the application considered. None that none of these methods helps us to construct the solution of Burgers equation when we have a non-zero force on the RHS of Eq. 1.73. Our numerical algorithm for the forced case relies heavily on this form of exact solution of

Burgers equation as described here.

And finally note that our description of the evolution under Burgers equation implies that when two fluid particles collide they stick to each other to form shocks. And between the collisions the fluid particles move with constant velocity. As the collision between the fluid particles are inelastic there is of course a finite dissipation. This constitutes a proof of the analogue of zeroth law of fluid turbulence (Section 1.6.2). As this argument relies to the form of the exact solution to the Burgers equation in the vanishing viscosity limit, it cannot be applied to the Navier–Stokes equation.

1.11.3 Structure functions

We now turn to the scaling properties of the structure functions of velocity difference in Burgers equation. With random and homogeneous and smooth initial conditions there will be shocks (discontinuities) at random Eulerian locations which do not cluster. From this it is easily inferred that, for $p > 0$, the structure functions

$$S_p(\Delta x, t) \equiv \langle |u(x + \Delta x, t) - u(x, t)|^p \rangle \quad (1.80)$$

behave, for small Δx , as

$$S_p(\Delta x, t) \sim C_p |\Delta x|^p + C'_p |\Delta x|, \quad (1.81)$$

where the first term comes from regular (smooth) parts of the Eulerian velocity, while the second comes from the $O(|\Delta x|)$ probability to have a shock somewhere in an interval of Eulerian length $|\Delta x|$. For $0 < p < 1$ the first term dominates as $\Delta x \rightarrow 0$, while, for $p > 1$, it is the second. Hence, $S_p \sim |\Delta x|^{\zeta_p}$, with the exponents ζ_p as shown in Fig. 1.11. This behaviour of multiscaling exponents is called *bi-scaling* and the underlying fractal nature *bi-fractal*.

There are also higher-order corrections to the simple scaling law given in 1.81 which cannot be obtained by such simple arguments [40]. Note that a second-

order structure functions with a behaviour $\propto |\Delta x|$ at small distances implies an energy spectrum $E(k) \propto k^{-2}$ as $k \rightarrow \infty$. Note that same form of bifractality is ob-

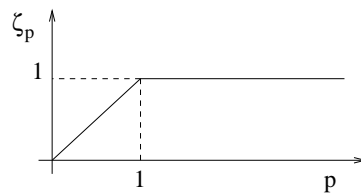


Figure 1.11: Exponent of the structure function of order p .

tained in Burgers equation forced at large spatial length scales. We have defined the structure function here with the absolute value of velocity difference. In the case of Burgers equation forced in large spatial length scales, the structure functions defined by not taking the absolute value show same scaling behaviour [40].

1.12 Summary

At the end our brief introduction to turbulence, let us a list few important point we shall use often in the rest of this thesis.

1. Experiments and DNS strongly suggests the presence of multiscaling in fluid turbulence. The evidence in support of multiscaling in strong but not conclusive.
2. We have mostly confined ourselves to scaling of order- p longitudinal structure functions in homogeneous isotropic turbulence defined by Eq.(1.6). In measurement of structure functions from real flows the following points should be noted:
 - (a) In experiments, instead of the velocity of the turbulent fluid at different points, a time-series of the velocity at a particular point is measured and the Taylor frozen-flow hypothesis is used to calculate the equal-time spatial structure functions. (see Section 1.5 and Section 1.10.3).

- (b) Structure functions constructed with longitudinal velocity difference and transverse velocity difference seems to have different but not widely different multiscaling exponents [7].
 - (c) Structure functions constructed with absolute value of of velocity difference seems to have slightly different multiscaling exponents that structure functions defined without the absolute value.
3. As far as dynamic scaling is concerned, dynamic structure functions [see Section(1.10)] are expected to show simple scaling with dynamic scaling exponents of $z = 1$ if Eulerian velocities are used, on the other hand Lagrangian or quasi-Lagrangian velocity structure functions are expected to show dynamic multiscaling. For the later, K41 theory predicts simple scaling with $z = 2/3$. There is some (but certainly not enough) evidence from experimental and numerical studies in support of this statement.

In the first part of this thesis consisting of Chapter 2, 3 and 4 we investigate dynamic multiscaling in fluid, passive-scalar and passive-vector turbulence. Our conclusions are summarised below :

1. By using the multifractal model we find bridge relations which connect the dynamic multiscaling exponents to the equal-time scaling exponents ζ_p [see Section(1.10), and Chapter 2].
2. The bridge relations depend on *how* the time scales are extracted from the time-dependent structure functions.
3. We give evidence in support of the two results given above by extensive numerical simulations of the GOY shell model.
4. The Kraichnan model of passive scalar show simple dynamic scaling (Chapter 3).

5. A passive scalar shell model advected by velocity field from GOY shell model show dynamic multiscaling (Chapter 3).
6. We present the first measurements of equal-time quasi-Lagrangian velocity structure functions, from 512^3 pseudo-spectral DNS studies of homogeneous isotropic turbulence and preliminary data for their dynamic properties (Chapter 4).

We have also summarised [Sec 1.11] the results of Burgulence which will be useful to us in Chapter 5 of this thesis. There we shall present compelling evidence in support of the fact that Burgers equation with forced with a stochastic force having a spectrum which goes as $1/k$ in Fourier space (where k is the Fourier mode) show multiscaling. This makes Burgers equation the simplest *non-linear*, one dimensional PDE showing multiscaling. We hope that understanding of multiscaling in this relatively simpler context may provide crucial clues for understanding multiscaling in fluid turbulence.

Bibliography

- [1] U. Frisch, *Turbulence the legacy of A.N. Kolmogorov* (Cambridge University Press, Cambridge, 1996).
- [2] T. Bohr, M. Jensen, G. Paladin, and A. Vulpiani, *Dynamical systems approach to turbulence* (Cambridge University Press, Cambridge, 1998).
- [3] G. Batchelor, *The theory of homogeneous turbulence* (Cambridge University Press, Cambridge, 1953).
- [4] A. Monin and A. Yaglom, *Statistical fluid mechanics* (MIT Press, Cambridge, Massachusetts, 1972).
- [5] M. V. Dyke, *An album of fluid motion* (The Parabolic Press, Stanford, California, 1982).
- [6] A. Kolmogorov, Dokl. Acad. Nauk USSR **30**, 9 (1941).
- [7] B. Dhruva, Y. Tsuji, and K. Sreenivasan, Physical Review E **56**, R4928 (1997).
- [8] T. Ishihara, Y. Kaneda, M. Yokokawa, K. Itakura, and A. Uno, Journal of Physical Society of Japan **72**, 983 (2003).
- [9] F. Anselmet, Y. Gagne, E. Hopfinger, and R. Antonia, J. Fluid Mech. **140**, 63 (1984).
- [10] K. Sreenivasan, Physics of Fluids **10**, 528 (1998).

- [11] Y. Kaneda, T. Ishihara, M. Yokokawa, K. Itakura, and A. Uno, *Physics of Fluids* **15**, L21 (2003).
- [12] J. von Neumann, in *Collected works (1949-1963)*, edited by A. Taub (Pergamon Press, ADDRESS, 1963), Vol. 6, p. 437.
- [13] S. Orszag and G. Patterson, *Phys. Rev. Lett.* **28**, 76 (1972).
- [14] S. Pope, *Turbulence* (Cambridge University Press, Cambridge, 2000).
- [15] R. Benzi, S. Ciliberto, R. Trippiccone, C. Baudet, F. Massaioli, and S. Succi, *Phys. Rev E* **48**, R29 (1993).
- [16] R. Benzi, L. Biferale, S. Ciliberto, M. Struglia, and R. Tripiccone, *Europhys. Lett.* **32**, 709 (1995).
- [17] S. Douady, Y. Couder, and M. Brachet, *Phys. Rev. Lett.* **67**, 983 (1991).
- [18] Z.-S. She and E. Leveque, *Phys. Rev. Lett.* **72**, 336 (1994).
- [19] E. Gledzer, *Sov. Phys. Dokl.* **18**, 216 (1973).
- [20] K. Ohkitani and M. Yamada, *Prog. Theor. Phys.* **55**, 833 (1985).
- [21] L. Kadanoff, D. Lohse, J. Wang, and R. Benzi, *Phys. Fluids* **7**, 617 (1999).
- [22] G. Falkovich, K. Gawędzki, and M. Vergassola, *Rev. Mod. Phys.* **73**, 913 (2001).
- [23] D. Mitra and R. Pandit, *Phys. Rev. Lett* **93**, 024501 (2004).
- [24] G. Come-Bellot and S. Corrsin, *J. Fluid. Mech.* **48**, 273 (1971).
- [25] D. Shlien and S. Corrsin, *J. Fluid. Mech.* **62**, 255 (1974).
- [26] Y. Kaneda, T. Ishihara, and K. Gotoh, *Phys. Fluids.* **11**, 2154 (1999).

- [27] S. Ott and J. Mann, *J. Fluid Mech.* **422**, 207 (2000).
- [28] A. L. Porta, G. Voth, A. Crawford, J. Alexander, and E. Bodenschatz, *Nature(London)* **409**, 1111 (2002).
- [29] N. Mordant, P. Metz, O. Michel, and J.-F. Pinton, *Phys. Rev. Lett.* **87**, 214501 (2001).
- [30] L. Biferale, G. Boffetta, A. Celani, B. Devenish, A. Lanotte, and F. Toschi, *nlin.CD/0403020* (2004).
- [31] U. Frisch and J. Bec, in *New Trends in Turbulence*, edited by A. Yaglom, F. David, and M. Lesieur (Springer EDP-Sciences, Les Ulis and Berlin, 2000), Vol. Les Houches Session LXXIV, pp. 341–383.
- [32] E. Hopf, *Comm. Pure Appl. Math.* **3**, 201 (1950).
- [33] J. Cole, *Quart. Appl. Math.* **9**, 225 (1951).
- [34] M. Kardar, G. Parisi, and Y.-C. Zhang, *Phys. Rev. Lett.* **56**, 889 (1986).
- [35] J. Bouchaud, M. Mézard, and G. Parisi, *Phys. Rev. E* **52**, 3656 (1995).
- [36] M. Kardar and Y.-C. Zhang, *Phys. Rev. Lett.* **58**, 2087 (1987).
- [37] S. Orszag, in *Fluid Dynamics, Les Houches*, edited by R. Balian and J. Peube (Gordon and Breach, New York, 1977), pp. 237–374.
- [38] H. Rose and P. Sulem, *J. Phys. France* **39**, 441 (1978).
- [39] M. Lesieur, *Turbulence in Fluids*, Vol. 40 of *Fluid Mechanics and Its Applications* (Kluwer, ADDRESS, 1997).
- [40] J. Bec, U. Frisch, and K. Khanin, *J. Fluid Mech.* **416**, 239 (2000).

Chapter 2

The varieties of dynamic multiscaling

In this Chapter we elucidate the dynamic multiscaling of time-dependent velocity structure functions in models for fluid turbulence. As we have discussed in Chapter 1, studies of time-dependent velocity structure functions by lag far being studies of their equal-time counterparts. Our main aim in this Chapter is to make up for this especially with a view to developing the analogue of the dynamic scaling of time-dependent correlation functions in the vicinity of a critical point [1].

In particular we show that different ways of extracting time scales from time-dependent velocity structure functions lead to different dynamic-multiscaling exponents ¹ These exponents are related to equal-time multiscaling exponents by different classes of bridge relations which we derive using the multifractal model, discussed in Chapter 1. We check this bridge-relations explicitly by detailed numerical simulations of the GOY shell model for fluid turbulence [2, 3].

2.1 Introduction

To understand dynamic multiscaling in turbulence, it is useful first to recall the dynamic scaling of the time-dependent correlation function in critical phenomenon.

¹For precise definitions of dynamic-multiscaling exponents see page 55.

Consider, e.g., an Ising ferromagnet in d -dimension. Near its critical point, the equal-time spin-spin correlation function at temperature T assumes the following scaling form

$$\Gamma(r, T_r, h) \approx \frac{1}{r^{d-2+\eta}} \mathcal{F}(T_r^\nu \xi, h/T_r^\Delta); \quad (2.1)$$

where r is the separation between the spins, T_r is the reduced temperature, $\equiv (T - T_c)/T_c$, $h \equiv H/k_B T_c$. T_c is the critical temperature, ξ the correlation length, which diverges at the critical point, and η , ν and Δ are static critical exponents. \mathcal{F} is the universal scaling function². The Fourier-space analogue of Eq. (2.1) is

$$\tilde{\Gamma}(\vec{q}, T_r, h) \approx \frac{1}{q^{2-\eta}} \mathcal{F}(T_r^\nu \xi, h/T_r^\Delta), \quad (2.2)$$

where \vec{q} is the wave vector with magnitude q . Furthermore, near the critical point the spin system shows *critical slowing down*, i.e., τ , the characteristic time scale for fluctuation, diverges as a power of the correlation length ξ , more specifically

$$\tau \sim \xi^z, \quad (2.3)$$

where z is called the dynamic scaling exponent. This phenomenon is reflected in the the time-dependent correlation function, which has the following form:

$$\tilde{\Gamma}(\vec{q}, t, T_r, h) \approx \frac{1}{q^{2-\eta}} \mathcal{G}(q^{-z}t, T_r^\nu \xi, h/T_r^\Delta); \quad (2.4)$$

where t denotes the time and \mathcal{G} is a scaling function. Existence of dynamic scaling implies that the the function $q^{2-\eta} \tilde{\Gamma}(\vec{q}, t, T_r, h)$ (for fixed T_r and h) for different q -values, plotted against tq^{-z} collapses on one another. And the collapsed function is the function \mathcal{G} . A third way of looking at dynamic scaling is to extract a q dependent time scale $\tau(q)$ from $\tilde{\Gamma}(\vec{q}, t, T_r, h)$. Irrespective of how this time scale is extracted, we always obtain the scaling relation $\tau(q) \sim q^{-z}$ with an unique z . This understanding of dynamic scaling in critical phenomenon emeged soon after the scaling of equal-time correlations [1].

²It is universal only if two scale factors are factored out [4]

By contrast, the development of an understanding of the dynamic multiscaling of time-dependent velocity structure functions in homogeneous, isotropic fluid turbulence is still continuing; and studies of it lag far behind their analogs for the multiscaling of equal-time velocity structure functions [5]. There are three major reasons for this:

1. The multiscaling of equal-time velocity structure functions in fluid turbulence is far more complex than the scaling of equal-time correlation functions in critical phenomena [5].
2. The dynamic scaling of Eulerian-velocity structure functions is dominated by sweeping effects that relate temporal and spatial scales linearly and thus lead to a trivial dynamic-scaling exponent $z_{\mathcal{E}} = 1$, where the subscript \mathcal{E} stands for Eulerian.
3. Even if this dominant temporal scaling because of sweeping effects is removed (see below), time-dependent velocity structure functions do not have simple scaling forms.

The first and second points above have already been discussed in Chapter 1. The third point was perhaps first recognised in Ref. [6], where it was stressed that in the fluid-turbulence context, an infinity of dynamic-multiscaling exponents is required. These are related to the equal-time multiscaling exponents by *bridge relations*. However, the crucial point about dynamic multiscaling, not enunciated clearly hitherto, though partially implicit in Refs. [6, 7, 8], is that *different ways of extracting time scales* from time-dependent velocity structure functions yield *different dynamic-multiscaling exponents* that are related to the equal-time multiscaling exponents by *different classes of bridge relations*. This implies that, unlike time-dependent correlation functions, Eq. (2.4), in critical phenomenon, scaling collapse of time-dependent structure functions does not occur in fluid turbulence.

This breakdown of simple dynamic scaling is a crucial characteristic of dynamic multiscaling.

One class of bridge-relations was previously obtained in Ref. [6]. In the forced-Burgers-turbulence context a few bridge relations of another class were obtained in Refs. [7, 8]. If the bridge relations of Refs. [6] and [7, 8] are compared naively, then they disagree with each other. We systematise such bridge relations by distinguishing three types of methods that can be used to extract time scales; these are based, respectively, on *integral* I, *derivative* D, and *exit-time* E scales. We then derive the bridge relations for dynamic-multiscaling exponents for these three methods. Our method of systematisation resolves the apparent contradiction between the bridge-relations in Ref [6] and Refs. [7, 8]. Finally we check by an extensive numerical simulation that such bridge relations are satisfied in the GOY shell model for fluid turbulence.

2.2 Dynamic structure functions

To proceed further let us recall that in homogeneous, isotropic turbulence, the equal-time, order- p , velocity structure function

$$\mathcal{S}_p(\ell) \equiv \langle [\delta u_{\parallel}(\vec{x}, t, \ell)]^p \rangle \sim \ell^{\zeta_p}; \quad (2.5)$$

$$\delta u_{\parallel}(\vec{x}, t, \ell) = [\vec{u}(\vec{x} + \vec{\ell}, t) - \vec{u}(\vec{x}, t)] \cdot \left(\frac{\vec{\ell}}{\ell}\right). \quad (2.6)$$

Where the scaling behaviour holds for ℓ in the inertial range, i.e. $\eta_d \ll \ell \ll L$. Here $\vec{u}(\vec{x}, t)$ is the Eulerian fluid velocity at point \vec{x} and time t , L is the large spatial scale at which energy is injected into the system, η_d is the dissipation scale, ζ_p is the order- p , equal-time multiscaling exponent, and the angular brackets denote an average over the statistical steady state of the turbulent fluid. The 1941 theory (K41) of Kolmogorov [9] yields the simple scaling result $\zeta_p^{K41} = p/3$. However, experiments and simulations indicate multiscaling, i.e., ζ_p is a nonlinear, convex

function of p ; and the von-Kármán-Howarth relation [5] yields $\zeta_3 = 1$. For further details see Chapter 1.

To study dynamic multiscaling we use the longitudinal, time-dependent, order- p structure function [6]

$$\mathcal{F}_p(\ell, \{t_1, \dots, t_p\}) \equiv \langle [\delta u_{\parallel}(\vec{x}, t_1, \ell) \dots \delta u_{\parallel}(\vec{x}, t_p, \ell)] \rangle. \quad (2.7)$$

Clearly,

$$\mathcal{F}_p(\ell, \{t_1 = \dots = t_p = 0\}) = \mathcal{S}_p(\ell). \quad (2.8)$$

We normally restrict ourselves to the simple case $t_1 = t_2 = \dots = t_q \equiv t$ and $t_{q+1} = t_{q+2} = \dots = t_p = 0$, for notational simplicity write $\mathcal{F}_p(\ell, t)$, and suppress the q dependence which should not affect dynamic-multiscaling exponents (see below). To remove the sweeping effects mentioned before, we must of course use quasi-Lagrangian [6, 10] or Lagrangian [11] velocities in Eq. (2.7), but we do not show this explicitly here for notational convenience. Given $\mathcal{F}_p(\ell, t)$, we can extract a characteristic time scale $\tau_p(\ell)$ in several different ways, as we describe later. We can generalise Eq. (2.3) and make the dynamic-multiscaling ansatz

$$\tau_p(\ell) \sim \ell^{z_p} \quad (2.9)$$

which can now be used to determine the order- p *dynamic-multiscaling exponents* z_p . Let us first start by a naive extension of K41 phenomenology to dynamic scaling. The characteristic time scale of an eddy of size ℓ is

$$\tau(\ell) = \delta u(\ell)/\ell, \quad (2.10)$$

where $\delta u(\ell)$ is the characteristic velocity fluctuation of an eddy of size ℓ . By the K41 phenomenology

$$\delta u(\ell) \sim \ell^{1/3}, \quad (2.11)$$

which gives, $z_p^{\text{K41}} = 2/3$ for all p . This result was perhaps first emphasized by Onsager.

On the other hand in a typical experiment in a wind tunnel the velocity is measured at one point in space and a time-series of the velocity is obtained. This is an Eulerian measurement. It is assumed that the mean velocity of the flow is high enough, such that time differences can be converted to length differences via the mean flow velocity. This implies that typical length and time scales are related linearly giving a dynamic scaling exponent of

$$z_p^{\mathcal{E}} = 1. \quad (2.12)$$

Even in direct numerical simulation (DNS) of homogeneous and isotropic turbulent flows, where there is no mean flow, there are still eddies of about system size which advect the small scale eddies. Hence we expect that for Eulerian velocities we should always obtain a dynamic scaling exponent of unity, Eq. (2.12). The K41 prediction hold for Lagrangian or quasi-Lagrangian velocities. In the next Section we go beyond the simple K41 phenomenology and try to see the prediction of the multifractal model for non-trivial dynamic multiscaling of Lagrangian or quasi-Lagrangian velocity time-dependent structure functions.

2.3 Multifractal formalism for dynamic multiscaling

In the multifractal model [5], discussed in detail in Ref. [5] and Chapter 1, the velocity of a turbulent flow is assumed to possess a range of universal scaling exponents

$$h \in \mathcal{I} \equiv (h_{\min}, h_{\max}). \quad (2.13)$$

For each h in this range, there exists a set $\Sigma_h \subset \mathbb{R}^3$ of fractal dimension $D(h)$, such that

$$\frac{\delta u(\vec{r}, \ell)}{u_L} \propto \left(\frac{\ell}{L}\right)^h \quad (2.14)$$

for $\vec{r} \in \Sigma_h$, with u_L the velocity at the forcing scale L , whence

$$\frac{S_p(\ell)}{u_L^p} \equiv \frac{\langle \delta u^p(\ell) \rangle}{u_L^p} \propto \int_{\mathcal{I}} d\mu(h) \left(\frac{\ell}{L}\right)^{z(h)}, \quad (2.15)$$

where $\mathcal{Z}(h) = [ph + 3 - D(h)]$, the measure $d\mu(h)$ gives the weight of the fractal sets, and a saddle-point evaluation of the integral yields $\zeta_p = \inf_h[\mathcal{Z}(h)]$. The ph term in $\mathcal{Z}(h)$ comes from p factors of (ℓ/L) in Eq. (2.15); the $3 - D(h)$ term comes from an additional factor of $(\ell/L)^{3-D(h)}$, which is the probability of being within a distance $\sim \ell$ of the set Σ_h of dimension $D(h)$ that is embedded in three dimensions.

For the time-dependent structure function, we assume that for a fixed h , there is a characteristic decay time $\tau(h)$. Thus we write

$$\frac{\mathcal{F}_p(\ell, t)}{u_L^p} \propto \int_{\mathcal{I}} d\mu(h) \left(\frac{\ell}{L}\right)^{\mathcal{Z}(h)} \mathcal{G}^{p,h}\left(\frac{t}{\tau_{p,h}}\right), \quad (2.16)$$

where we assume the function $\mathcal{G}^{p,h}(\frac{t}{\tau_{p,h}})$ to have the same functional form for all p and h ; and $\mathcal{G}^{p,h}(0) = 1$. For a fixed h , we assume the characteristic decay time, $\tau_{p,h}$, to have the following form,

$$\tau_{p,h} \sim \ell/\delta u(\ell) \sim \ell^{1-h}. \quad (2.17)$$

Eq. (2.17) is a crucial step in our argument. Here we have assumed a simple scaling form for $\tau_{p,h}$, which follows from purely dimensional arguments. This scaling behaviour, Eq. (2.17), should of course be taken as the leading behaviour. The amplitude of ℓ^{1-h} , or sub-leading terms can, in principle depend on p , but this does not change our conclusions for the dynamic multiscaling exponents as given below.

If $\int_0^\infty t^{(M-1)} \mathcal{G}^{p,h} dt$ exists, we can define the order- p , degree- M , *integral* time scale

$$\mathcal{T}_{p,M}^I(\ell) \equiv \left[\frac{1}{\mathcal{S}_p(\ell)} \int_0^\infty \mathcal{F}_p(\ell, t) t^{(M-1)} dt \right]^{(1/M)}. \quad (2.18)$$

We can now define the *integral* dynamic-multiscaling exponents $z_{p,M}^I$ via

$$\mathcal{T}_{p,M}^I \sim \ell^{z_{p,M}^I}. \quad (2.19)$$

By substituting the multifractal form (2.16) in Eq. (2.18), computing the time integral first, and then performing the integration over the multifractal measure by the saddle-point method, we obtain the *integral* bridge relations

$$z_{p,M}^I = 1 + [\zeta_{p-M} - \zeta_p]/M, \quad (2.20)$$

which was first obtained in Ref. [6]. Likewise, if $\frac{\partial^M}{\partial t^M} \mathcal{G}^{p,h}|_{t=0}$ exists³ we can define the order- p , degree- M , *derivative* time scale

$$\mathcal{T}_{p,M}^D \equiv \left[\frac{1}{\mathcal{S}_p(\ell)} \frac{\partial^M}{\partial t^M} \mathcal{F}_p(\ell, t) \Big|_{t=0} \right]^{(-1/M)}, \quad (2.21)$$

and the *derivative* dynamic-multiscaling exponents $z_{p,M}^D$ via $\mathcal{T}_{p,M}^D \sim \ell^{z_{p,M}^D}$, and thence obtain the *derivative* bridge relation

$$z_{p,M}^D = 1 + [\zeta_p - \zeta_{p+M}]/M. \quad (2.22)$$

Such derivative bridge relations, for the special cases (a) $p = 2, M = 1$ and (b) $p = 2, M = 2$, were first obtained in the forced-Burgers-turbulence context in Refs. [8] and [7], respectively⁴, without using quasi-Lagrangian velocities but by using other methods to suppress sweeping effects. Case (a) yields the interesting result $z_{2,1}^D = \zeta_2$, since $\zeta_3 = 1$. Both relations (2.20) and (2.22) reduce to $z_p^{K41} = 2/3$ if we assume K41 scaling for the equal-time structure functions.

To have a better understanding, we have plotted $z_{p,1}^I$ and $z_{p,2}^D$ from Eqs. (2.20 and 2.22) using the She-Leveque formula for the ζ_p s, in Fig. (2.1). Note that the two different varieties of dynamic scaling exponents differ more drastically for lower values of p , thus we have here a prediction of the multifractal model which can be verified for lower values of p .

³The assumptions about existence of appropriate derivatives and integrals is crucial. Our numerical study shows that the first order time derivative of the $\mathcal{F}_p(\ell, t)$ at $t = 0$, is close to zero. It can be proved from the Navier-Stokes equation that $\frac{\partial}{\partial t} \mathcal{F}_2(\ell, t) = 0$ at $t = 0$ [11]. For the Kraichnan model of passive scalar turbulence, we can analytically show that derivatives of order higher than one do not exist, and hence the corresponding bridge-relations are meaningless.

⁴In Ref. [7] case (b) appears as a sub-dominant contribution to the dominant sweeping contribution.

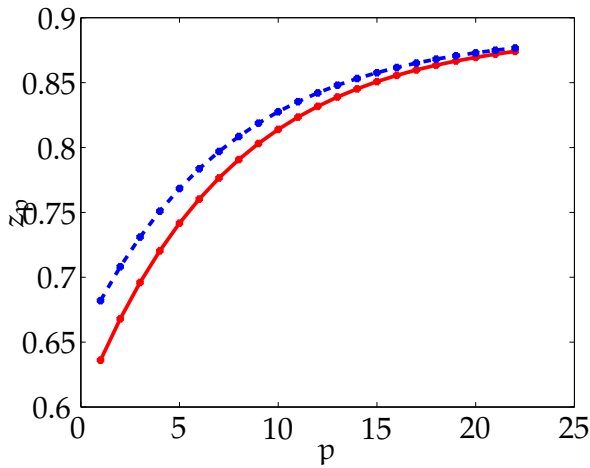


Figure 2.1: Plot of $z_{p,1}^I$ (continuous line) and $z_{p,2}^D$ (broken line) from Eqs. (2.20 and 2.22) using the She-Leveque formula for the $\zeta_{p,s}$. Note that the difference between the two curves is more for lower values of p .

2.3.1 Several time-arguments

If we consider n non-zero time arguments for the structure function, $\mathcal{F}_{p,n}(\ell, t_1, \dots, t_n, \dots, 0, \dots, 0)$, which we denote by $\mathcal{F}_{p,n}(\ell, t_1, \dots, t_n)$ for notational simplicity, we can define the integral time scale,

$$\mathcal{T}_{p,M,n}^I(\ell) \equiv \left[\frac{1}{\mathcal{S}_p(\ell)} \int_0^\infty \mathcal{F}_p(\ell, t_1, \dots, t_n) t_1^{m_1-1} dt_1 \dots t_n^{m_n-1} dt_n \right]^{1/(Mn)}, \quad (2.23)$$

and the derivative time scale,

$$\mathcal{T}_{p,M,n}^D(\ell) \equiv \left[\frac{1}{\mathcal{S}_p(\ell)} \frac{\partial^{m_1}}{\partial t_1^{m_1}} \dots \frac{\partial^{m_n}}{\partial t_n^{m_n}} \mathcal{F}_p(\ell, t_1, \dots, t_n) \Big|_{t_1=0, \dots, t_n=0} \right]^{-1/(Mn)}, \quad (2.24)$$

where $M = \sum_{i=1}^n m_i$. From these we can obtain, as above, two generalised bridge relations :

$$z_{p,M,n}^I = 1 + (\zeta_{p-nM} - \zeta_p)/(nM); \quad (2.25)$$

$$z_{p,M,n}^D = 1 + (\zeta_p - \zeta_{p+nM})/(nM). \quad (2.26)$$

2.4 GOY shell model

2.4.1 Multiscaling of equal-time structure functions

Next we check our bridge-relations by numerically calculating time-dependent structure functions of the GOY shell model for fluid turbulence [5, 12, 13, 14]:

$$\left[\frac{d}{dt} + \nu k_n^2\right] u_n = i[a_n u_{n+1} u_{n+2} + b_n u_{n-1} u_{n+1} + c_n u_{n-1} u_{n-2}]^* + f_n. \quad (2.27)$$

Here the complex, scalar velocity u_n , for the shell n , depends on the one-dimensional, logarithmically spaced wave-vectors $k_n = k_0 2^n$, complex conjugation is denoted by $*$, and the coefficients $a_n = k_n$, $b_n = -\delta k_{n-1}$, and $c_n = -(1 - \delta)k_{n-2}$, with $\delta = 1/2$, are chosen to conserve the shell-model analogues of energy and helicity in the inviscid, unforced limit. By construction, the velocity in a given shell is affected directly only by velocities in nearest- and next-nearest-neighbour shells. By contrast, all Fourier modes of the velocity field interact with each other in the Navier-Stokes equation as can be seen easily by writing it in wave-vector space. Thus the GOY shell model does not have the sweeping effect by which modes (eddies) corresponding to the largest length scales affect all those at smaller length scales *directly*. Hence it has been suggested that the GOY shell model should be thought of as a model for quasi-Lagrangian velocities [15]. We might anticipate therefore that GOY-model structure functions should not have the trivial dynamic scaling associated with Eulerian velocities; we show this explicitly below.

We integrate the GOY model (2.27) by using the slaved, Adams-Bashforth scheme [16, 17], discussed in Appendix, and 22 shells ($1 \leq n \leq 22$), with $f_n = 0$ for $n \geq 2$ and $f_1 = (1 + i) \times 5 \times 10^{-3}$ (Table 2.1). The equal-time structure function of order- p and the associated exponent is defined by

$$S_p(k_n) = \langle |u_n|^p \rangle \sim k_n^{-\zeta_p}. \quad (2.28)$$

Fig. (2.2) shows (in log-log scale) the equal-time structure functions calculated

ν	δt	λ	u_{rms}	Re_λ	L_{int}	τ_L	T_{tr}	T_{av}
10^{-7}	2×10^{-4}	0.7	0.35	2×10^6	6.3	$10^5 \delta t$	$5 \times 10^4 \delta t$	$10^5 \tau_L$

Table 2.1: Viscosity ν , the time-step δt , Taylor microscale $\lambda \equiv (\sum_n |u_n|^2 / k_n / \sum_n k_n |u_n|^2)^{1/2}$, the root-mean-square velocity $u_{rms} \equiv [2 \sum_n |u_n|^2 / k_n / (2\pi k_1)]^{1/2}$, the Taylor-microscale Reynolds number $Re_\lambda \equiv \lambda u_{rms} / \nu$, the integral scale $L_{int} \equiv (\sum_n |u_n|^2 / k_n^2) / (\sum_n |u_n|^2 / k_n)$, and the box-size eddy turnover time $\tau_L \equiv L_{int} / u_{rms}$, that we use in our numerical simulation of the GOY shell model. Data from the first T_{tr} time steps are discarded so that transients can die down. We then average our data for time-dependent structure functions for an averaging time T_{av} .

from our simulations. Note that there is a 3-cycle with the shell index n , clearly visible in this figure. This is a well known peculiar feature of the GOY shell model, which is effectively filtered out [14] if instead of S_p we use

$$\Sigma_p(k_n) \equiv \langle |\mathfrak{J}(u_{n+2}u_{n+1}u_n - (1/4)u_{n-1}u_nu_{n+1})|^{p/3} \rangle \sim k_n^{-\zeta_p}, \quad (2.29)$$

to determine ζ_p . In Fig (2.3) we have plotted $\Sigma_p(k_n)$ versus k_n in log-log scale. A least-square fit to the linear region of this plot the equal-time multiscaling exponents ζ_p are extracted. These exponents are in close agreement with those found for homogeneous, isotropic fluid turbulence in three dimension [14]. Data for the exponents ζ_p from our calculations are given in Table 2.2.

2.4.2 Extended Self Similarity

Another well known method for filtering out the three-cycle mentioned above is to plot $S_p(k_n)$ versus $S_3(k_n)$ on a log-log scale. This is called *extended self-similarity* (ESS). ESS is also useful in analysing structure functions obtained from DNS studies of Navier-Stokes equation or actual experimental data. In particular, a log-log plot of real-space equal-time structure function $S_p(\ell)$ versus ℓ , for $p > 2$, shows scaling for the range of ℓ close to a decade⁵. But, in ESS plots, where $\log[S_p(\ell)]$ is plotted against $\log[S_3(\ell)]$, scaling behaviour is observed for

⁵The situation is far worse in DNS than in experiments because DNS at present cannot reach very high Reynolds numbers due to computational limitations.

much larger range allowing a far more accurate determination of the equal-time multiscaling exponent ratios ζ_p/ζ_3 . Since $\zeta_3 = 1$ by the von-Kármán-Howarth relation, this yields ζ_p . While studying dynamic multiscaling exponents it would be most useful to have a dynamic analogue of ESS. This question is investigated at the end of this Chapter.

2.4.3 Time-dependent structure functions

We analyse the velocity $u_n(t)$ time-series for $n = 4$ to 13, which corresponds to wave-vectors well within the inertial range. The smaller the wave-vector k_n the slower is the evolution of $u_n(t)$, so it is important to use different temporal sampling rates for velocities in different shells. We use sampling rates of $50 \times \delta t$ for $4 \leq n \leq 8$ and $10 \times \delta t$ for $9 \leq n \leq 13$, respectively.

For the GOY shell model we use the normalised, order- p , complex, time-dependent structure function,

$$f_p(n, t) \equiv \frac{1}{S_p(k_n)} \langle [u_n(0)u_n^*(t)]^{p/2} \rangle, \quad (2.30)$$

which has both real and imaginary parts. The representative plot of Fig. 2.5 shows that the imaginary part of $f_p(n, t)$ is negligibly small compared to its real part. Observe that $f_p(n, -t) = f_p^*(n, t)$ by assuming time-translational invariance. Hence a vanishing imaginary part of $f_p(n, t)$ would imply time reflection symmetry for $f_p(n, t)$.

We work with the real part of $f_p(n, t)$, i.e.,

$$F_p(n, t) \equiv \Re[f_p(n, t)]. \quad (2.31)$$

Representative plots of $F_p(n, t)$ are shown in Fig. (2.6). Integral and derivative time scales can be defined for the shell model (2.27) as in Eqs. (2.18) and (2.21).

We now concentrate on the integral time scale with $M = 1$,

$$T_{p,1}^I(n, t_u) \equiv \int_0^{t_u} F_p(n, t) dt, \quad (2.32)$$

the derivative time scale with $M = 2$,

$$T_{p,2}^D \equiv \left[\frac{\partial^2 F_p(n, t)}{\partial t^2} \Big|_{t=0} \right]^{-1/2}, \quad (2.33)$$

and the associated dynamic-multiscaling exponents defined via $T_{p,1}^I(n, t_u) \sim k_n^{-z_{p,1}^I}$ and $T_{p,2}^D(n) \sim k_n^{-z_{p,2}^D}$. In principle we should use $t_u \rightarrow \infty$ but, since it is not possible to obtain $F_p(n, t)$ accurately for large t , we select an upper cut-off t_u such that $F_p(n, t_u) = \alpha$, where, for all n and p , we choose $\alpha = 0.7$ in the results we report. We have checked that our results do not change if we use $0.3 < \alpha < 0.8$. The slope of a log-log plot of $T_{p,1}^I(n)$ versus k_n now yields $z_{p,1}^I$ (Fig. 2.7 and Table 2.2). Preliminary data for $z_{p,1}^I$ were reported by us in Ref. [2].

For extracting the derivative scale $T_{p,2}^D$ we extend $F_p(n, t)$ to negative t via $F_p(n, -t) = F_p(n, t)$ and use a centred, sixth-order, finite-difference scheme to find $\frac{\partial^2}{\partial t^2} F_p(n, t) \Big|_{t=0}$. A log-log plot of $T_{p,2}^D(n)$ versus k_n now yields the exponent $z_{p,2}^D$ (Fig. 2.8 and Table 2.2).

2.4.4 Exit-time analysis

In Ref. [15] dynamic-multiscaling exponents were extracted not from time-dependent structure functions but by using the following exit-time algorithm: We define the decorrelation time for shell n , at time t_i , to be $T_i(n)$, such that,

$$|u_n(t_i)| |u_n(t_i + T_i)| \geq \lambda^{\pm 1} |u_n(t_i)|^2, \quad (2.34)$$

with $0 < \lambda < 1$. The exit-time scale of order- p and degree- M for the shell k_n is

$$T_{p,M}^E \equiv \lim_{N \rightarrow \infty} \left[\frac{\frac{1}{N} \sum_{i=1}^N T_i^M |u_n(t_i)|^p}{\frac{1}{N} \sum_{i=1}^N |u_n(t_i)|^p} \right]^{(1/M)} \sim k_n^{-z_{p,M}^E}, \quad (2.35)$$

where the last proportionality follows from the dynamic-multiscaling ansatz. In practise we cannot of course take the limit $N \rightarrow \infty$; in a typical run of length T_{av} (Table 2.1) $N \simeq 10^9$. By suitably adapting the multifractal formalism used above, we get the exit-time bridge relation

$$z_{p,M}^E = 1 + [\zeta_{p-M} - \zeta_p]/M, \quad (2.36)$$

obtained in Ref. [15] only for $M = 1$. We have used this algorithm to extract the exit-time for $M = 1$ [see Fig. (2.9)] and $M = -2$ [see Fig. (2.10)], which obeys the same bridge relations as $T_{p,1}^I$ and $T_{p,2}^D$ respectively. Dynamic-multiscaling exponents obtained via this exit-time algorithm are shown for $M = 1$ and $M = -2$ in Table 2.2. The exit-time bridge relations for $M > 0$ are the analogs of the integral-time bridge relation (2.20) and those for $M < 0$ are the analogs of the derivative-time bridge relation (2.22). We have checked that our results do not depend on λ for $0.3 < \lambda < 0.8$.

Our numerical results for the equal-time exponents ζ_p (Column 2), the integral-time exponents $z_{p,1}^I$ (Columns 3 and 4), the derivative-time exponents $z_{p,2}^D$ (Columns 6 and 7), and the exit-time exponents $z_{p,1}^E$ and $z_{p,-2}^E$ (Columns 5 and 8, respectively) for $1 \leq p \leq 6$ are given in Table 2.2. The agreement of the exponents in Columns 3 and 4 shows that the bridge relation (2.20) is satisfied (within error bars). Likewise, a comparison of Columns 6 and 7 shows that the bridge relation (2.22) is satisfied. By comparing Columns 4 and 5 we see that the integral-time exponent $z_{p,1}^I$ is the same as the exit-time exponent $z_{p,1}^E$; similarly, Columns 7 and 8 show that the derivative-time exponent $z_{p,2}^D$ is the same as the exit-time exponent $z_{p,-2}^E$. The relation $z_{2,1}^D = \zeta_2$ mentioned above [8] is not meaningful in the GOY model since $\partial F_p(n, t)/\partial t|_{t=0}$ vanishes, at least at the level of accuracy of our numerical study.

We have obtained 50 different values of each of the dynamic-multiscaling exponents from 50 different initial conditions. For each of these initial conditions time-averaging is done over a time T_{av} (Table 2.1) which is larger than the averaging time of Ref. [15] by a factor of about 10^4 . The means of these 50 values for each of the dynamic-multiscaling exponents are shown in Table 2.2; and the standard deviation yields the error. This averaging is another way of removing the effects of the 3-cycle mentioned above.

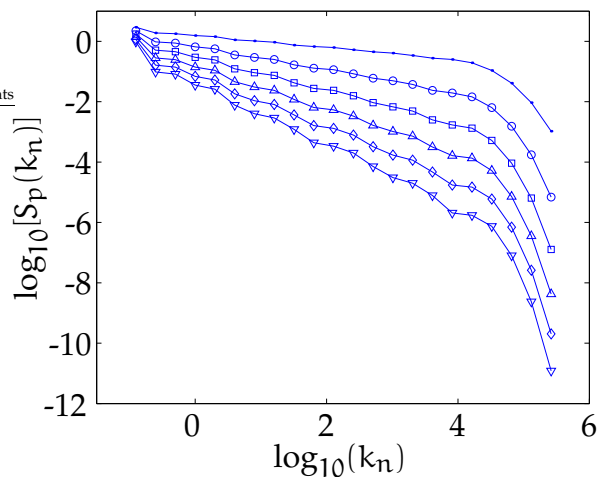


Figure 2.2: $\log - \log$ Plot of $S_p(k_n)$ versus k_n from our simulation of GOY shell model. (From top to bottom $p = 1$ to 6.) Note the three-cycles present in the plot. The parameters of simulation are given in Table(2.1).

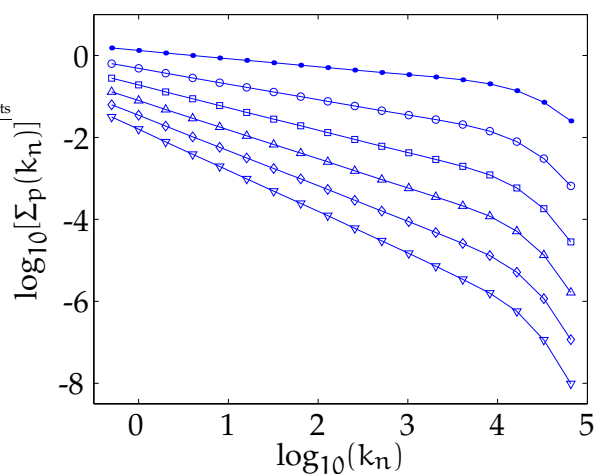


Figure 2.3: $\log - \log$ Plot of $\Sigma_p(k_n)$ versus p from our simulation of GOY shell model. (From top to bottom $p = 1$ to 6.) Compare with Fig. (2.2). The equal-time multiscaling exponents ζ_p are extracted by least-squares fitting to the linear region of this plot are listed in Table(2.2). The parameters of simulation are given in Table(2.1).

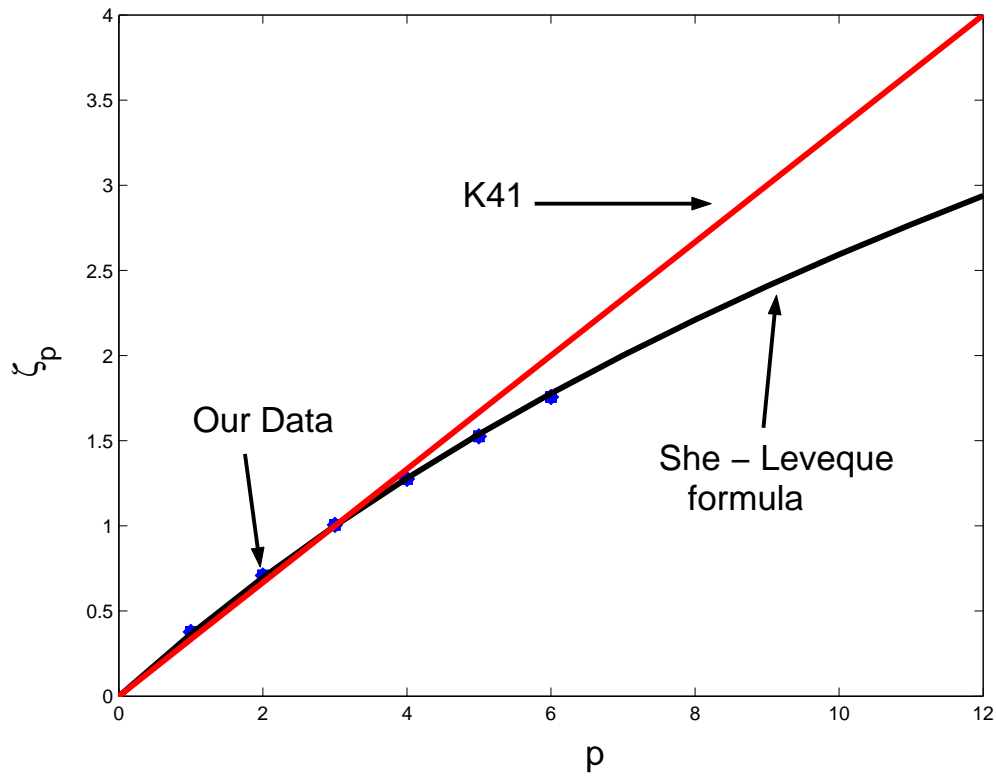


Figure 2.4: Plot of ζ_p versus p from our simulations of the GOY shell model. Our data are shown by asterix. The K41 prediction is shown the straight line in the plot. The value of ζ_p obtained from the She-Leveque formula [see Sec. (1.7.6)] is also shown in the plot.

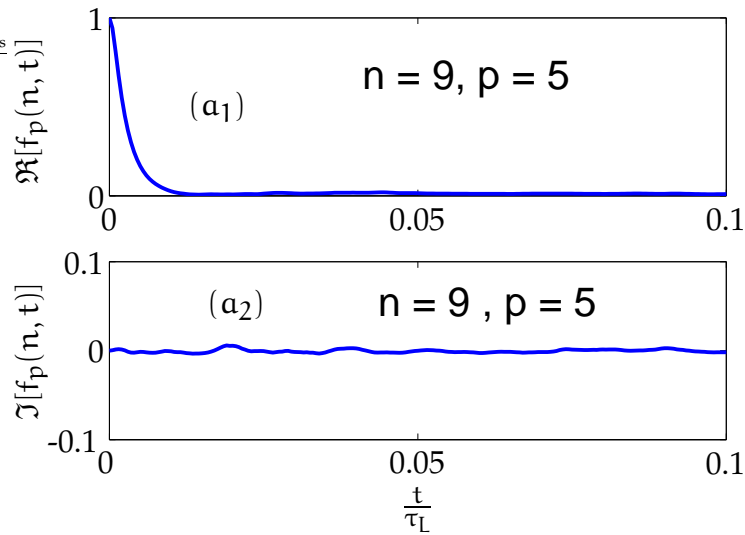


Figure 2.5: Plots of real (a_1) and imaginary (a_2) parts of the time-dependent structure function $f_p(n, t)$ for the GOY shell model for shell number $n = 9$ and order $p = 5$ versus time t/τ_L , where τ_L is the box-size eddy turnover time (Table 2.1). Note that $\Im[f_p(n, t)]$ is negligibly small compared to $F_p(n, t) = \Re[f_p(n, t)]$.

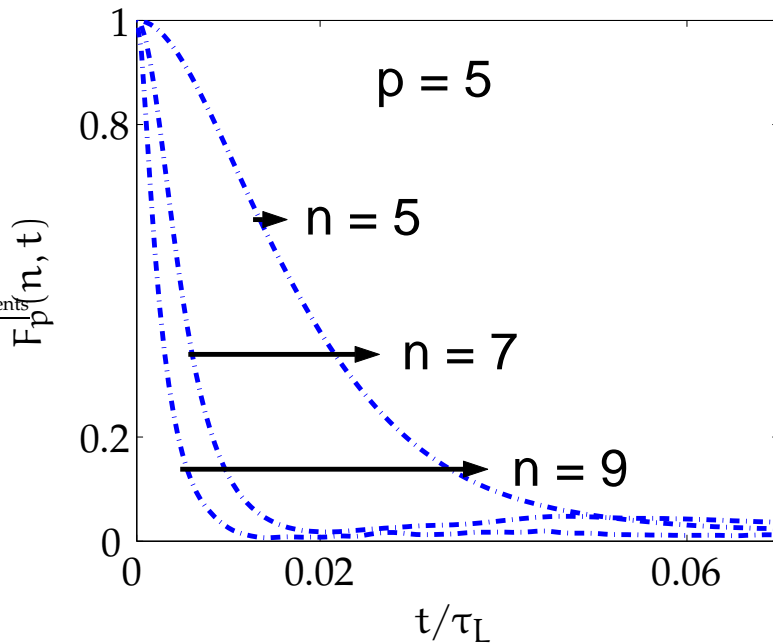


Figure 2.6: $F_p(n, t)$ versus t/τ_L for $p = 5$ and $n = 5, 7$, and 9 .

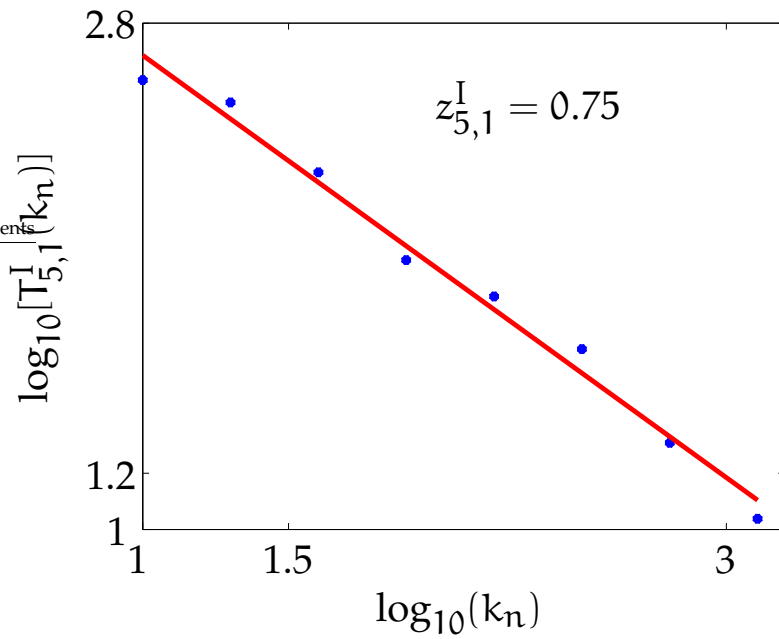


Figure 2.7: Representative plot of the integral time scales $T_{5,1}^I(n)$ versus k_n (in log-log scale); the slopes of the linear least-square fits yield the dynamic exponents $z_{5,1}^I$.

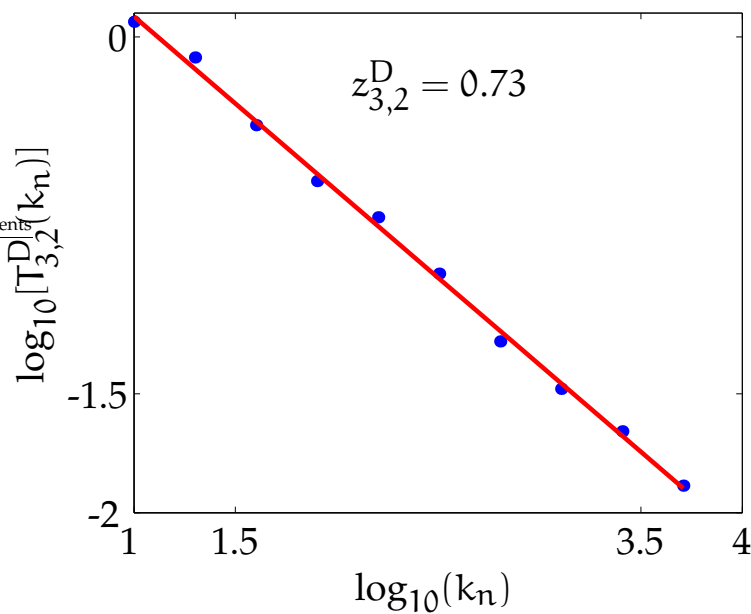


Figure 2.8: Representative plot of the derivative time scales $T_{3,2}^D(n)$ versus k_n (in log-log scale); the slopes of the linear least-square fits yield the dynamic exponents $z_{3,2}^D$.

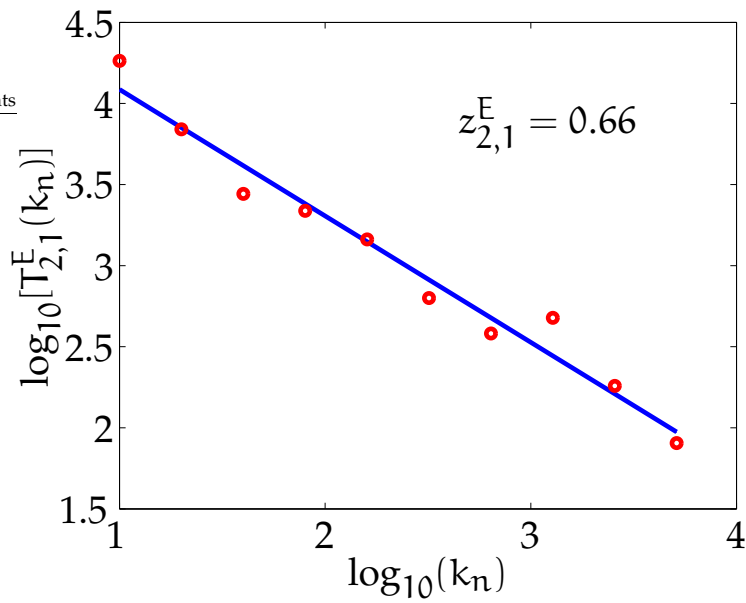


Figure 2.9: Representative plot of the exit time scales $T_{2,1}^E(k_n)$ versus k_n (in log-log scale); the slopes of the linear least-square fits yield the dynamic exponents $z_{2,1}^E$.

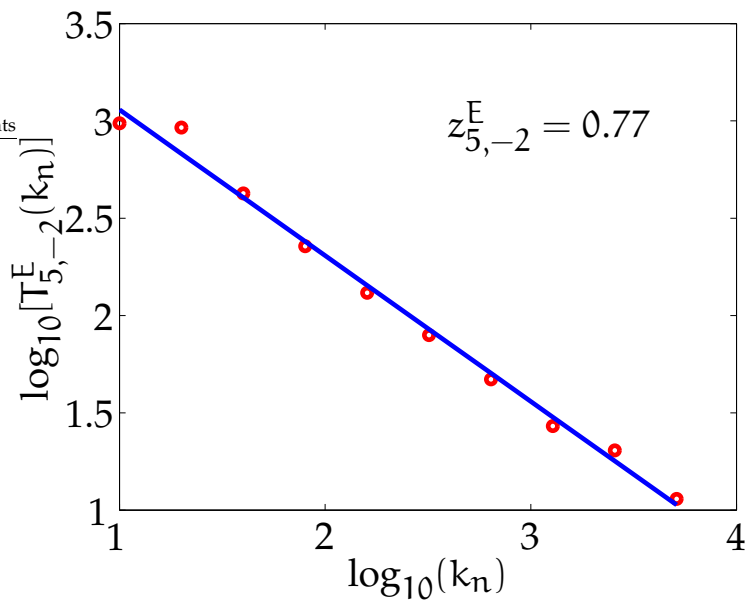


Figure 2.10: Representative plot of the exit time scales $T_{5,-2}^E(k_n)$ versus k_n (in log-log scale); the slopes of the linear least-square fits yield the dynamic exponents $z_{5,-2}^E$.

order(p)	ζ_p	$z_{p,1}^I$ [Eq.(2.20)]	$z_{p,1}^I$	$z_{p,1}^E$	$z_{p,2}^D$ [Eq.(2.22)]	$z_{p,2}^D$	$z_{p,-2}^E$
1	0.3777 ± 0.0001	0.6221 ± 0.0001	0.60 ± 0.02	0.603 ± 0.007	0.6820 ± 0.0001	0.70 ± 0.02	0.677 ± 0.001
2	0.7091 ± 0.0001	0.6686 ± 0.0002	0.67 ± 0.02	0.661 ± 0.007	0.7081 ± 0.0002	0.71 ± 0.01	0.719 ± 0.004
3	1.0059 ± 0.0001	0.7030 ± 0.0002	0.701 ± 0.009	0.708 ± 0.001	0.7310 ± 0.0002	0.73 ± 0.01	0.739 ± 0.006
4	1.2762 ± 0.0002	0.7298 ± 0.0003	0.727 ± 0.007	0.74 ± 0.01	0.7509 ± 0.0003	0.744 ± 0.009	0.758 ± 0.006
5	1.5254 ± 0.0005	0.7511 ± 0.0007	0.759 ± 0.009	0.77 ± 0.01	0.7684 ± 0.0007	0.756 ± 0.009	0.778 ± 0.003
6	1.757 ± 0.001	0.768 ± 0.002	0.77 ± 0.01	0.79 ± 0.01	0.7836 ± 0.002	0.764 ± 0.009	0.797 ± 0.0008

Table 2.2: Order- p (Column 1) multiscaling exponents for $1 \leq p \leq 6$ from our simulations of the GOY model: equal-time exponents ζ_p (Column 2), integral-scale dynamic-multiscaling exponent $z_{p,1}^I$ of degree-1 (Column 3) from the bridge relation (2.20) and the values of ζ_p in Column 1, $z_{p,1}^I$ from our calculation using time-dependent structure functions (Column 4), the exit-time exponents of order 1 $z_{p,1}^E$ (Column 5), the derivative-time exponents $z_{p,2}^D$ (Column 6) from the bridge relation (2.22) and the values of ζ_p in Column 1, $z_{p,2}^D$ from our calculation using time-dependent structure function (Column 7) and the exit-time exponent of order -2 , $z_{p,-2}^E$ (Column 8). The error estimates are obtained as described in the text.

2.5 Dynamic ESS

Inspired by the ESS method used to extract scaling exponents from equal-time structure functions, we have tried dynamic counterpart of ESS here. This can be done in two different ways:

1. Instead of plotting $\log[T_{p,M}(k_n)]$ versus $\log(k_n)$ we plot $\log[T_{p,M}(k_n)]$ versus $\log[S_3(k_n)]$. We have checked that this kind of ESS does not help in removing the three cycle present in our data, nor does it increase the scaling ranges substantially.
2. We plot $\log[T_{p,M}(k_n)]$ versus $\log[T_{2,M}(k_n)]$. This form of dynamic ESS filters out the effect of the three cycle to some extent; however, the extension of the scaling range is only marginal as can be seen from comparing Fig. (2.11) and Fig. (2.12).

Hence we conclude that there seems to be no good dynamic analogue of ESS at least in the GOY shell model.

2.6 Conclusion

We have shown systematically how different ways of extracting time scales from time-dependent velocity structure functions or time series can lead to different sets of dynamic-multiscaling exponents, which are related in turn to the equal-time multiscaling exponents ζ_p by different classes of bridge relations. Our extensive numerical study of the GOY shell model for fluid turbulence verifies explicitly that such bridge relations hold. Experimental studies of Lagrangian quantities in turbulence have been increasing over the past few years [18, 19, 20]. We hope our work will stimulate studies of dynamic multiscaling in such experiments. Furthermore, the sorts of bridge relations we have discussed here must also hold in other problems with multiscaling of equal-time and time-dependent

structure functions or correlation functions. Passive-scalar and magneto-hydrodynamic turbulence are two obvious examples. Dynamic multiscaling in passive-scalar turbulence shall be discussed in the next chapter. Numerical studies of time-dependent, quasi-Lagrangian-velocity structure functions in the Navier-Stokes equation, will be discussed in Chapter 5.

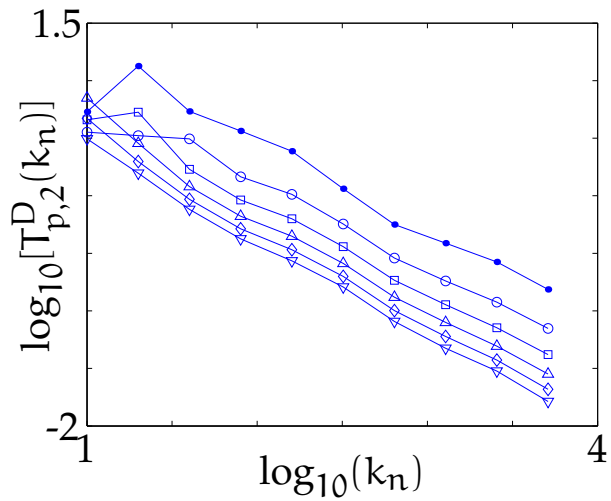


Figure 2.11: Representative log – log plot of the derivative time scales $T_{p,2}^D(k_n)$ versus k_n . The order p goes from 1 (filled circles) to 6 (upside down triangles) as we go from the top curve to the bottom curve.

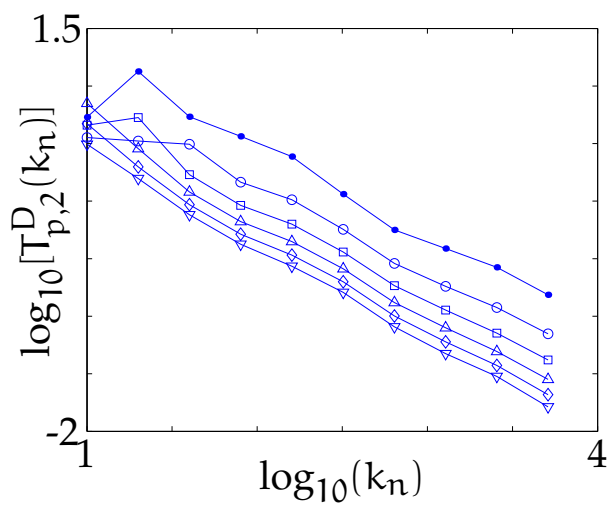


Figure 2.12: Representative plot of $T_{p,2}^D(k_n)$ versus $T_{2,2}^D$ (in log – log scale). The order p goes from 1 to 6 as we go from the top curve to the bottom curve. Observe that unlike the case of equal-time structure functions, this ESS-style plot does not improve the quality of scaling substantially.

Bibliography

- [1] P. Hohenberg and B. Halperin, *Rev. Mod. Phys.* **49**, 435 (1977).
- [2] D. Mitra and R. Pandit, *Physica A* **318**, 179 (2003).
- [3] D. Mitra and R. Pandit, *Phys. Rev. Lett* **93**, 024501 (2004).
- [4] D. Stauffer, M. Ferer, and M. Wortis, *Phys. Rev. B* **6**, 3426 (1972).
- [5] U. Frisch, *Turbulence the legacy of A.N. Kolmogorov* (Cambridge University Press, Cambridge, 1996).
- [6] V. L'vov, E. Podivilov, and I. Procaccia, *Phys. Rev. E* **55**, 7030 (1997).
- [7] F. Hayot and C. Jayaprakash, *Phys. Rev. E* **57**, R4867 (1998).
- [8] F. Hayot and C. Jayaprakash, *Int. J. Mod. Phys. B* **14**, 1781 (2000).
- [9] A. Kolmogorov, *Dokl. Acad. Nauk USSR* **30**, 9 (1941).
- [10] V. Belinicher and V. L'vov, *Sov. Phys. JETP* **66**, 303 (1987).
- [11] Y. Kaneda, T. Ishihara, and K. Gotoh, *Phys. Fluids*. **11**, 2154 (1999).
- [12] E. Gledzer, *Sov. Phys. Dokl.* **18**, 216 (1973).
- [13] K. Ohkitani and M. Yamada, *Prog. Theor. Phys.* **55**, 833 (1985).
- [14] L. Kadanoff, D. Lohse, J. Wang, and R. Benzi, *Phys. Fluids* **7**, 617 (1999).
- [15] L. Biferale, G. Bofetta, A. Celani, and F. Toschi, *Physica D* **127**, 187 (1999).

-
- [16] S. Dhar, A. Sain, and R. Pandit, *Phys. Rev. Lett.* **78**, 2964 (1997).
- [17] D. Pisarenko, L. Biferale, D. Courvoisier, U. Frisch, and M. Vergassola, *Phys. Fluids A* **5**, 2533 (1993).
- [18] S. Ott and J. Mann, *J. Fluid Mech.* **422**, 207 (2000).
- [19] A. L. Porta, G. Voth, A. Crawford, J. Alexander, and E. Bodenschatz, *Nature(London)* **409**, 1111 (2002).
- [20] N. Mordant, P. Metz, O. Michel, and J.-F. Pinton, *Phys. Rev. Lett.* **87**, 214501 (2001).

Chapter 3

Dynamic scaling and multiscaling in passive-scalar and passive-vector turbulence

3.1 Introduction

Important advances have been made over the past decade in understanding the statistical properties of the turbulence of passive scalars and passive vectors advected by a fluid (see the Review [1] and our short description in Section 1.9). If the advecting velocity is stochastic and of the Kraichnan type [2, 3, 4], then, in some limits [see page 27 and Section(3.2)], it can be established analytically that passive-scalar and passive-vector turbulence show *anomalous scaling* or *multiscaling* of structure functions. (Similar results have been found numerically, at high Reynolds numbers, if the advecting velocity is governed by the two-dimensional Navier-Stokes equation [1].) These are the only turbulence problems for which such multiscaling has been proven analytically, so it is important to use them as testing grounds for new ideas about multiscaling in turbulence. Since significant progress has been made over the past few years in the development of the theory of *dynamic multiscaling* in fluid turbulence [5, 6, 7, 8], it is our purpose here to examine what this theory implies for passive-scalar and passive-vector turbulence. For notational convenience, in this Chapter all quantities pertaining to the

velocity field has the superscript u . Quantities associated with the passive-vector field carries the superscript B . Furthermore, unless explicitly specified, all other quantities refer to the passive-scalar field.

Recall (Chapter 1) that the quest for a statistical characterisation of turbulence begins most often with the equal-time, order- p velocity structure functions

$$S_p^u(\ell) \equiv \langle [\delta u_{\parallel}(\ell)]^p \rangle, \quad (3.1)$$

$$\delta u_{\parallel}(\ell) \equiv [\vec{u}(\vec{x} + \vec{\ell}) - \vec{u}(\vec{x})] \cdot \left(\frac{\vec{\ell}}{\ell} \right), \quad (3.2)$$

i.e., the order- p moments of the probability distribution functions of longitudinal velocity differences at the length scale ℓ . The equal-time multiscaling exponents ζ_p^u for velocity differences are defined by the power law

$$S_p^u(\ell) \sim \ell^{\zeta_p^u}, \quad (3.3)$$

valid for the inertial range $\eta_d \ll \ell \ll L$, where η_d is the dissipation scale and L the length at which energy is pumped in. Simple scaling [9], developed by Kolmogorov [see Section (1.4)] in 1941 (K41), yields ${}^u\zeta_p^{K41} = p/3$, but subsequent work [10] suggests significant corrections for $p > 3$ and *multiscaling* with ζ_p^u a non-linear, convex, monotonically increasing function of p , as we have summarised in Chapter 1. The generalisation of such multiscaling to *dynamic multiscaling* is subtle and has been systematised only recently [5, 6, 7, 8] (for further details see Chapter 2). We summarise below the essential points of this generalisation since we build on it here for passive-scalar and passive-vector turbulence.

- We must not use Eulerian-velocity structure functions since they lead to trivial dynamic scaling with all dynamic exponents $z_p^{\mathcal{E}} = 1$ [11], where \mathcal{E} denotes an Eulerian-velocity exponent. Nontrivial dynamic exponents z_p^u can be obtained [8] from dynamic-multiscaling ansätze of the form

$$\tau_p^u \sim \ell^{z_p^u}, \quad (3.4)$$

where the times τ_p^u are extracted from *Lagrangian* or *quasi-Lagrangian* time-dependent structure functions.

- A generalisation of the multifractal formalism [10] to the case of time-dependent structure functions [5, 7, 8] can be used to show that dynamic and equal-time multiscaling exponents must be related by simple *bridge relations*; and, most remarkably [8], these bridge relations depend crucially on how time scales are extracted from time-dependent structure functions. In particular, from the order- p time-dependent structure function, $\mathcal{F}_p^u(\ell, t)$, defined precisely in Section(2.2), we can extract integral time scale, of order- p , degree- M

$$\mathcal{T}_{p,M}^{I,u}(\ell) \equiv \left[\frac{1}{S_p^u(\ell)} \int_0^\infty \mathcal{F}_p^u(\ell, t) t^{(M-1)} dt \right]^{(1/M)} \sim \ell^{z_{p,M}^{I,u}}. \quad (3.5)$$

and thence the associated dynamic multiscaling exponent $z_{p,m}^{I,u}$. Similarly the and derivative time scale of order- p , degree- M and their corresponding dynamic scaling exponents.

$$\mathcal{T}_{p,M}^{D,u}(\ell) \equiv \left[\frac{1}{S_p^u(\ell)} \frac{\partial^M}{\partial t^M} \mathcal{F}_p^u(\ell, t) \Big|_{t=0} \right]^{(-1/M)} \ell^{z_{p,M}^{D,u}}., \quad (3.6)$$

and $z_{p,M}^{D,u}$ the associated dynamic multiscaling exponent.

- It has been shown in Chapter 2 and Ref. [8] that, for fluid turbulence, these dynamic multiscaling scaling exponents are related by the following *bridge relations* to equal-time multiscaling exponents.

$$z_{p,M}^{I,u} = 1 + [\zeta_{p-M}^u - \zeta_p^u]/M; \quad (3.7)$$

$$z_{p,M}^{D,u} = 1 + [\zeta_p^u - \zeta_{p+M}^u]/M. \quad (3.8)$$

- This implies that, in fluid turbulence, even for a fixed order p there $\mathcal{F}_p(\ell, t)$ versus t cannot be made to collapse on one another by simple scaling of the axes as is possible, e.g., for correlation functions near critical points in equi-

librium critical phenomenon. This signifies a breakdown of simple dynamic scaling [5].

Our principal results of this Chapter illustrate important principles that appear, at first sight, to be surprising. We find, e.g., that the dynamic exponents of the passive-scalar field depend via bridge relations only on the equal-time scaling exponents of the velocity field. Thus, even though equal-time structure functions for the passive-scalar and passive-vector problems display multiscaling, they show *simple dynamic scaling* if the advecting velocity is of the Kraichnan type (see later). Dynamic multiscaling is obtained only if the advecting velocity field is itself intermittent.

The rest of this Chapter is organised in the following way:

1. We first consider the Kraichnan model of passive scalar advection and calculate its dynamic scaling exponents analytically, [Section (3.2)]. We also comment on the validity of our results if the advecting velocity field is scales simply (like the Kraichnan velocity field) but is *not* white-in-time (unlike the Kraichnan velocity field).
2. In Section (3.3) we do similar calculations for a shell model for passive-scalar turbulence with a Kraichnan velocity field, for which we obtain further support in favour of our analytical results by numerical simulations. The similarities and differences between this shell model and the full advection-diffusion equation for the passive-scalar, considered in Sec (3.2) are also pointed out.
3. Next we consider a shell model for passive-scalar turbulence in which the passive-scalar is advected by velocity obeying the GOY shell model equations for fluid turbulence. In this case [Section(3.4)] we show that the multifractal model, which proved very useful in dealing with dynamic mul-

tiscaling for fluid turbulence in Chapter 2, predicts dynamic multiscaling. We confirm this result by our numerical simulations. Similar results are expected to be true for a passive-scalar advected by a velocity field governed by the Navier–Stokes equation, if we consider the passive-scalar in Lagrangian or quasi-Lagrangian frameworks.

4. And finally [Section (3.5)] we discuss the implications of our study for the passive-vector model.

3.2 Kraichnan model (Model A)

We consider several models in this Chapter beginning with the advection-diffusion equation for the passive scalar field $\theta(\vec{x}, t)$ at point \vec{x} and time t :

$$\frac{\partial}{\partial t}\theta + \vec{u} \cdot \nabla\theta = \kappa\nabla^2\theta + f_\theta, \quad (3.9)$$

where κ is the passive-scalar diffusivity and f_θ an external force. The advecting velocity \vec{u} should be obtained from solutions of the Navier-Stokes equation, but, to investigate equal-time multiscaling of passive-scalar structure functions, it has also proved very fruitful to use the *Kraichnan ensemble* in which each component of \vec{u} is a zero-mean, delta-correlated Gaussian random variable with the covariance

$$\langle u_i(\vec{x}, t)u_j(\vec{x} + \vec{\ell}, t') \rangle = 2D_{ij}(\vec{\ell})\delta(t - t') \quad (3.10)$$

and the Fourier transform of D_{ij} has the form

$$\tilde{D}_{ij}(\vec{q}) \propto \left(q^2 + \frac{1}{L^2} \right)^{-\frac{d+\xi}{2}} \exp(-\eta q^2) \left[\delta_{ij} - \frac{q_i q_j}{q^2} \right] \quad (3.11)$$

Here η plays to role of the dissipation scale and L plays the role of the large scale of forcing, i.e., the integral scale, the factor inside square brackets on the right assures incompressibility and d is the dimensionality of space. In real space

Eq. (3.11) takes the form,

$$D_{ij}(\vec{\ell}) = D^0 \delta_{ij} - \frac{1}{2} d_{ij}(\vec{\ell}), \quad (3.12)$$

and, in the limits $L \rightarrow \infty$ and $\eta \rightarrow 0$ we get the scaling form

$$d_{ij} = D_1 \ell^\xi \left((d - 1 + \xi) \delta_{ij} - \xi \frac{\ell_i \ell_j}{\ell^2} \right). \quad (3.13)$$

with D_1 a normalisation constant. The parameter ξ plays a crucial role in this model. For $0 < \xi < 2$ this model shows multiscaling for equal-time order- p structure functions. Note that the constant D^0 defined by

$$D^0 = 2 \int_0^\infty \bar{D}_{ij}(\vec{q}) d^d q \propto O(L^\xi) \quad (3.14)$$

diverges in the limit $L \rightarrow \infty$. The external force f_θ is also a zero-mean, random, Gaussian random variable which is white-in-time with the following variance:

$$\langle f_\theta(\vec{x}, t) f_\theta(\vec{y}, t') \rangle = C \left(\frac{|\vec{x} - \vec{y}|}{L} \right) \delta(t - t'), \quad (3.15)$$

where the function $C(x/L)$ is confined to large length scales only. Moreover, f_θ and u are specified to be statistically independent of each other. In this Chapter we call this model, the Kraichnan model of passive-scalar advection, **Model A**.

The equal-time multiscaling properties of this model has already been summarised in Section(1.9). In this Chapter we are principally interested in the time-dependent structure function of this model, namely,

$$\mathcal{F}_p(\vec{\ell}, \{t_1, \dots, t_p\}) \equiv \left\langle [\delta\theta(\vec{x}, t_1, \vec{\ell}) \dots \delta\theta(\vec{x}, t_p, \vec{\ell})] \right\rangle, \quad (3.16)$$

$$\delta\theta(\vec{x}, t, \vec{\ell}) = \theta(\vec{x} + \vec{\ell}, t) - \theta(\vec{x}, t). \quad (3.17)$$

Here the angular brackets denote an average over the statistics of velocity field u and the force f_θ . From this dynamic structure function $\mathcal{F}_p(\ell, t)$ we can extract a time scale $\tau_p(\ell)$ in several different ways and use the dynamic multiscaling ansatz $\tau_p(\ell) \sim \ell^{z_p}$ to find out the order- p dynamic multiscaling exponent z_p . First we use

a K41-type dimensional arguments¹ to extract z_p . The characteristic time scale for length scale ℓ is usually taken to be

$$\mathcal{T}(\ell) \sim \frac{\ell}{\delta u(\ell)}. \quad (3.18)$$

However, given the white-in-time nature of the velocity correlation we should use the spatial part of the velocity correlator, $D_{ij}(\ell)$, to define the characteristic time scale as follows:

$$\mathcal{T}(\ell) \sim \frac{\ell^2}{D_{ij}(\ell)} \sim \ell^{2-\xi}. \quad (3.19)$$

Hence $z_p = 2 - \xi$ for all p . As in the case of fluid turbulence, we expect this prediction to be valid for passive-scalar field in Lagrangian or quasi-Lagrangian framework.

We now calculate the dynamic-scaling exponent directly from the advection-diffusion equation for the passive-scalar, Eq (3.9), model A. In particular we consider the case $p = 2$:

$$\mathcal{F}_2(\ell, t) = \left\langle \left[\theta(\vec{x} + \vec{\ell}, t) - \theta(\vec{x}, t) \right] \left[\theta(\vec{x} + \vec{\ell}, 0) - \theta(\vec{x}, 0) \right] \right\rangle \quad (3.20)$$

$$= 2C(\vec{0}, t) - 2C(\vec{\ell}, t) \quad (3.21)$$

where $C(\vec{\ell}, t) = \left\langle \theta(\vec{x} + \vec{\ell}, t) \theta(\vec{x}, 0) \right\rangle$. Later in this Chapter we shall do similar calculation for a shell model of passive-scalar advected by a Kraichnan velocity field. To make the connection with the shell model clear we do our calculations in Fourier space instead of real space. Hence we consider the correlation function

$$\tilde{C}(\vec{k}, t) \equiv \left\langle \tilde{\theta}(-\vec{k}, 0) \tilde{\theta}(\vec{k}, t) \right\rangle. \quad (3.22)$$

The advection-diffusion equation for the passive-scalar, written in Fourier space, is

$$\partial_t \tilde{\theta}(\vec{k}, t) - i \int k_j \tilde{u}_j(\vec{q}, t) \tilde{\theta}(\vec{p}, t) \delta(\vec{k} - \vec{p} - \vec{q}) d^d q d^d p = -\kappa k_j k_j \tilde{\theta}(\vec{k}) + \tilde{f}_\theta(\vec{k}) \quad (3.23)$$

¹Note that, for the case of fluid turbulence similar arguments give the simple scaling result of $z_p^{K41} = 2/3$ for all p for Lagrangian or quasi-Lagrangian velocities; Eulerian velocities are expected to show $z_p = 1$ for all p . Dimensional arguments, in general, are unable to capture multiscaling.

Here tilde denotes Fourier transforms and \vec{k} , \vec{p} and \vec{q} are wavevectors. This yields the following equation of motion for $\tilde{C}(\vec{k}, t)$:

$$\partial_t \tilde{C}(\vec{k}, t) = \left\langle \tilde{\theta}(-\vec{k}, 0) \partial_t \tilde{\theta}(\vec{k}, t) \right\rangle \quad (3.24)$$

$$= \left\langle \tilde{\theta}(-\vec{k}, 0) \left\{ i \int \mathbf{k}_j \tilde{u}_j(\vec{q}) \tilde{\theta}(\vec{k} - \vec{q}) d^d \mathbf{q} - \kappa k_j k_j \tilde{\theta}(\vec{k}) + \tilde{f}_\theta(\vec{k}) \right\} \right\rangle \quad (3.25)$$

where all the terms inside the braces are at time t , whereas the one outside it is at time 0 . As the statistics of both the velocity field and the external force are Gaussian, white-in-time, and independent of each other, the average in Eq.(3.25) can be easily performed (see Appendix (C) and Ref [10, 12]) to obtain:

$$\partial_t \tilde{C}(\vec{k}, t) = -k_j k_m \int \tilde{D}_{jm}(\vec{q}) d^d \mathbf{q} \tilde{C}(\vec{k}, t) \quad (3.26)$$

in the vanishing diffusivity limit of $\kappa \rightarrow 0$. An inverse Fourier transforming yields:

$$\begin{aligned} \partial_t C(\vec{\ell}, t) &= -D^0(L) \frac{\partial^2}{\partial \ell^2} C(\vec{\ell}, t) \\ &\sim -L^\xi \frac{\partial^2}{\partial \ell^2} C(\vec{\ell}, t) \end{aligned} \quad (3.27)$$

We use the boundary condition of, $C(\ell, 0) = 1$ and $C(\ell, t) \rightarrow 0$ as $t \rightarrow \infty$ for all ℓ .

This equation has the following properties:

- The right-hand-side (RHS) of this equation diverges, even for finite ℓ , if we take the limit $L \rightarrow \infty$.
- For a fixed integral scale, L , the dynamic exponent is $z = 2$. This, firstly, is not the dimensional prediction of K41 type phenomenology. Secondly, Eq. (3.27) shows coupling between the largest length scale in the problem, L , and all the other length scales.
- However, if the RHS of Eq. (3.27) evaluated at $\ell = L$ shows that the characteristic decay time for length scale L is, $\mathcal{T}(\ell) \sim \ell^{2-\xi}$.

- The time-dependence in Eq.(3.27) implies that the second order dynamic structure functions for different ℓ will collapse on one another if the time axis is scaled by a factor of ℓ^z . This simple dynamic scaling can be understood by a heuristic argument²: If the Kraichnan model is considered in the Lagrangian framework [1] then it describes the motion of fluid particles being kicked by a force whose statistics is given by Eq.(3.11). Each of these fluid particles just carry the passive-scalar variable with it. As the force is white-in-time the motion of these fluid particles are controlled by Langevin type equation, for which the time correlations typically decay as exponential in time and simple dynamic scaling is obtained.

A similar calculation for the fourth-order time-dependent structure function is straightforward but much more cumbersome. Numerical simulations of the Kraichnan model have been performed successfully to investigate the multiscaling of equal-time structure functions [13]. We could have tried to generalise this numerical method to investigate the dynamic scaling properties of time-dependent structure functions too, but we have chosen instead to investigate the time-dependent structure functions in a model which is computationally far simpler than model A but shows similar equal-time multiscaling properties. We call this model B; it is a shell model analogue of the Kraichnan model [Section(3.3)]. It has often been argued that shell models of turbulence should be viewed as a highly simplified quasi-Lagrangian version of the equations of fluid dynamics. In particular, the dynamic scaling or multiscaling properties of time-dependent structure functions in such shell models is believed to be akin to those of Lagrangian or quasi-Lagrangian velocities [8]. Hence passive-scalar shell models of the Kraichnan type should either (a) agree with the dimensional prediction of $z_p = 2 - \xi$ for all p and show simple dynamic scaling, or (b) it should show dynamic multiscaling.

²U. Frisch, private communication

3.3 Kraichnan type passive-scalar shell model (Model B)

The shell-model for Kraichnan passive-scalar advection was proposed in Ref. [14]. We refer to this as **Model B**. It is defined in a logarithmically discretised wavevector space by the equations

$$\begin{aligned} \left[\frac{d}{dt} + \kappa k_m^2 \right] \theta_m(t) = & i [a_m (\theta_{m+1}^* u_{m-1}^* - \theta_{m-1}^* u_{m+1}^*) \\ & + b_m (\theta_{m-1}^* u_{m-2}^* + \theta_{m-2}^* u_{m-1}^*) \\ & + c_m (\theta_{m+2}^* u_{m+1}^* + \theta_{m+1}^* u_{m+2}^*)] \\ & + \delta_{m,1} f(t). \end{aligned} \quad (3.28)$$

Where the asterisk denotes complex conjugation, θ_m and u_m are, respectively, shell-model analogues of the Fourier component of the the passive scalar and velocity in shell m , $k_m = 2^m k_0$, $k_0 = 1/16$, $a_m = k_m/2$, $b_m = -k_{m-1}/2$, and $c_m = k_{m+1}/2$. $u_{-1} = u_0 = \theta_{-1} = \theta_0 = 0$ is the boundary condition. Note the similarity between this model and the passive-scalar advection-diffusion equation in Fourier space, Eq. (3.23). The convolution term in Eq. (3.23) corresponds to the coupling between different shells in Eq. (3.28). But unlike Eq. (3.23) the coupling in Eq. (3.28) is limited to next nearest neighbours, hence we expect that in the shell model there will be no direct coupling of the small scales to the integral scale as we have seen in Eq. (3.27). The constants defining the shell model, v.i.z, a_m , b_m and c_m are chosen such that in the limit of zero diffusivity and zero external force,

$$E^\theta \equiv \sum_{m=1}^N |\theta_m|^2 \quad (3.29)$$

is conserved, where N is the total number of shells. The Kraichnan version of this passive-scalar shell model the shell velocity is a zero-mean, Gaussian random variable that is white-in-time and with covariance

$$\langle u_m(t) u_p^*(t') \rangle = D_m \delta_{p,m} \delta(t - t'), \quad (3.30)$$

with $D_m = k_m^{-\xi}$. The force is random, Gaussian and white-in-time but limited only to the first shell. For this model, it was shown in Ref. [14] that the equal-time passive-scalar structure functions,

$$S_p^\theta(m) \equiv \langle [\theta_m \theta_m^*]^{p/2} \rangle \sim k_m^{-\zeta_p^\theta} \quad (3.31)$$

exhibit multiscaling for $0 < \xi < 2$, i.e., the equal-time scaling exponents ζ_p^θ is a nonlinear function of p Fig.(3.2). We now define the order- p , time-dependent passive-scalar structure functions for such shell models:

$$F_p(m, t) = \langle [\theta_m(0) \theta_m^*(t)]^{p/2} \rangle, \quad (3.32)$$

where the angular brackets denote an average over the probability distribution functions of the shell velocities and force.

3.3.1 Analytical calculation

We now repeat the calculation done for Mode A. We begin with the equation of motion:

$$\begin{aligned} \frac{d}{dt} F_2(m, t) = & \langle \theta_m(0) [-\kappa k_m^2 \theta_m + \delta_{m,1} f] \\ & - \langle \theta_m(0) \{ i [a_m (\theta_{m+1}^* \mathbf{u}_{m-1}^* - \theta_{m-1}^* \mathbf{u}_{m+1}^*) \\ & + b_m (\theta_{m-1}^* \mathbf{u}_{m-2}^* + \theta_{m-2}^* \mathbf{u}_{m-1}^*) \\ & + c_m (\theta_{m+2}^* \mathbf{u}_{m+1}^* + \theta_{m+1}^* \mathbf{u}_{m+2}^*)] \} \rangle, \end{aligned} \quad (3.33)$$

where all the terms inside the square brackets have time label t . Novikov's theorem [see Appendix (C)] and Eq.(3.30) can be used to perform the average and the resulting equation can be integrated to obtain

$$F_2(m, t) = S_2(m) \exp\left[-\frac{1}{4} k_m^{2-\xi} A(\xi) t\right], \quad (3.34)$$

where

$$A(\xi) = (2^{(2\xi-2)} + 2^{-(2\xi-2)}) + (2^\xi + 2^{-\xi}) + (2^{(\xi-2)} + 2^{-(\xi-2)}) \quad (3.35)$$

Similar relations can be derived for $p = 4$ and higher values of p though the algebraic manipulations required become progressively more complicated. The equivalent relation for Model A, Eq. (3.27) will reduce an equation similar to Eq. (3.34) if the integral in Eq. (3.26) is limited to the region $k - \epsilon$ to $k + \epsilon$ in Fourier space.

The Equation (3.34) and its analogue for $p = 4$ implies that, for this Kraichnan version of the shell model for passive scalar turbulence, there is one a unique characteristic time scale for the all time-dependent structure functions of the passive-scalar,

$$\tau_p \sim k^{-(2-\xi)}, \quad (3.36)$$

at least for $p = 2$ and 4. This results is true irrespective of whether we use integral or derivative time scales of any degree M , i.e., we have *simple dynamic scaling* with $z_{p,M}^D = z_{p,M}^I = 2 - \xi$. [In this example, derivative time scales with $M > 1$ do not exist.]

3.3.2 Numerical Simulations

To confirm the simple dynamic scaling shown by our analytical calculation we have also studied Model B, i.e., Eqs.(3.28) and (3.30) by a direct numerical simulation for $\xi = 0.6$. This is a set of coupled ordinary differential equation (ODE) with random coefficients. Since both the advecting velocity and the force are white-in-time the mathematical meaning of such stochastic differential equation (SDE) is ambiguous. One way of interpreting the solutions, called the Stratanovitch version, is to view the solution of such SDEs to be the limit, as the correlation time goes to zero, of the solution of an ODE with random coefficients which has nonzero correlation time. In our case we first define a shell model for passive scalar advection where the velocity has a finite correlation time τ_c and then take the limit of that $\tau_c \rightarrow 0$. Moreover, all standard numerical method of solving

coupled ODEs assume smooth coefficients and fail when applied to SDE, like Eq. (3.28). The Stratanovitch version of solution is also impractical because, as we go to the limit of small correlation time, we require a time-step δt much smaller than the correlation time. The alternative formulation of SDE, the Ito formulation, is useful for numerical solutions. Without going into further details here [see Appendix (B)] let us state that we use a weak order-one Euler scheme associated with the Ito formulation of Eq. (3.28). In our choice of numerical scheme we have followed Ref. ([14]) where equal-time multiscaling properties of Eq. (3.28) have been investigated. The different parameters used in our simulations, e.g. the total number of shells (N), the large-eddy-turnover-time (τ_L^0), and the time-step (δt) are given in Table. (3.1). In Fig. (3.2) we present ESS plots of the equal-time structure functions, i.e., S_p versus S_2 . These equal-time results agree with previous studies of Ref. [14]. Next we calculate the time-dependent structure functions defined in Eq. (3.32). The imaginary parts of these time-dependent structure functions are negligible compared to their real parts so we plot only the real parts here. These are given in the top panel of Figs. (3.3) and (3.4) for $p = 2$ and 4, respectively.

We next fit an exponential to each of $F_p(m, t)$ up to the time t_μ such that $\frac{F_p(m, t_\mu)}{S_p(m)} = \mu$, and extract a characteristic decay rate $T_p(m)$. We have varied μ from 0.5 to 0.9 without any appreciable change in our final result. Log-log plots of $T_p(m)$ versus m are shown in the bottom plots of Figs. (3.3) and (3.4). The slopes of these and similar plots yield z_2, z_4, z_6 . The error-bars on the equal-time and dynamic exponents are obtained in the following. We carry out 50 runs, each averaged over a time T_{av} given in Table (3.1). We thus obtain 50 different values for each of these exponents. The mean values of these 50 exponents are quoted here [Table (3.2)]; and the root-mean-square deviation about the mean value is the error-limit shown in Table (3.2). Our results are consistent with $z_{p,1}^D = z_{p,M}^I = 2 - \xi$ for all orders p , no matter which degree M we use or whether we use integral or

derivative time scales. We have also used a different kind of time scale here, the alpha-cutoff time, $\tau_p^{\text{cutoff}}(m, \alpha)$, defined via :

$$\frac{F_p[m, \tau_p^{\text{cutoff}}(m)]}{S_p(m)} = \alpha. \quad (3.37)$$

Simple dynamic scaling would imply

$$\tau_p^{\text{cutoff}}(m, \alpha) \sim k_m^{-z_p} \quad (3.38)$$

with $z_p = 2 - \xi$ for all p . In Fig. (3.5) we have plotted, on log-log scale, $\tau_p^{\text{cutoff}}(m, \alpha)$ versus k_m for $\alpha = 1/3$ and $p = 4$. The slope yeilds simple scaling value of z_4 .

To summarise, our analysis of time-dependent structure functions in passive scalar turbulence advected by a Kraichnan-type velocity field, yields following results.

1. Both Model A and Model B show simple dynamic scaling.
2. Model A, in which we consider Eulerian structure functions, yields $z_p = 2$ for all p , if we hold the integral scale fixed.
3. Model B, which can be viewed as a simplified Lagrangian or quasi-Lagrangian model for teh Kraichnan version of the passive-scalar problem, shows simple dynamic scaling, $z_p = 2 - \xi$ which agrees with the dimensional prediction (see page81).
4. Predictions from the multifractal model, which we describe below, also agrees with the dimensional prediction given above since we have simple dynamic scaling here.

There are two important ways in which the statistical properties of a Kraichnan-type-velocity field differs from that of a turbulent velocity field obeying the Navier-Stokes equation. One is the infinitismaly small correlation time, i.e., the white-in-time nature of the Kraichnan velocity; and the other is the Gaussian nature of the

Model	Numerical Scheme	N	κ	δt	τ_L^θ	T_{tr}	T_{av}
Model B	Appendix B	22	2^{-14}	2^{-24}	$\approx 2^{24}\delta t$	$5 \times 10^4 \tau_L$	$10^5 \tau_L$
Model C	Appendix A	22	5×10^{-7}	10^{-4}	$10^5 \delta t$	$5 \times 10^4 \tau_L$	$10^5 \tau_L$

Table 3.1: The total number of shells N , diffusivity κ , the time-step δt , and the box-size eddy turnover time $\tau_L \equiv 1/k_0 u_{rms}$, that we use in our numerical simulations of the two passive-scalar shell models B and C. Data from the first T_{tr} time steps are discarded so that transients can die down. We then average our data for time-dependent structure functions for an averaging time T_{av} . For the simulations of Eq. (3.28) we have use $\xi = 0.6$.

order p	2	4	6
ζ_p^θ	1.40 ± 0.005	1.78 ± 0.01	2.43 ± 0.01
z_p^θ	1.40 ± 0.005	1.40 ± 0.005	1.40 ± 0.01

Table 3.2: The equal-time scaling exponents for even-order structure functions, ζ_p^θ , and the dynamic-scaling exponents of even-order, z_p up to $p = 6$ from our simulation of the Kraichnan shell model, Eq.(3.28). In our simulations we have used $\xi = 0.6$ and from our analytical calculations we expect a value of $z_p = 2 - \xi = 1.4$ for all p .

probability distribution function (PDF) of the Kraichnan velocity. If the first of these properties is relaxed, for example, if we replace the white-in-time nature of the Kraichnan velocity by a non-zero correlation time, our analytical methods, as described above, fail. But we can still use the multifractal model, as in Chapter 2, to study properties of the time-dependent structure functions in passive-scalar. Even if the velocity PDF is not Gaussian the multifractal model can still be used. We show in the next Section that if the PDF of the advecting velocity is Gaussian, simple dynamic scaling is obtained; but if PDF of the advecting velocity is not Gaussian but intermittent, dynamic multiscaling is obtained. Hence our conclusion of simple dynamic scaling for Models A and B should hold even if we consider velocities which are not white-in-time but has non-zero correlation time.

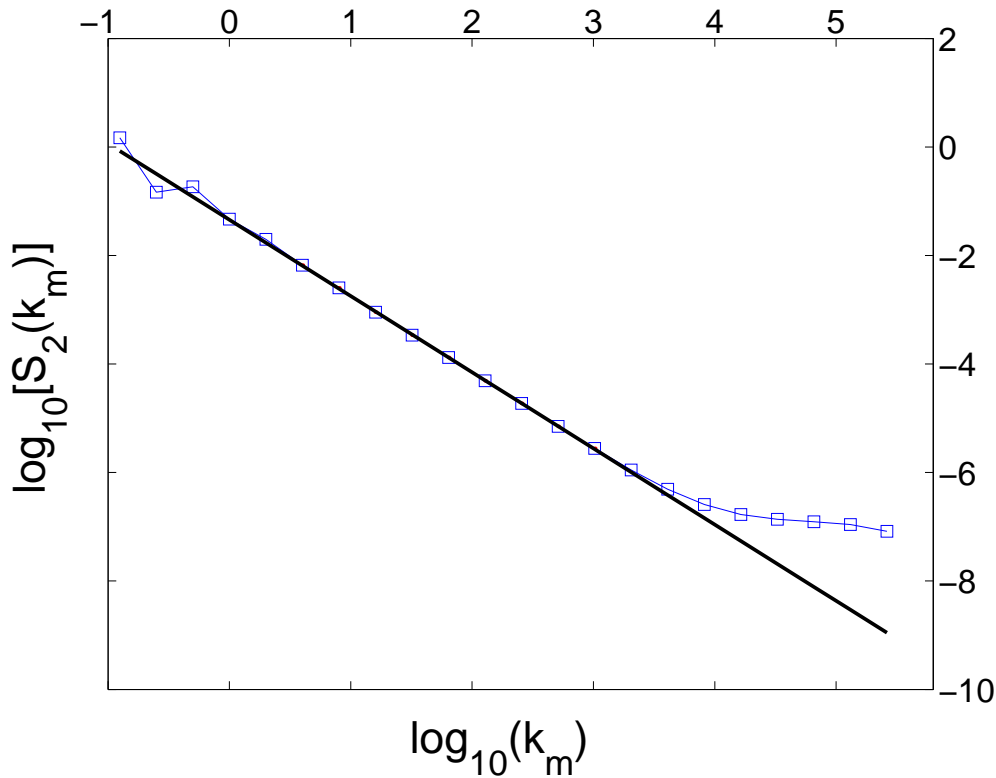


Figure 3.1: A representative log-log plot of $S_2(m)$ versus k_m for the Kraichnan shell model [Eq.(3.28)]. The straight line in the plot is a least-square fit to the inertial range ($m = 5$ to 13). The slope of the straight line is 1.40 ± 0.005

3.4 A passive-scalar shell model advected by turbulent velocity field

3.4.1 Multifractal analysis

Now consider the passive-scalar problem advected by a turbulent velocity, i.e., a velocity field that displays multiscaling of equal-time velocity structure functions and has non-zero correlation time. Of course we can no longer determine the form of the time-dependent structure function analytically. Instead we use the multifractal model discussed in Section (1.7.4) and its extension to dynamic multiscaling which we describe in Section (2.3). The analysis here is more delicate since we have to deal with two multifractal sets, one for the velocity u and another for the passive-scalar field θ .

We begin with the multifractal representation of the equal-time structure function of the passive-scalar field, namely

$$\frac{S_p(\ell)}{\theta_L^p} \equiv \frac{\langle \delta\theta^p(\ell) \rangle}{\theta_L^p} \propto \int_{\mathcal{I}, \mathcal{I}'} d\mu(\mathbf{h}) \left(\frac{\ell}{L} \right)^{\mathcal{Z}(\mathbf{h})}, \quad (3.39)$$

where

$$\mathcal{Z}(\mathbf{h}) = 3 + p\mathbf{h} - D(\mathbf{h}), \quad (3.40)$$

the integration is over a range of universal scaling exponents $\mathbf{h} \in \mathcal{I} \equiv (\mathbf{h}_{\min}, \mathbf{h}_{\max})$.

For each \mathbf{h} in this range, there exists a set $\Sigma_{\mathbf{h}} \subset \mathbb{R}^3$ of fractal dimension $D(\mathbf{h})$ such that,

$$\frac{\delta\theta(\vec{r}, \ell)}{\theta_L} \propto \left(\frac{\ell}{L} \right)^{\mathbf{h}} \quad (3.41)$$

for $\vec{r} \in \Sigma_{\mathbf{h}}$. Here θ_L is the strength of the passive scalar at the forcing scale L . $\delta\theta(\vec{r}, \ell)$ is the fluctuation of the passive scalar variable across a length scale ℓ about the point \vec{r} . The statistics of θ , in particular the multiscaling exponents ζ_p depends on the function $D(\mathbf{h})$, \mathbf{h}_{\min} and \mathbf{h}_{\max} . Since the statistics of θ is determined by the velocity \vec{u} , the functions $D(\mathbf{h})$ is also a depends on the velocity field.

Similar multifractal picture applies to the velocity field too. But the multifractal measure for the velocity field is independent of the passive-scalar field, although the converse is not true. Hence the integration in Eq. (3.39) is over the multifractal measure of both the passive-scalar and the velocity field. For $\vec{r} \in \Sigma'_{\mathbf{h}}$

$$\frac{\delta\mathbf{u}(\vec{r}, \ell)}{u_L} \propto \left(\frac{\ell}{L} \right)^{\mathbf{g}} \quad (3.42)$$

Here the velocity field is assumed to possess scaling exponent $\mathbf{g} \in \mathcal{I}' \equiv (\mathbf{g}_{\min}, \mathbf{g}_{\max})$.

We can use this multifractal representation to study the dynamic structure functions,

$$\frac{\mathcal{F}_p(\ell, \mathbf{t})}{\theta_L^p} \propto \int_{\mathcal{I}, \mathcal{I}'} d\mu(\mathbf{h}, \mathbf{g}) \left(\frac{\ell}{L} \right)^{\mathcal{Z}(\mathbf{h})} \mathcal{G}^{p, \mathbf{h}}\left(\frac{\mathbf{t}}{\tau_{p, \mathbf{h}}}\right), \quad (3.43)$$

where we make the ansatz that $\mathcal{G}^{p,h}(\frac{t}{\tau_{p,h}})$ has a characteristic decay time

$$\tau_{p,h} \sim \frac{\ell}{\delta u(\ell)} \sim \ell^{1-g} \quad (3.44)$$

and $\mathcal{G}^{p,h}(0) = 1$. Note here that on dimensional grounds the simplest form for the characteristic decay time $\tau_{p,h}$ in the one in Eq. (3.44), i.e., it depends solely on the velocity but not on the passive-scalar field. Now let us calculate the degree-2 derivative time scale of order-p,

$$\begin{aligned} T_{p,2}^D &\equiv \left[\frac{1}{S_p(\ell)} \frac{d^2}{dt^2} \mathcal{F}_p(\ell, t) \Big|_{t=0} \right]^{-2} \\ &\propto \left[\frac{1}{S_p(\ell)} \int_{\mathcal{I}} d\mu(h) \left(\frac{\ell}{L} \right)^{z(h)} \left(\frac{d^2}{dt^2} \mathcal{G}^{p,h} \Big|_{t=0} \right) \frac{1}{\tau_{p,h}^2} \right]^{-2}. \end{aligned} \quad (3.45)$$

By using the scaling form of $\tau_{p,h}$ we get

$$T_{p,2}^D \propto \left[\frac{1}{S_p(\ell)} \int_{\mathcal{I}} d\mu(h) \left(\frac{\ell}{L} \right)^{z(h)} \frac{[\delta u(\ell)]^2}{\ell^2} \left(\frac{d^2}{dt^2} \mathcal{G}^{p,h} \Big|_{t=0} \right) \right]^{-2} \quad (3.46)$$

$$\propto \frac{1}{\ell^2 S_p(\ell)} \langle \delta u^2(\ell) \rangle \langle \delta \theta^p(\ell) \rangle \sim \ell^{1-\zeta_2^u/2}. \quad (3.47)$$

The integral in Eq. (3.46) is an average over the velocity field too. As θ is a passive variable here, we assume that the average over the velocity field can be computed independent of averaging over over the θ field. Hence we obtain Eq. (3.47) from Eq. (3.46). Similarly for the degree-M case we get the bridge-relation,

$$z_{p,M}^D = 2 - \frac{\zeta_M^u}{M}, \quad (3.48)$$

which does not depend on p. However, this does not mean we have simple dynamic scaling. The fact that the derivative time scale of order-M depends of ζ_M^u , shows that, firstly for a velocity field which multiscales, i.e., when $\zeta_M^u/M \neq \zeta_1$, we have dynamic multiscaling. Secondly, note that for the Kraichnan velocity field the above formula predicts simple dynamic scaling with $z_{p,1}^D = 2 - \xi$. Higher degree-M derivative exponents do not exists for the Kraichnan shell model. Similar analysis applied to dynamic exponent of the integral type yields

$$z_{p,1}^I = 1 - \zeta_{-1}^u. \quad (3.49)$$

To the best of our knowledge this is the first time points out the physical relevance of equal-time structure function scaling exponents with negative order is noticed. We shall show later that our numerical simulations indicate that the above bridge relation is meaningful only for $M = 1$ for this model, i.e., model C.

3.4.2 Numerical Simulation

Our results using multifractal analysis were confirmed through our numerical simulations in the passive vector shell model (**Model C**)

$$\begin{aligned}
 \left[\frac{d}{dt} + \kappa k_m^2\right]\theta_m(t) = & i[a_m(\theta_{m+1}^* \mathbf{u}_{m-1}^* - \theta_{m-1}^* \mathbf{u}_{m+1}^*) \\
 & + b_m(\theta_{m-1}^* \mathbf{u}_{m-2}^* + \theta_{m-2}^* \mathbf{u}_{m-1}^*) \\
 & + c_m(\theta_{m+2}^* \mathbf{u}_{m+1}^* + \theta_{m+1}^* \mathbf{u}_{m+2}^*)] \\
 & + \delta_{m,1} f(t),
 \end{aligned} \tag{3.50}$$

Here $a_m = k_m$, $b_m = -k_{m-1}/2$ and $c_m = -k_{m+1}/2$ [see Ref. [15]]. And the advecting velocity is supplied from the GOY shell model for fluids, Eq. (3.51).

$$\begin{aligned}
 \left[\frac{d}{dt} + \nu k_m^2\right]\mathbf{u}_n = & i(a_m \mathbf{u}_{m+1} \mathbf{u}_{m+2} + b_m \mathbf{u}_{m-1} \mathbf{u}_{m+1} \\
 & + c_m \mathbf{u}_{m-1} \mathbf{u}_{m-2})^* + f_m^u.
 \end{aligned} \tag{3.51}$$

The shell models, having only next-nearest-neighbour coupling between the shells, are expected to show dynamic properties similar to Lagrangian or quasi-Lagrangian representation. The prediction of the multifractal model are valid in the same representation. Our numerical integration of this two coupled shell model is done by a 2-nd order Adams-Bashforth scheme [see Appendix (A)]. The parameters of simulation for the passive-vector shell model are given in Table (3.1). The relevant parameters of the numerical simulation of the GOY shell model are given in Chapter 2. The equal-time multiscaling properties of this shell-model has been studied in Ref. [15], who calculated the equal-time structure functions,

$$S_p(k_m) = \langle [\theta_m(t) \theta_m^*(t)]^{p/2} \rangle \sim k_m^{-\zeta_p^0} \tag{3.52}$$

and extract the equal-time multiscaling exponents ζ_p^θ . The plot of the structure functions show the 3-cycle characteristic of GOY shell model (see Chapter 2). Hence we have used

$$\Sigma_p(k_n) \equiv \langle |\mathcal{J}(\theta_{n+2}\theta_{n+1}u_n - (1/4)\theta_{n-1}\theta_n\theta_{n+1})|^{p/3} \rangle \sim k_n^{-\zeta_p^\theta}, \quad (3.53)$$

to extract the multiscaling exponents. This method evaluation of equal-time multiscaling exponents is effectively filters out [16] the peculiar 3-cycle. Representative plots of $\Sigma_p(k_m)$ are shown in the top panel of Fig. (3.6), and a plot of ζ_p^θ versus p is shown in the bottom panel. Our equal-time results agrees with the results of Ref. [15].

To find out the dynamic multiscaling exponents of this model, we calculate the dynamic structure function, defined by,

$$f_p(m, t) \equiv \frac{1}{S_p(k_m)} \langle \theta_m(0)\theta_m^*(t) \rangle \quad (3.54)$$

The imaginary part of the function $f_p(m, t)$ is negligible compared to its real part,

$$F_p(m, t) = \Re[f_p(m, t)]. \quad (3.55)$$

We show representative plots of the real part of $F_p(m, t)$ in Fig. (3.7).

3.4.3 Derivative time scales

For extracting the derivative scale $T_{p,2}^D$ we extend $F_p(n, t)$ to negative t via $F_p(n, -t) = F_p(n, t)$ and use a centered, sixth-order, finite-difference scheme to find

$$\frac{\partial^2}{\partial t^2} F_p(n, t)|_{t=0} \quad (3.56)$$

A log-log plot of $T_{p,2}^D(n)$ versus k_n now yields the exponent $z_{p,2}^D$, see Fig. (3.10). In this case we find a clear signature of dynamic multiscaling. Note that the error-limits of the small values of the order- p are large than the one for the higher order- p . This is a characteristic of all our dynamic results. This is due to the

following reason: the time scale of fluctuations for low- p and high- p are very different, hence to get reliable data for all values of p we need many different sampling rates. As the time scale of fluctuations for different shell- m , also are very different it is important to use different sampling rates for different values of m too. In our simulations we have indeed used two different sampling rates, $50 \times \delta t$ for $4 \leq m \leq 8$ and $10 \times \delta t$ for $9 \leq m \leq 13$, respectively. A different choice of sampling rates will give more reliable data for lower values of p , but of course will sacrifice reliability for higher values of p . A comparison of our results with the multifractal prediction

$$z_{p,M}^D = 2 - \frac{\zeta_M^u}{M}, \quad (3.57)$$

is shown in Fig. (3.10) and Table (3.3). The M dependence of this result is a clear signature of dynamic multiscaling

3.4.4 Integral time scale

The evaluation of the integral time scale $T_{p,M}^I$ is numerically far more complicated than evaluation of the derivative time scale, because we need reliable data for $F_p(m, t)$ for large values of t . We now concentrate on the integral time scale with $M = 1$,

$$T_{p,1}^I(n, t_u) \equiv \int_0^{t_u} F_p(n, t) dt, \quad (3.58)$$

and the associated dynamic-multiscaling exponents defined via

$$T_{p,1}^I(n, t_u) \sim k_n^{-z_{p,1}^I}. \quad (3.59)$$

In principle we should use $t_u \rightarrow \infty$ but, since it is not possible to obtain $F_p(n, t)$ accurately for large t , we select an upper cut-off t_u such that $F_p(m, t_u) = \alpha$, where, for all m and p , we choose $\alpha = 0.7$ in the results we report. We have checked that our results do not change if we use $0.3 < \alpha < 0.8$. The slope of a log-log plot of $T_{p,1}^I(m)$ versus k_n now yields $z_{p,1}^I$ (Fig. 3.10 and Table 3.3).

order(p)	ζ_p	$z_{p,1}^I$ [Eq. (3.60)]	$z_{p,1}^I$	$z_{p,2}^D$ [Eq. (3.57)]	$z_{p,2}^D$
1	0.34 ± 0.001	0.56 ± 0.005	0.52 ± 0.03	0.645 ± 0.0001	0.63 ± 0.03
2	0.63 ± 0.001	0.56 ± 0.005	0.53 ± 0.03	0.645 ± 0.0001	0.64 ± 0.03
3	0.87 ± 0.001	0.56 ± 0.005	0.56 ± 0.005	0.645 ± 0.0001	0.64 ± 0.005
4	1.07 ± 0.001	0.56 ± 0.005	0.56 ± 0.005	0.645 ± 0.0001	0.64 ± 0.01
5	1.24 ± 0.004	0.56 ± 0.005	0.56 ± 0.005	0.645 ± 0.0001	0.64 ± 0.01
6	1.38 ± 0.006	0.56 ± 0.005	0.57 ± 0.007	0.645 ± 0.0001	0.64 ± 0.02

Table 3.3: Order- p (Column 1) multiscaling exponents for $1 \leq p \leq 6$ from our simulations of the passive-scalar model advected by a velocity field obeying GOY shell mode: equal-time exponents ζ_p^θ (Column 2), integral-scale dynamic-multiscaling exponent $z_{p,1}^I(\theta)$ of degree-1 (Column 3) from the bridge relation and the values of $\zeta_{-1}^u = 0.44 \pm 0.005$, $z_{p,1}^I$ from our calculation using time-dependent structure functions (Column 4), the derivative-time exponents $z_{p,2}^D$ (Column 6) from the bridge relation and the values of $\zeta_p^u = 0.709 \pm 0.0001$, $z_{p,2}^D$ from our calculation using time-dependent structure function (Column 7). The error estimates are obtained as described in the text.

Let us also point out an additional difficulty involving the integral time scale for the present case. The bridge-relation for the integral time scale dynamic multiscaling exponents is

$$z_{p,1}^I = 1 - \zeta_{-1}^u, \quad (3.60)$$

which involves equal-time multiscaling exponents of negative order. Whether or not ζ_p^u for negative- p will exist, depends on the probability distribution of $|\mathbf{u}_m|$. We have calculated the cumulative probability distribution function, $P^{\text{cum}}[|\mathbf{u}_m|]$, of $|\mathbf{u}_m|$ in rank-order method (see Chapter 5). A representative plot is shown in Fig (3.9). For small values of the argument x the function $P^{\text{cum}}(x)$ goes to zero as $\approx x^{1.84}$. This implies that structure functions of order $p \leq -1.84$ will not exist. This also implies that the integral time-scale $T_{p,M}^I$ for $M > 1.84$ will not exist. In our simulation we have concentrated on the value of $M = 1$. A representative plot of $S_{-1}(k_m)$ is shown in the bottom panel of Fig. (3.9). The exponent ζ_{-1}^u is extracted by least-square fit to the inertial range of this plot.

3.5 Passive vector models

Now let us try to extend our results from the domain of passive-scalar turbulence to passive-vector turbulence. Here there are additional difficulties. The passive-vector advection-diffusion equation (**model D**) is :

$$\partial_t B_i + u_j \partial_j B_i = B_j \partial_j u_i + \kappa \partial_{jj} B_i + f_i^B \quad (3.61)$$

Here the vector field \vec{B} is the passive-vector. The velocity \vec{u} follows the Navier-Stokes equation, and \vec{f}^B is the external forcing. Note that in the passive-scalar model, Eq. (3.9), the quantity

$$E^\theta = \int \theta^2(\vec{x}) d^d x \quad (3.62)$$

is conserved in the limit of $\kappa \rightarrow 0$ and $f^\theta = 0$. But in the passive-vector case the corresponding quantity:

$$E^B = \int B_i(\vec{x}) B_i(\vec{x}) d^d x \quad (3.63)$$

is not conserved. Hence there is possibility of unbounded growth of of the passive-vector field. This phenomenon is called the *dynamo effect*. If indeed the passive-vector equation shows dynamo effect then there will be no possibility of statistical steady state, and hence our idea of multiscaling will loose sense.

First we consider the Kraichnan version of this passive vector model. The velocity then do not obey the Navier-Stokes equation but is random, Gaussian and white-in-time with the statistics given in Eq. (3.10). The equal-time multiscaling properties of this model was studied in Ref. [17], in which the following was proved:

1. No dynamo effect occurs if $\xi < 1$ in three spatial dimension (Anti-dynamo theorem).
2. For the range of $0 < \xi < 1$, equal-time multiscaling is observed, and even ζ_2^b has intermittency corrections.

Here we study the dynamic correlation function,

$$C_{ij}(\vec{x} - \vec{y}, t) \equiv \langle B_i(\vec{x}, 0) B_j(\vec{y}, t) \rangle \quad (3.64)$$

We can of course investigate dynamic multiscaling properties only if $\xi < 1$, i.e., when the *anti-dynamo* theorem holds. Proceeding in a way exactly similar to the passive scalar problem, we calculate :

$$\partial_t C_{ij}(\vec{x} - \vec{y}, t) = \langle B_i(\vec{x}, 0) \partial_t B_j(\vec{y}, t) \rangle \quad (3.65)$$

Going over to Fourier space and calculating in a fashion very similar to the passive-scalar problem, we have

$$\partial_t \tilde{C}_{ij}(\vec{k}, t) = \epsilon_{ijk} \epsilon_{klm} \epsilon_{\mu\nu\delta} \epsilon_{\delta\beta\alpha} k_j k_\nu D_{l\mu}^0(L) C_{m\alpha}(\vec{k}, t) \quad (3.66)$$

This gives the same dynamic exponent $z = 2$, if we consider a fixed integral scale L , as in the case of the passive-scalar.

In the next step we look at a passive-vector shell model. We arrive at this model in the following way. A shell model for magnetohydrodynamic turbulence was proposed in Ref. [18], inspired by the GOY shell model, which showed equal-time multiscaling. We take this shell model and make it passive³. We obtain the following passive-vector shell model (**model E**):

$$\begin{aligned} \left[\frac{d}{dt} + \kappa k_m^2 \right] \theta_m(t) = & i [a_m (\theta_{m+2} \mathbf{u}_{m+1} - \theta_{m+1} \mathbf{u}_{m+2}) \\ & + b_m (\theta_{m+1} \mathbf{u}_{m-1} + \theta_{m-1} \mathbf{u}_{m+1}) \\ & + c_m (\theta_{m-2} \mathbf{u}_{m-1} + \theta_{m-1} \mathbf{u}_{m-2})]^* \\ & + \delta_{m,1} f(t), \end{aligned} \quad (3.67)$$

where the advecting velocity obeys the GOY shell model, and $a_m = k_m/6$, $b_m = -k_{m-1}/3$ and $c_m = -k_{m-2}/(3/2)$.

³The passive-vector advection-diffusion equation has been obtained in exactly similar way by the making the equation of MHD passive.

Consider the two advection-diffusion type of models we have discussed in this Chapter (namely model A and model D). For each of them we can define even order correlation functions in Fourier space

$$\tilde{C}_{2p}(\vec{k}, t) \equiv \left\langle \left[\phi(\vec{k}, t) \phi(-\vec{k}, t) \right]^p \right\rangle \quad (3.68)$$

Here ϕ is the passive scalar θ in model A and a component of the passive-vector B_i in model D. By Gaussian averaging we can show that the equation of motion of this correlation function is of the form,

$$\partial_t C_{2p}(\vec{k}, t) = A_{2p} C_{2p}(\vec{k}, t) + B_{2p} C_{2p-2} \quad (3.69)$$

Here A_{2p} depends on the velocity-velocity correlator D^0 and component of the Fourier mode \vec{k} and B_{2p} depends on the correlation function of the force. This type of equations are called *moment equations*. This moment equation is *closed*. By which we mean that RHS of Eq. (3.69) contains correlation functions of order equal to or less than the order on the LHS. This *closed* nature of the moment equations is due to the white-in-time nature of the advecting velocity. The moment equation is also diagonal. By which we mean that the LHS and the RHS of Eq. (3.69) contains the same wave-vector \vec{k} . For advection-diffusion type of equations we have considered the moment equation is always *diagonal* due to the nature of the coupling term. Unfortunately the moment equation for model E is closed but not diagonal. The same is true for moment equations of model C. But the moment equations for model B are both closed and diagonal. This explains the subtle difference between the coupling term of model B and model C. For example the order-2 moment equation for model E will be of the form

$$\partial \langle \theta_m^*(0) \theta_m^*(t) \rangle = \sum A_{p,q} \langle \theta_p^*(0) \theta_q^*(t) \rangle + \text{forcing terms}. \quad (3.70)$$

Here the shell index $p, q = m+2, m+1, \dots, m-2$, A_p are numerical constants. we need to change Eq. (3.67) appropriately to make the moment equations diagonal.

Fortunately, another shell model for MHD equations, introduced in Ref. [19], when turned into passive-Kraichnan type, yields closed moment equation. Before we embark into a study of multiscaling properties of this model, we need to investigate whether or not this model shows a dynamo effect. This passive vector shell model is (**model F**)

$$\begin{aligned} \left[\frac{d}{dt} + \kappa k_m^2\right] B_m(t) = & i[a_m(B_{m+2}u_{m+1}^* - B_{m+1}^*u_{m+2}) \\ & + b_m(B_{m+1}u_{m-1}^* - B_{m-1}^*u_{m+1}) \\ & + c_m(B_{m-2}u_{m-1} - B_{m-1}u_{m-2})] \\ & + \delta_{m,1}f(t), \end{aligned} \quad (3.71)$$

where $a_m = \alpha k_{m+1}$, $b_m = \beta k_m$ and $c_m = \gamma k_{m-1}$; $\alpha = 1/6$, $\beta = 1/3$, and $\gamma = 2/3$. Here the velocity is random, taken from a Kraichnan ensemble. To investigate the possibility of a dynamo effect we write the equation of motion for the quantity:

$$P_m(t) = \langle B_m^*(t)B_m(t) \rangle \quad (3.72)$$

The equation of motion is :

$$\begin{aligned} \frac{1}{2} \frac{d}{dt} P_m = & c^2 k_{m-1}^2 D_{m-1} P_{m-2} + \{b^2 k_m^2 D_{m+1} + c^2 k_{m-1}^2 D_{m-2}\} P_{m-1} \\ & + \{abk_{m+1}^2 D_{m+2} + (abk_m^2 - ack_{m+1}^2) D_{m+1} \\ & + (bck_m^2 - ack_{m-1}^2) D_{m-1} + bck_{m-1}^2 D_{m-2}\} P_m \\ & + \{a^2 k_{m+1}^2 D_{m+2} + b^2 k_m^2 D_{m-1}\} P_{m+1} + a^2 k_{m+1}^2 D_{m+1} P_{m+2} \end{aligned} \quad (3.73)$$

The dynamo effect is characterised by the behaviour of

$$\begin{aligned} \frac{d}{dt} E^b(t) = & \sum_n P_m(t) \\ = & \sum P_m(t) \left[\frac{1}{6} k_{m+1}^2 D_{m+2} + \frac{2}{3} k_m^2 D_{m-1} \right. \\ & + \frac{1}{12} k_m^2 D_{m+1} + \frac{1}{3} k_{m-1}^2 D_{m-2} \\ & \left. + \frac{1}{3} k_{m+1}^2 D_{m+1} + \frac{2}{9} k_{m-1}^2 D_{m-1} \right] \\ = & A(\xi) \sum_m k_m^{2-\xi} P_m(t) \end{aligned} \quad (3.74)$$

where

$$A(\xi) = k_0 \left[\frac{1}{6} 2^{2-2\xi} + \frac{2}{3} 2^{-\xi} \frac{1}{12} 2^\xi + \frac{1}{3} 2^{-2-2\xi} + \frac{1}{3} 2^{2+\xi} + \frac{2}{9} 2^{-2-2\xi} \right] \quad (3.75)$$

is a positive constant irrespective of the values of ξ ⁴. This implies that this passive-scalar shell model will always develop into a dynamo irrespective of the value of ξ . This result is an example, where a crucial qualitative feature of the advection-diffusion equation, i.e. the *anti-dynamo theorem* does not hold in the shell model analogue⁵. Moreover, this result implies that this Kraichnan-passive-vector shell model will not attain non-equilibrium statistical steady state, where its scaling properties can be studied.

Finally we consider the passive-vector shell model, Eq. (3.67) advected by velocity obeying GOY shell model equations. In this case we can no longer analytically investigate the existence of dynamo, but our numerical investigations suggest the presence of dynamo. Similar results in support of dynamo in MHD shell models have also been obtained by other groups [19]⁶; however the nonlinearities in such MHD shell model make the dynamo saturate and a statistical steady state is obtained eventually.

3.6 Conclusion

In this Chapter we have discussed dynamic multiscaling in models of passive turbulence, v.i.z. several different models of passive scalar and vector. If the velocity field taken from a Kraichnan ensemble then our analytical calculation of the full advection-diffusion equations (for both the passive-scalar and the passive-vector) show simple dynamic scaling. Simple dynamic scaling also follows from

⁴Let us remind our reader that the shells in shell models are logarithmically spaced, i.e. $k_m = k_0 \lambda^m$, and we have used $\lambda = 2$ and $k_0 = 1/16$

⁵These yet unpublished results on dynamo-effect in shell model were obtained jointly with T. Gilbert

⁶Private communications, A. Basu, unpublished.

our analytical calculations and numerical simulations of a shell model. If the velocity field is assumed to be Gaussian but white-in-time, simple dynamical scaling is obtained. But if in addition the velocity field is multifractal, then our numerical simulations of a passive vector shell model shows dynamic multiscaling, with exponents which agrees well with *bridge-relations* obtained using multifractal model. The *bridge-relation* for the dynamic exponent of the integral variety involves equal-time scaling exponents with negative order. This is perhaps the first instant where the mathematically curious, negative-order equal-time structure functions have found physical connection. And finally we show that a passive-vector shell model advected by a Kraichnan velocity field will not reach a non-equilibrium statistical steady state. Similar results for a passive vector shell model advected by the GOY shell model are indicated by numerical experiments.

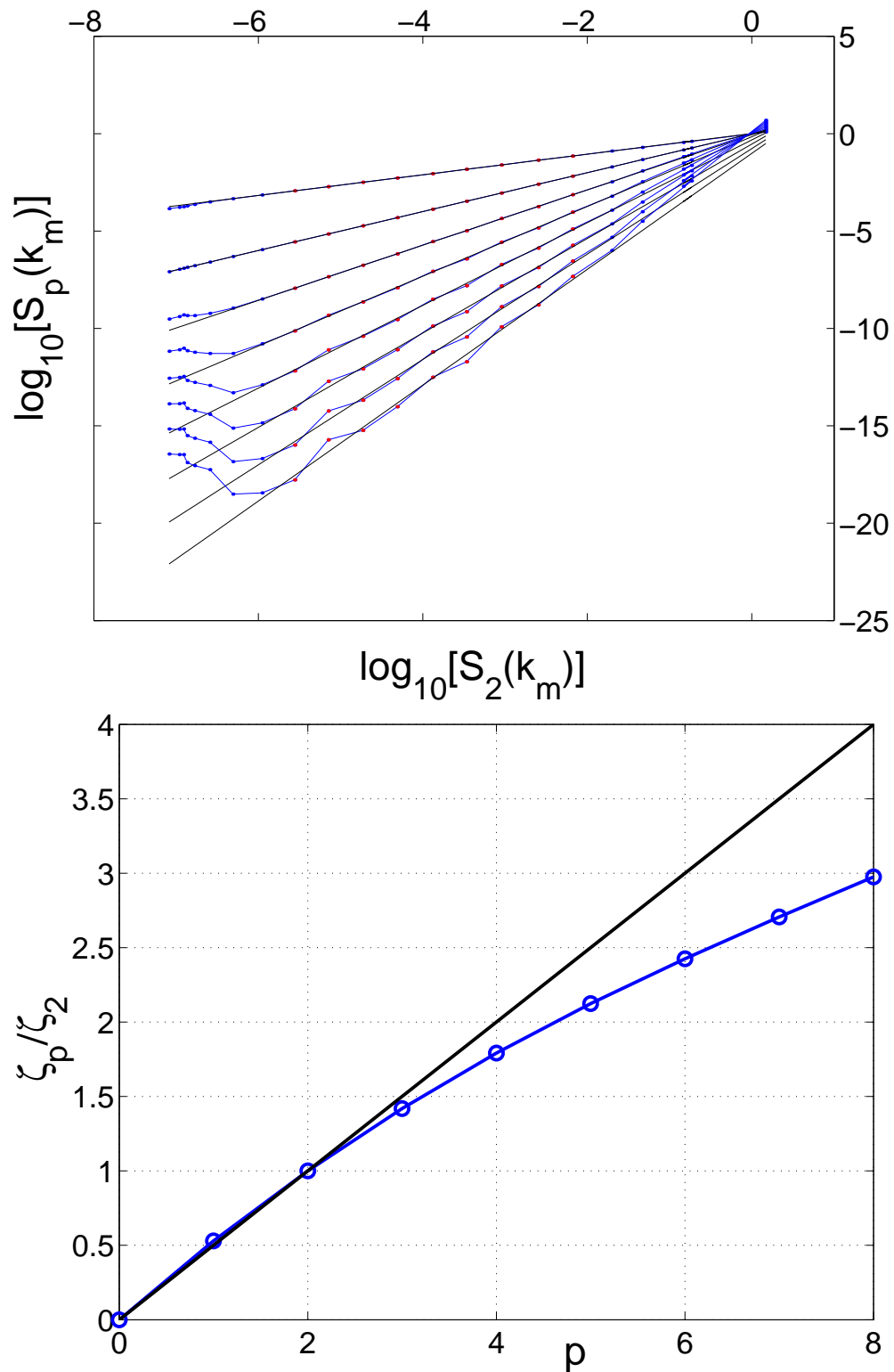


Figure 3.2: A representative, ESS, log-log plot (top panel) of equal-time structure functions, $S_p(m)$, for $p = 1$ to 8 , for the Kraichnan shell model [Eq.(3.28)] versus $S_2(m)$. The straight lines shown in the plot are least square fits to the inertial range. (Bottom panel) The ratio of the scaling exponents ζ_p/ζ_2 extracted from ESS plots is plotted against the order p . Equal-time multiscaling is evident from the curvature of this plot. The straight line in this plot is the simple scaling prediction $\zeta_p = (p/2)\zeta_2$. We have use $\xi = 0.6$. $\zeta_2 = 1.4 \pm 0.005$ is obtained from our numerical simulations.

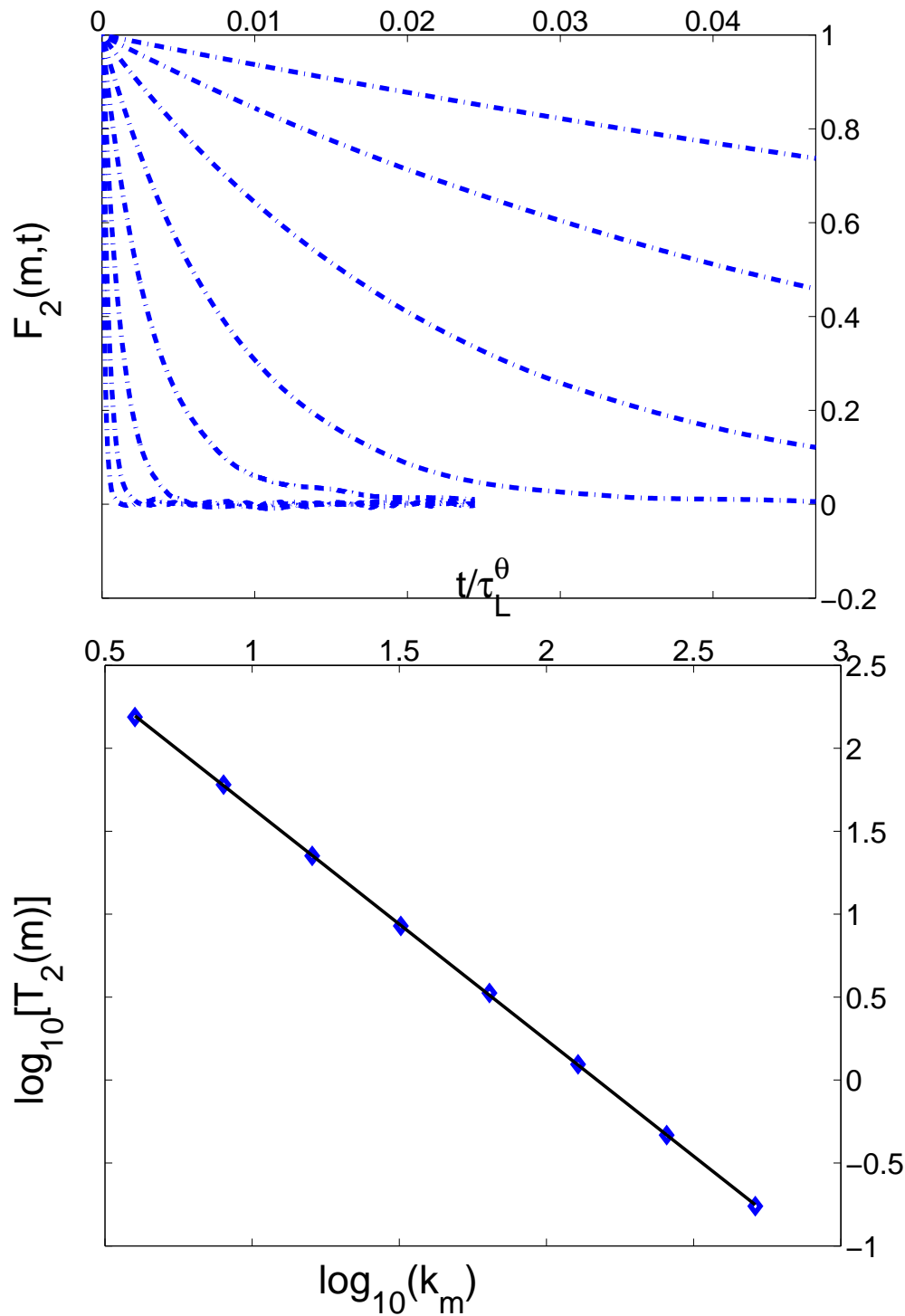


Figure 3.3: (Top panel) Plot of the order-2 time-dependent structure function for the Kraichnan version of passive-scalar shell model, Eqs.(3.28) and (3.30), with $\xi = 0.6$. Exponential functions [like Eq. (3.34)] are good approximation to these time-dependent structure functions. The uppermost curve is for $m = 6$, the next for $m = 7$, and so on till $m = 13$ (the last few are not clearly visible on this scale). (Bottom panel) The characteristic time scale $T_2(m)$, extracted from such exponential fits, plotted against the wavevector k_m on a log-log scale. The straight line is the least-squares fit to the points shown in the plot. The slope of this straight line gives $z_2 \simeq 1.40 \simeq 2 - \xi$, with $\xi = 0.6$.

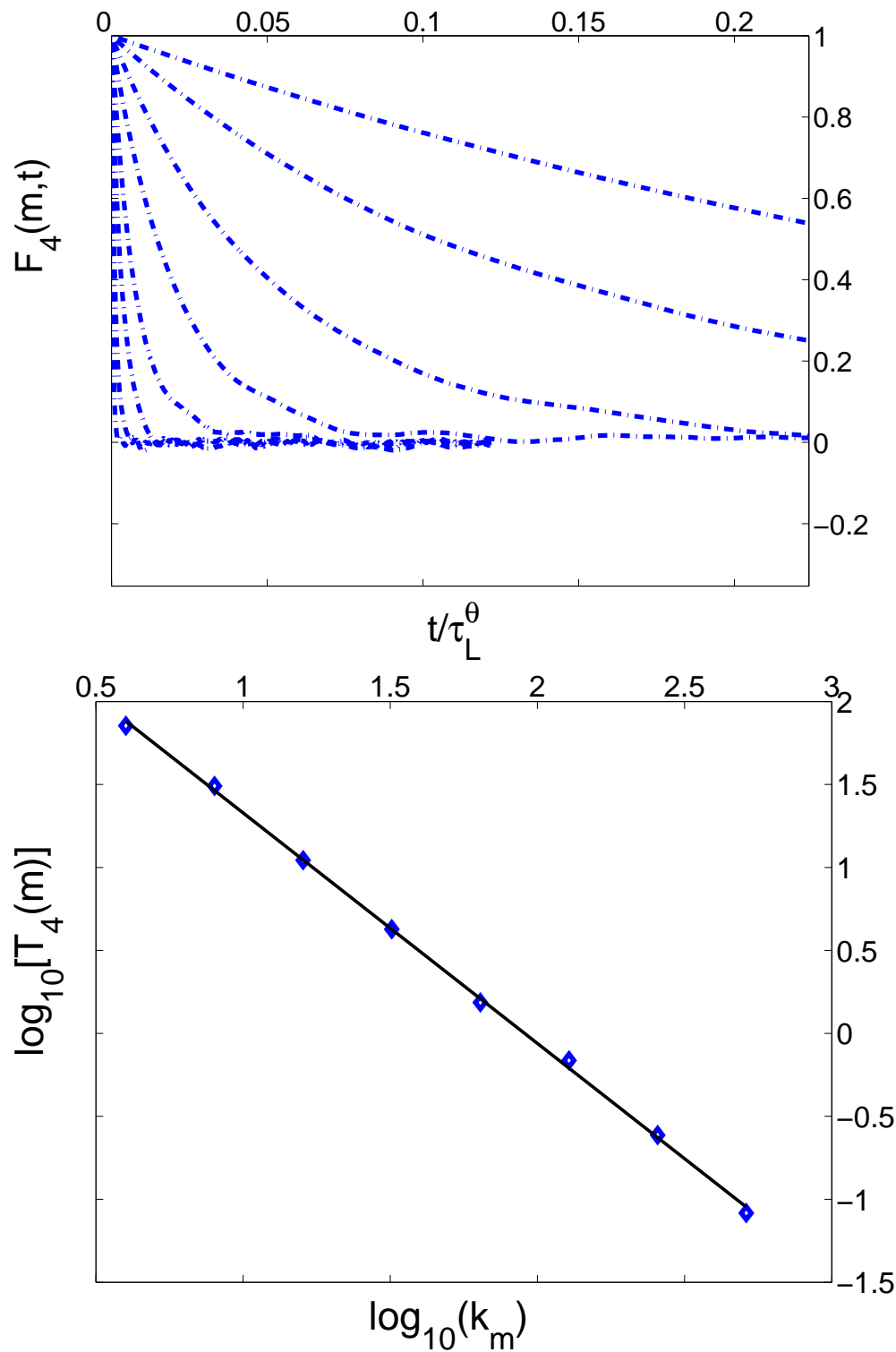


Figure 3.4: (Top panel) Plot of the order-4 time-dependent structure function for the Kraichnan version of passive-scalar shell model, Eqs.(3.28) and (3.30), with $\xi = 0.6$. Exponential functions [like Eq. (3.34)] are good approximation to these time-dependent structure functions. The uppermost curve is for $m = 6$, the next for $m = 7$, and so on till $m = 13$ (the last few are not clearly visible on this scale). (Bottom panel) The characteristic time scale T_m , extracted from such exponential fits, plotted against the wavevector k_m on a log-log scale. The straight line is the least-squares fit to the points shown in the plot. The slope of this straight line gives $z_4 \simeq 1.39 \simeq 2 - \xi$, with $\xi = 0.6$.

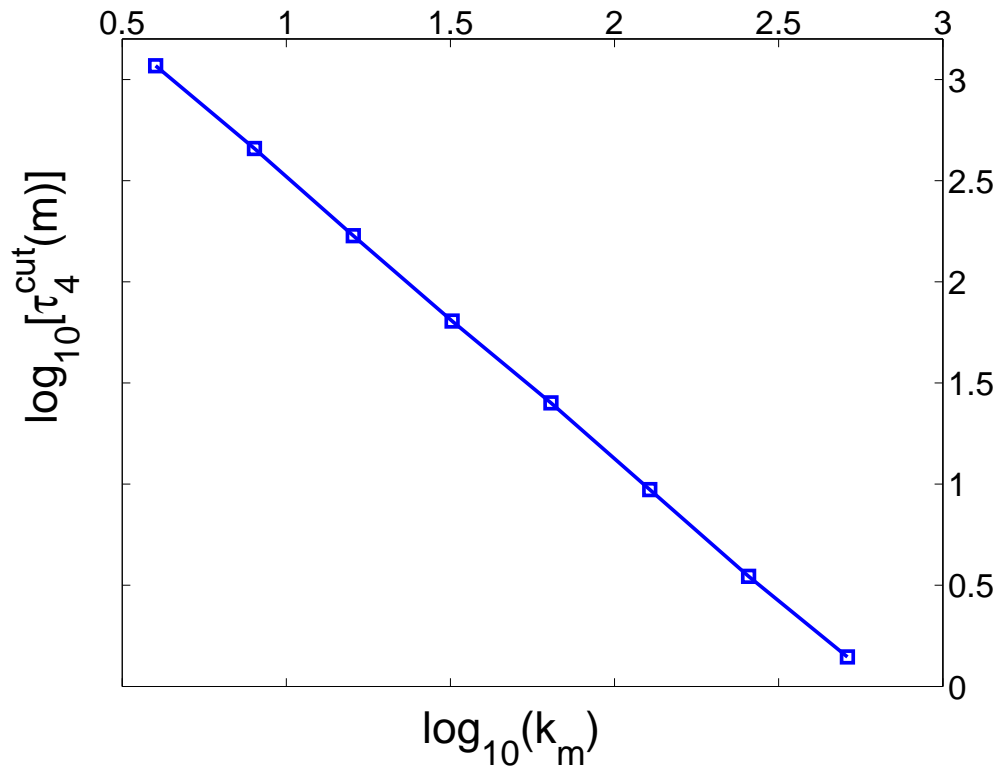


Figure 3.5: Log-log plot of the time, $\tau_4^{cut}(m)$, the time taken for the real part of $F_4(m, t)$ to become 1/3-rd of $F_4(m, 0)$, versus k_m . The slope of this plot gives the dynamic scaling exponent $z = 1.40$, which is consistent with the prediction $2 - \xi$ for the case $\xi = 0.6$ which we study here.

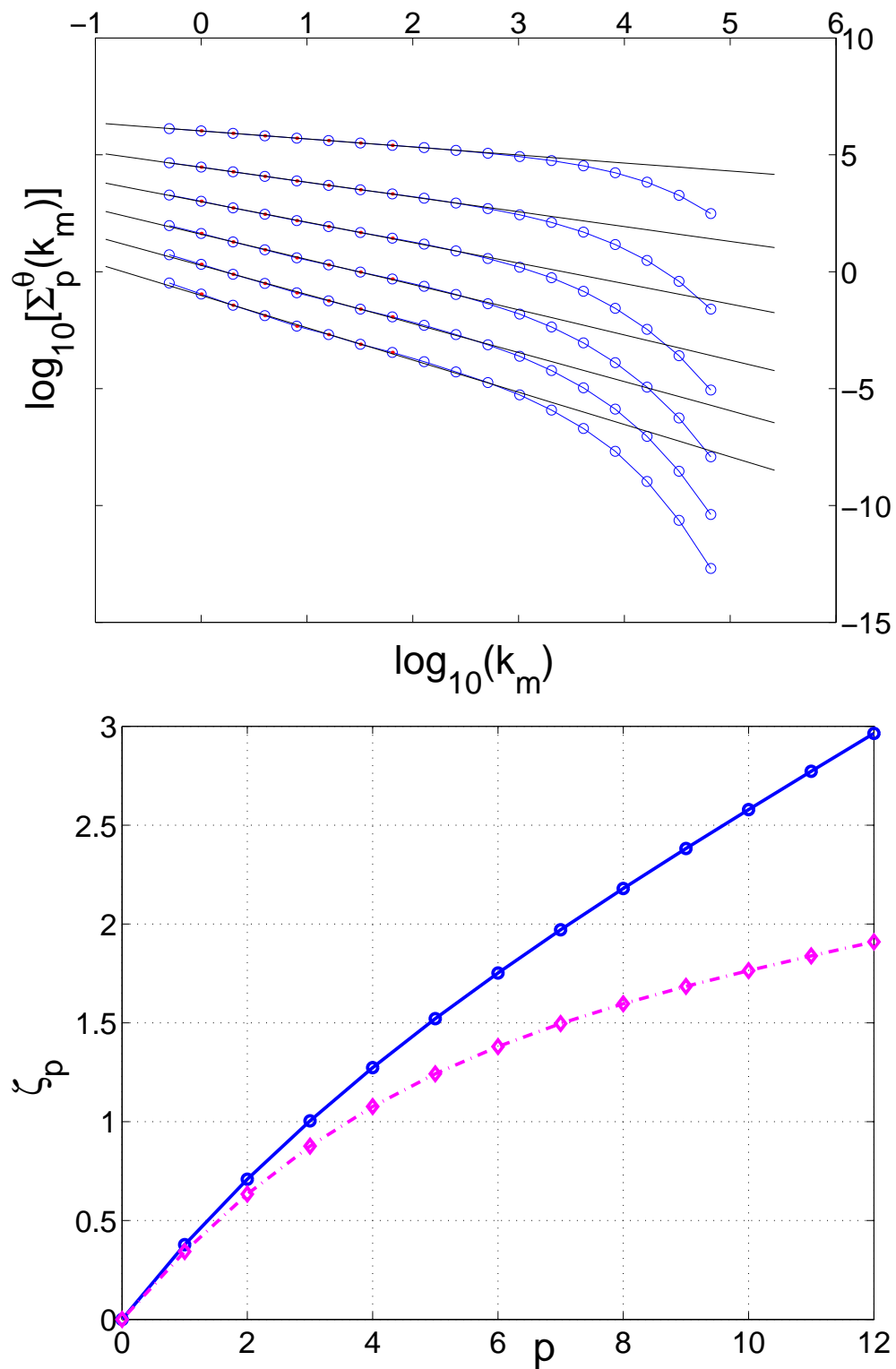


Figure 3.6: (top panel) A representative plot of equal-time structure functions $\Sigma_p^\theta(k_m)$ for $p = 1$ (top) to 6 (bottom) of the passive-scalar shell model [Eq. (3.50)] advected by the GOY shell model. (bottom panel) And a plot of the equal-time multiscaling exponents ζ_p^θ (broken line) extracted from power-law fits to the scaling range in the equal-time structure functions. Equal-time multiscaling is evident from this plot. The full line shows the ζ_p^u for the GOY shell model for comparison

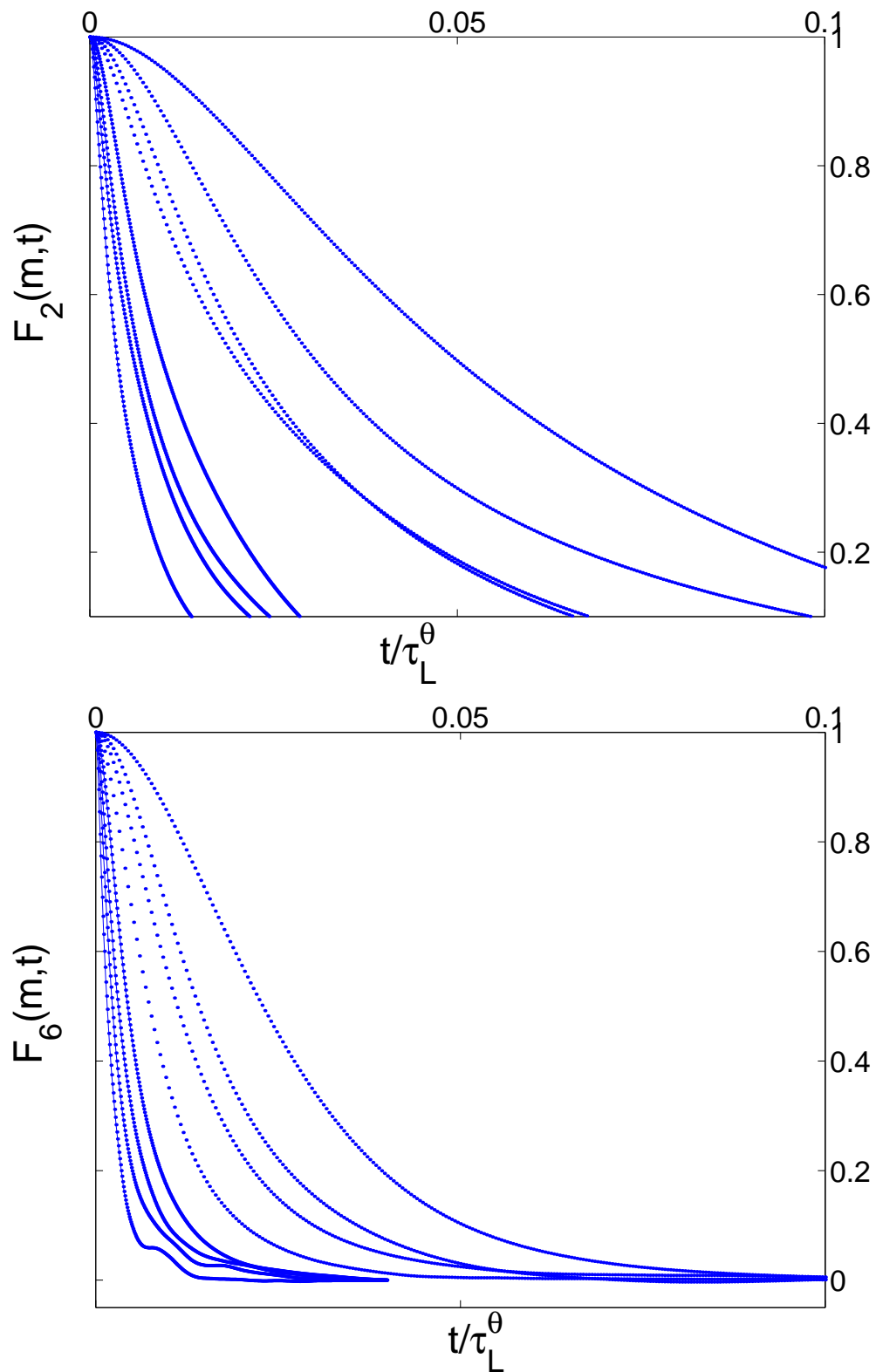


Figure 3.7: A representative plots of dynamic structure functions of 2-nd (top) and 6-th order (bottom) for the passive scalar field θ_n obeying Eq. (3.50), being advected by velocity field obeying the GOY shell model [Eq. (3.51)]

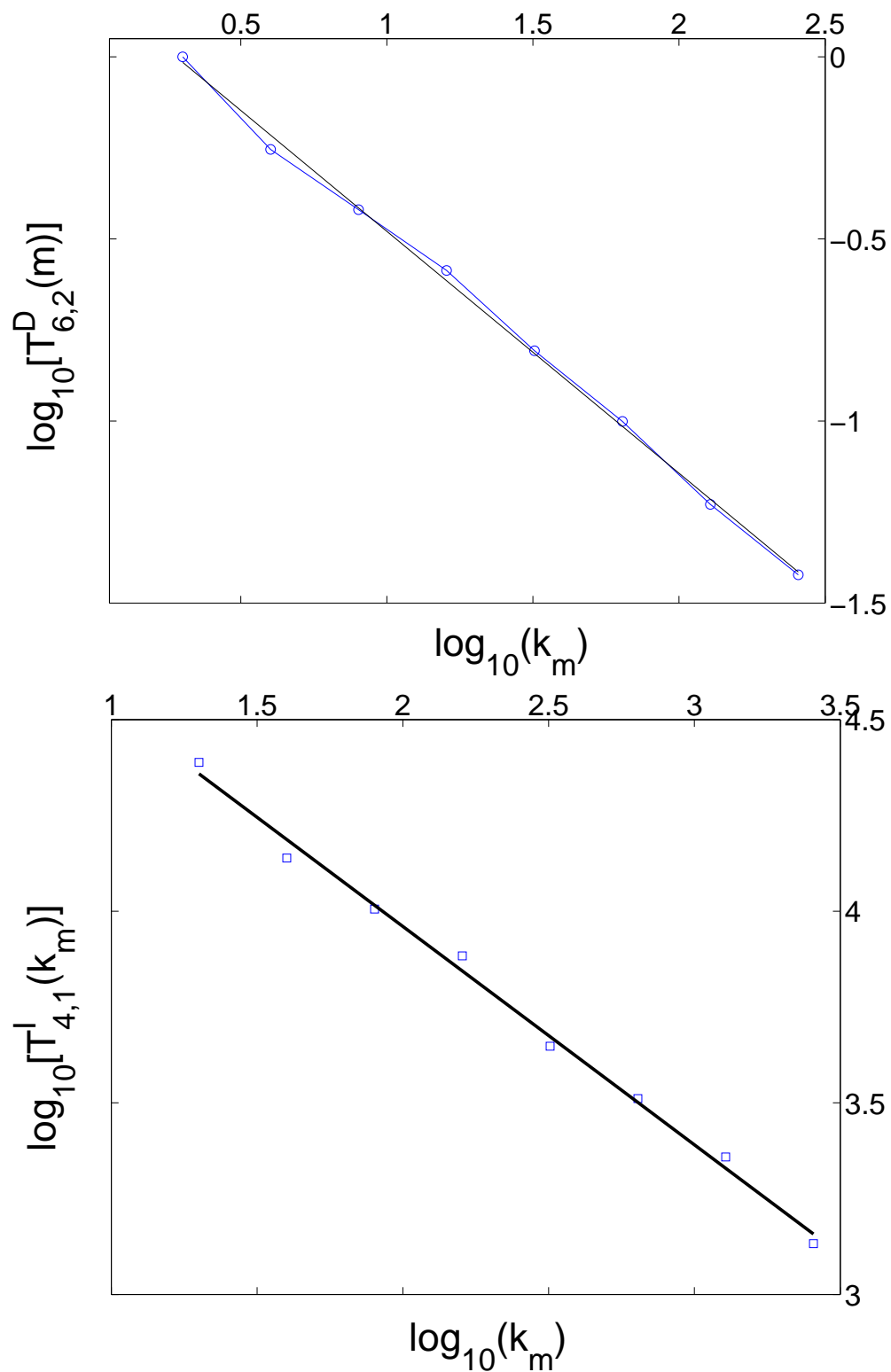


Figure 3.8: (top) Representative plot of the derivative time scales $T_{6,2}^D(n)$ versus k_m (in log-log scale); the slopes of the linear least-square fits yield the dynamic exponents $z_{6,2}^D$. (bottom) Representative plot of the integral time scales $T_{4,1}^I(m)$ versus k_m (in log-log scale); the slopes of the linear least-square fits yield the dynamic exponents $z_{4,1}^I$.

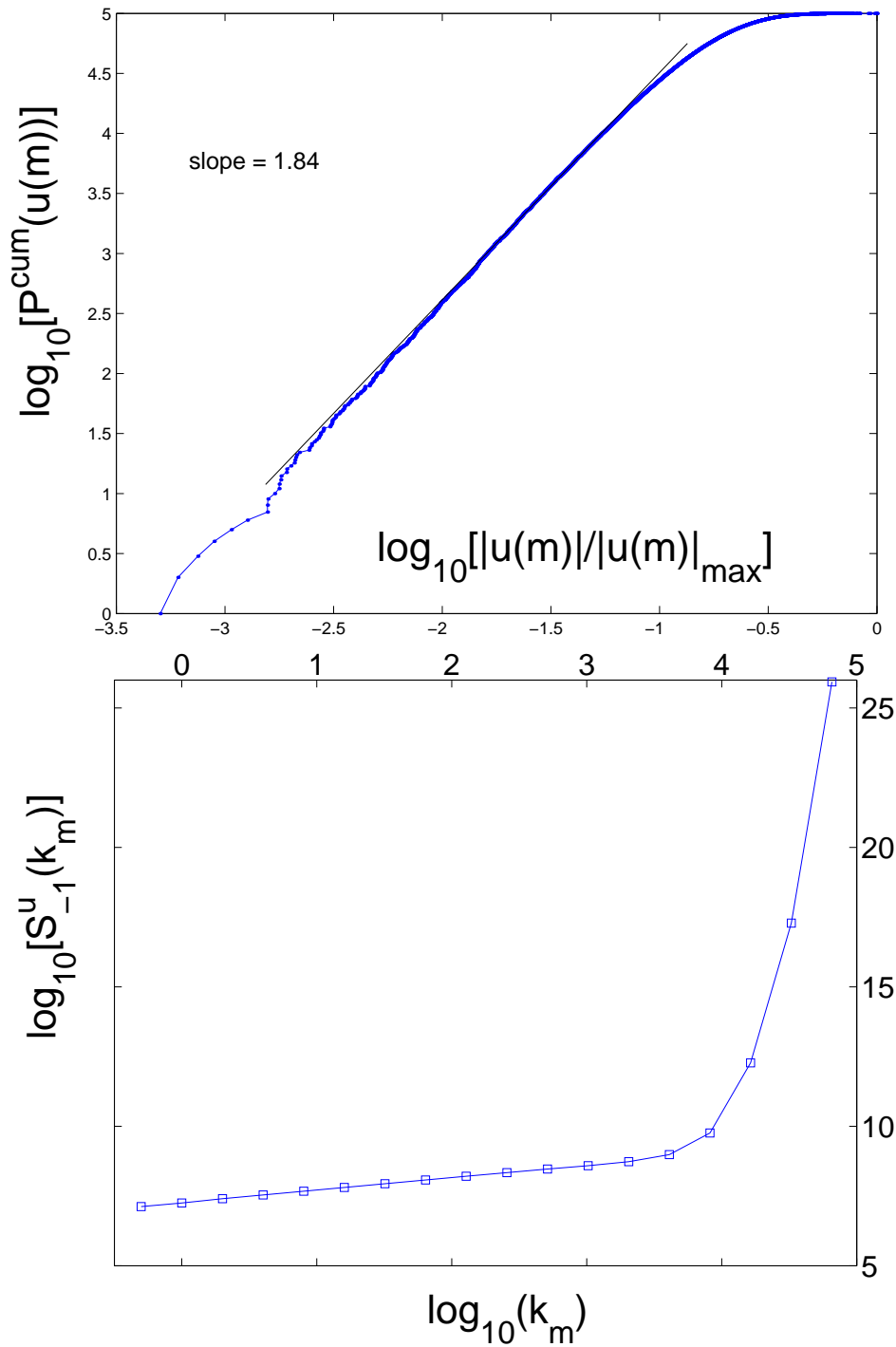


Figure 3.9: Top panel: A representative plot of the cumulative probability distribution function $P^{\text{cum}}(|u_m|)$ versus $|u_m|$ on a log-log scale for $m = 8$. The straight line suggests the power-law behaviour $P^{\text{cum}}(|u_m|) \sim |u_m|^{1.84}$ for small $|u_m|$. The power 1.84 is fairly insensitive to the value of m for shells in the inertial range. This power-law behaviour implies that the equal-time multiscaling exponent ζ_{-1}^u can be defined. We obtain it from a log-log plot of $S_{-1}^u(k_m)$ versus k_m (bottom panel).

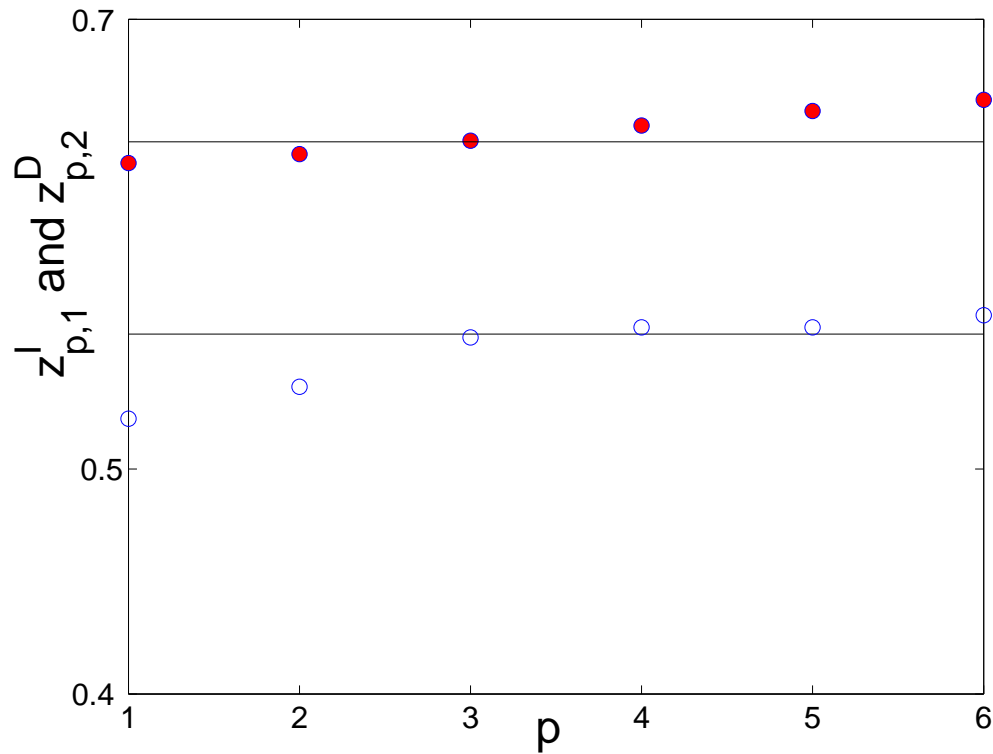


Figure 3.10: Plot of $z_{p,2}^D$ (open circles) and $z_{p,1}^I$ (filled circles) versus p from our simulations of passive-scalar shell model advected by GOY shell model. Our numerical estimates for these exponents (see Table 3.3 for error-bars) are consistent with our predictions which are indicated by the horizontal lines. Even though the dynamic exponents are independent of p , their dependence on the degree M and the difference between the derivative and interal-scale exponents are clear signatures of dynamic multiscaling.

Bibliography

- [1] G. Falkovich, K. Gawędzki, and M. Vergassola, *Rev. Mod. Phys.* **73**, 913 (2001).
- [2] R. Kraichnan, *Phys. Fluids* **11**, 945 (1968).
- [3] R. Kraichnan, *Phys. Rev. Lett.* **72**, 1016 (1994).
- [4] R. Kraichnan, *Phys. Rev. Lett.* **78**, 4922 (1997).
- [5] V. L'vov, E. Podivilov, and I. Procaccia, *Phys. Rev. E* **55**, 7030 (1997).
- [6] F. Hayot and C. Jayaprakash, *Phys. Rev. E* **57**, R4867 (1998).
- [7] D. Mitra and R. Pandit, *Physica A* **318**, 179 (2003).
- [8] D. Mitra and R. Pandit, *Phys. Rev. Lett* **93**, 024501 (2004).
- [9] A. Kolmogorov, *Dokl. Acad. Nauk USSR* **30**, 9 (1941).
- [10] U. Frisch, *Turbulence the legacy of A.N. Kolmogorov* (Cambridge University Press, Cambridge, 1996).
- [11] Y. Kaneda, T. Ishihara, and K. Gotoh, *Phys. Fluids*. **11**, 2154 (1999).
- [12] J. Zinn-Justin, *Quantum Field Theory and Critical Phenomenon* (Oxford University Press, Oxford, 1999).
- [13] U. Frisch, A. Mazzino, and M. Vergassola, *Phys. Rev. Lett.* **80**, 5532 (1998).

- [14] A. Wirth and L. Biferale, *Phys. Rev. E* **54**, 4928 (1996).
- [15] M. Jensen, G. Paladin, and A. Vulpiani, *Phys. Rev. A* **45**, 7214 (1992).
- [16] L. Kadanoff, D. Lohse, J. Wang, and R. Benzi, *Phys. Fluids* **7**, 617 (1999).
- [17] M. Vergassola, *Phys. Rev. E* **53**, R3021 (1996).
- [18] A. Basu, A. Sain, S. Dhar, and R. Pandit, *Phys. Rev. Lett* **81**, 2687 (1998).
- [19] P. Giuliani, in *Nonlinear MHD waves and Turbulence*, edited by T. Passot and P. Sulem (Springer, New York, 1999), Vol. 356, Lecture Notes in Physics.

Chapter 4

Dynamic multiscaling in the Navier–Stokes Equation

In this Chapter we investigate numerically the dynamic multiscaling of velocity structure function for the Navier–Stokes equation. We have already discussed the general belief in this field: If we use Eulerian-velocity, time-dependent structure functions to study the dynamic multiscaling properties, we expect simple dynamic scaling with

$$z_p^{\mathcal{E}} = 1, \quad (4.1)$$

where $z_p^{\mathcal{E}}$ is the order- p dynamic scaling exponent and the superscript \mathcal{E} stands for Eulerian. By contrast, if we use Lagrangian or quasi-Lagrangian velocities, we can expect nontrivial *dynamic multiscaling*. The associated multiscaling exponents should then be related by *bridge relations* to the equal-time multiscaling exponents ζ_p [1]. As we have discussed in the previous Chapters these *bridge relations* depend on the way a characteristic time scales are extracted from the time-dependent structure functions. From standard Direct Numerical Simulation (DNS) of Navier–Stokes equation Eulerian velocity time-dependent structure functions can be numerically calculated. Lagrangian velocities have also been calculated from particle-tracking DNS [2, 3]. But dynamic multiscaling properties have not been investigated. We have developed an algorithm to perform pseudo-spectral DNS of quasi-Lagrangian velocities. In this Chapter we report

our preliminary results from pseudo-spectral DNS with 512^3 and 256^3 Fourier modes. To the best of our knowledge, this is the first DNS that calculates quasi-Lagrangian velocity structure functions.

The rest of this Chapter is organised in the following way. First, in Sec. (4.1), we summarise the results of earlier studies in this field. In Sec. (4.2) we discuss the pseudo-spectral DNS algorithm and our additions to it which makes it possible to calculate quasi-Lagrangian velocities. Next we present our results from DNS studies with 512^3 and 256^3 Fourier modes in Sec. (4.3). Our results for time-dependent quasi-Lagrangian velocity structure functions are preliminary. And we conclude with a discussion of our results and directions for future research.

4.1 Review of earlier studies

In experiments on turbulent flows, the fluid velocity is measured at one point in space as a function of time. Temporal separations are then converted to spatial separations by using the mean velocity of the flow. This is justified by invoking the *Taylor frozen-flow hypothesis*, which implies the simple dynamic scaling embodied in Eq. (4.1) [see page 11 and Sec. (1.10.3)]. This phenomenon is also called the *sweeping effect* (see page 32).

At present there is no theory which starts from the Navier–Stokes equation and systematically proves Eq. (4.1) for Eulerian velocities. Neither is there any theory which systematically removes the sweeping effect and unearths the dynamic multiscaling for the velocity structure functions. In what follows we summarise a few earlier attempts.

Jayaprakash and Hayot [4, 5] addressed the problem of time-dependent behaviour of structure functions in the forced Burgers equation

$$\partial_t u + u \partial_x u = \nu \partial_{xx} u + f(x, t) \quad (4.2)$$

We illustrate their idea in the one dimensional case with the Burgers velocity

$u = -\partial_x \psi$, where ψ is the velocity potential¹. $f(x, t)$ is the external stochastic force. In Ref. [4] these authors showed that

$$\frac{\partial}{\partial t} F_2(r, t) = \frac{1}{2} \frac{\partial}{\partial r} T_3(r, t) + \langle u_1 f_2 \rangle - \langle u_2 f_1 \rangle \quad (4.3)$$

where $u_1 \equiv u(x + r, t/2)$ and $u_2 \equiv u(x - r, -t/2)$,

$$F_p(r, t) \equiv \langle [u_1 - u_2]^p \rangle, \quad (4.4)$$

and

$$T_3(r, t) \equiv -\langle (u_1 + u_2)(u_1 - u_2)^2 \rangle. \quad (4.5)$$

These authors further argued, based on very plausible assumptions that, in the zero-viscosity limit, $\nu \rightarrow 0$ the leading behaviour of T_3 is

$$\frac{\partial}{\partial t} T_3(r, t) \propto \langle u^2 \rangle \frac{\partial F_2}{\partial r} + A \frac{\partial^2 F_4}{\partial r^2}; \quad (4.6)$$

the second term in Eq. (4.6) is subdominant to the first. $u = \frac{u_1 + u_2}{2}$. If we take only the dominant contribution, we have

$$\frac{\partial^2}{\partial t^2} F_2(r, t) \propto \langle u^2 \rangle \frac{\partial^2}{\partial r^2} F_2(r, t) \quad (4.7)$$

which implies, (see Ref. [1] and Chapter 2), :

$$z_{2,2}^D = 1. \quad (4.8)$$

This is the dominant contribution to dynamic-scaling exponent. Furthermore, if the subleading term in Eq. (4.6) is considered, in our notation,

$$z_{2,2}^D = 1 + \frac{\zeta_2 - \zeta_4}{2}. \quad (4.9)$$

Thus dynamic multiscaling can be uncovered by looking at the subdominant terms. Note that, this *bridge relation* Eq. (4.9) is a particular case of a more general bridge relation which we obtained in Ref. [1] and Chapter 2, Eq. (2.22), by

¹The Burgers equation is in many ways akin to the Navier–Stokes equation (see page 35).

using the multifractal model. Thus, the authors of Ref. [4] not only outlined how $z = 1$ can emerge as the leading dynamical behaviour time-dependent Eulerian velocity structure function in the Burgers equation but also suggested how non-trivial dynamic multiscaling can emerge from the subdominant contributions. Unfortunately a similar analysis for the Navier–Stokes equation, also performed in Ref. [4], is more complicated because of the presence of the pressure terms. And finally the arguments presented above are not rigorous even for the Burgers equation.

A different approach for the removal of sweeping effects was originally suggested by Belinicher and L’vov [6] and later developed further by L’vov, Procaccia and Podivilov [7, 8, 9, 10]. In Ref. [6] the authors proposed a quasi-Lagrangian transformation that converts Eulerian velocity fields to quasi-Lagrangian ones. We follow them and begin by defining the Lagrangian velocity. Let $\vec{\rho}(t|\vec{r}_0, t_0)$ be the Lagrangian displacement of a fluid particle which was at \vec{r}_0 at time t_0 . Then the Lagrangian velocity of this fluid particle is

$$\vec{U}(t|\vec{r}_0, t) \equiv \frac{\partial}{\partial t} \vec{\rho}(t|\vec{r}_0, t_0). \quad (4.10)$$

The quasi-Lagrangian velocity field, defined with respect to the above mentioned Lagrangian particle, is

$$\vec{V}(\vec{x}, t|\vec{r}_0, t_0) \equiv \vec{u}[\vec{x} + \vec{\rho}(t|\vec{r}_0, t_0), t], \quad (4.11)$$

where $\vec{u}(\vec{x}, t)$ is the Eulerian velocity field, which satisfies the incompressible Navier–Stokes equation

$$\partial_t \vec{u}(\vec{x}, t) + \left[\vec{u}(\vec{x}, t) \cdot \vec{\nabla} \right] \vec{u}(\vec{x}, t) = \nu \nabla^2 \vec{u}(\vec{x}, t) + \vec{\nabla} p + f, \quad (4.12)$$

with incompressibility imposed by

$$\vec{\nabla} \cdot \vec{u} = 0. \quad (4.13)$$

Equation (4.12) and (4.12) can be rewritten as

$$\partial_t \vec{u}(\vec{x}, t) + P \left[\vec{u}(\vec{x}, t) \cdot \vec{\nabla} \right] \vec{u}(\vec{x}, t) = \nu \nabla^2 \vec{u}(\vec{x}, t) + f, \quad (4.14)$$

where the external force f is now divergenceless. Here P is the transverse projection operator. The application of P to any vector field \vec{a} is non-local in physical space and has the form

$$[P\vec{a}(\vec{x})]_i \equiv \int d^d y P_{ij}(\vec{x} - \vec{y}) a_j(\vec{y}) \quad (4.15)$$

where P_{ij} is the inverse Fourier transform of

$$\tilde{P}_{ij}(\vec{q}) \equiv \delta_{ij} - \frac{q_i q_j}{q^2}, \quad (4.16)$$

where \vec{q} is a wave-vector. The quasi-Lagrangian transformation can be performed on any field, not only the velocity field [11]. Furthermore, Ref. [7] showed that the following quasi-Lagrangian velocity difference

$$\vec{W}(\vec{x}, t | \vec{r}_0, t_0) \equiv \vec{V}(\vec{x}, t | \vec{r}_0, t_0) - \vec{V}(\vec{r}_0, t | \vec{r}_0, t_0) \quad (4.17)$$

satisfies the following Navier–Stokes-like equation:

$$\partial_t \vec{W}(\vec{x}, t | \vec{r}_0, t_0) + P \left[\vec{W}(\vec{x}, t | \vec{r}_0, t_0) \cdot \vec{\nabla} \right] \vec{W}(\vec{x}, t | \vec{r}_0, t_0) = \nu \nabla^2 \vec{W}(\vec{x}, t | \vec{r}_0, t_0) + F \quad (4.18)$$

Here F is the quasi-Lagrangian transformed f . Equal-time structure functions for quasi-Lagrangian velocity differences, can now be defined as

$$\mathcal{S}_p^{ql}(\ell) = \left\langle \left[\vec{W}(\vec{r}_0 + \vec{\ell}, t | \vec{r}_0, t_0) \cdot \left(\frac{\vec{\ell}}{\ell} \right) \right]^p \right\rangle. \quad (4.19)$$

If the turbulent flow is homogeneous and stationary, these structure functions should not depend on the choice of \vec{r}_0 and t_0 . Hence the quasi-Lagrangian velocity equal-time structure functions should be equal to the Eulerian-velocity equal-time structure functions. In numerical simulations this equality will emerge only after sufficiently long averaging, since this is required to obtain statistically homogeneous results from a DNS study. We explore this below.

The quasi-Lagrangian velocity is expected to be free of the *sweeping effect* and we might expect that quasi-Lagrangian velocity structure functions to show non-trivial dynamic multiscaling [10]. Let us define the quasi-Lagrangian velocity time-dependent structure functions

$$\mathcal{F}_p^{ql}(\ell, \{t_1, \dots, t_p\}) = \left\langle W_{\parallel}(\vec{r}_0 + \vec{\ell}, t_1) \dots W_{\parallel}(\vec{r}_0 + \vec{\ell}, t_p) \right\rangle. \quad (4.20)$$

For $t_1 = t_2 = \dots = t_p$ this reduces to Eq. (4.19). In general, we shall restrict ourselves to the case, $t_1 = 0$ and $t_2 = t_3 = \dots = t_p = t$. Then, following the formalism detailed in Chapter 2, we can extract the following length-dependent time scales:

1. The integral time scale of order- p and degree- M

$$\mathcal{T}_{p,M}^I(\ell) \equiv \left[\frac{1}{\mathcal{S}_p^{ql}(\ell)} \int_0^\infty \mathcal{F}_p^{ql}(\ell, t) t^{(M-1)} dt \right]^{(1/M)}. \quad (4.21)$$

and the associated integral dynamic scaling exponent via

$$\mathcal{T}_{p,M}^I \sim \ell^{z_{p,M}^I}. \quad (4.22)$$

2. The derivative time scale of order- p and degree- M

$$\mathcal{T}_{p,M}^D \equiv \left[\frac{1}{\mathcal{S}_p^{ql}(\ell)} \frac{\partial^M}{\partial t^M} \mathcal{F}_p^{ql}(\ell, t) \Big|_{t=0} \right]^{(-1/M)} \quad (4.23)$$

and the associated *derivative* dynamic-multiscaling exponent via

$$\mathcal{T}_{p,M}^D \sim \ell^{z_{p,M}^D}. \quad (4.24)$$

For these quasi-Lagrangian velocity dynamic multiscaling exponents the multifractal model predicts the two following bridge relations [1, 10].

$$z_{p,M}^I = 1 + [\zeta_{p-M} - \zeta_p]/M, \quad (4.25)$$

$$z_{p,M}^D = 1 + [\zeta_p - \zeta_{p+M}]/M. \quad (4.26)$$

The ultimate goal of our study is to verify these and similar bridge relations through quasi-Lagrangian DNS.

Experimental studies of dynamic structure functions of Eulerian and Lagrangian velocities were performed in Refs. [12, 13]. Recent DNS studies of second order time-dependent structure functions for Eulerian and Lagrangian velocities have been reported in Refs. [14]. The results of these studies have been summarised in Chapter 1 Sec. 1.10.3.

4.2 Quasi-Lagrangian algorithm

We now perform a pseudo-spectral DNS of the Navier–Stokes equation to calculate the quasi-Lagrangian velocity field. Note that, as far as numerical simulations are concerned, quasi-Lagrangian velocity is defined on a grid in physical space. Two possible strategies can be used for this numerical simulation. (1) We can solve Eq. (4.17) by using a pseudo-spectral method. (2) We can solve the Navier–Stokes equation in a pseudo-spectral way and at every time step perform a quasi-Lagrangian transformation on the Eulerian velocity. We use method (2).

In standard pseudo-spectral DNS of the Navier–Stokes equation, in a periodic box, the spatial derivatives are calculated in Fourier space and the products are calculated in physical space. We use a cube of length $L = 2\pi$ with N^3 grid points. In our simulations we have used $N = 512$ or 256 . Other parameters of our simulation are given in Table 4.1. The algorithm for a standard pseudo-spectral DNS of Eulerian velocity is summarised below :

1. We start with an initial velocity in Fourier space, say $\vec{u}(\vec{q})^2$, where \vec{q} is the wave-vector. The initial velocity is taken to be divergenceless.
2. Given $\vec{u}(\vec{q})$ we can easily evaluate the dissipative term $[-\nu q^2 \vec{u}(\vec{q})]$ since it is

²We follow the convention that a wavevector argument like \vec{q} indicates that we are considering the spatial Fourier transform of the function under consideration

local in Fourier space.

3. We next evaluate $\vec{\Omega}(\vec{q}) \equiv i\vec{q} \times \vec{u}(\vec{q})$ which is also local in Fourier space.

4. The nonlinear term in the Navier–Stokes equation can be written as

$$\mathcal{N}[\vec{u}(\vec{x})] \equiv \vec{u} \cdot \vec{\nabla} \vec{u} = -\vec{u} \times \vec{\nabla} \times \vec{u} = -\vec{u}(\vec{x}) \times \vec{\Omega}(\vec{x}) \quad (4.27)$$

Hence inverse Fourier transform $\vec{\Omega}(\vec{q})$ to physical space, $\vec{\Omega}(\vec{x})$.

5. Inverse Fourier transform $\vec{u}(\vec{q})$ to physical space $\vec{u}(\vec{x})$ and $\vec{\Omega}(\vec{q})$ to $\vec{\Omega}(\vec{x})$.

6. Evaluate the cross product in last term in Eq. (4.27) in real space.

7. Next we Fourier transform the nonlinear term to obtain $\mathcal{N}[\vec{u}(\vec{q})]$. And multiply it by the projection operator [Eq. (4.16)] to impose incompressibility.

At this stage the Navier–Stokes equation in Fourier space as follows:

$$\partial_t \vec{u}(\vec{q}) = -\mathcal{P}\mathcal{N}[\vec{u}(\vec{q})] - \nu q^2 \vec{u}(\vec{q}) + \vec{f}(\vec{q}). \quad (4.28)$$

Where the first two terms on the right-hand-side (RHS) of this equation have been evaluated. The forcing terms in not considered at this stage, and Eq. (4.28) is updated in time by time-step δt by the Adams-Bashforth scheme [see Appendix A].

8. Since we want to force the fluid at large spatial scales, we impose the forcing as follows: All the Fourier-modes of $\vec{u}(\vec{q})$ for $|\vec{q}| = 1, 2$ are rescaled such that the total energy in these two shells of Fourier space are held at a constant.

To extend this algorithm so to obtain quasi-Lagrangian velocities, we note that:

$$\vec{V}(\vec{q}, t) = \vec{u}(\vec{q}, t) \exp[i\vec{q} \cdot \vec{\rho}(t|\vec{r}_0, t_0)] \quad (4.29)$$

where $\rho(t|\vec{r}_0, t_0)$ is the Lagrangian displacement of the fluid particle which was at \vec{r}_0 at time t_0 . Hence all we need to know is the Lagrangian displacement of a

single reference particle. We start with the reference particle situated at a grid point \vec{r}_0 in physical space. At any point of time t , if the reference particle is at the point \vec{r} , (which may be an off-grid point), the equation of motion of this particle is

$$\partial_t \rho(t|\vec{r}_0, t_0) = \vec{U}(t|\vec{r}_0, t_0) = \vec{u}(\vec{r}, t). \quad (4.30)$$

This equation can be integrated by a second-order Adams-Bashforth scheme. In addition, the point \vec{r} can be written as $\vec{r} = \vec{r}_0 + \vec{\rho}$. Hence

$$\vec{u}(\vec{r}, t) = \frac{1}{N^3} \sum e^{i\vec{q}\cdot\vec{r}} \vec{u}(\vec{q}) \quad (4.31)$$

$$= \frac{1}{N^3} \sum e^{i\vec{q}\cdot\vec{r}_0} \vec{V}(\vec{q}) \quad (4.32)$$

$$= \vec{V}(\vec{r}_0, t) \quad (4.33)$$

Where in the last step Eq. (4.29) has been used. Thus we need an additional computational cost of one Fourier transform, per time step, to perform pseudo-spectral quasi-Lagrangian DNS.

Clearly the Fourier transform lie at the heart of any pseudo-spectral code. It is crucial therefore, to use an efficient Fast Fourier Transform (FFT) routine. We have carried out these calculations on three different types of computers: (a) The IBM Regatta. (b) The SGI Altix. and (c) 33-node Linux Beowulf-type cluster. In each of these we have use the FFT routines from (a) PESSL, (b) parallel SCSL, and (c) parallel FFTW libraries respectively.

4.3 Results

We perform pseudo-spectral de-aliased DNS with quasi-Lagrangian velocities with N^3 grid points. Parameters of our simulation are given in Table 4.1.

We first calculate the shell-averaged energy spectrum, $E(k)$ defined by,

$$E(k) \equiv \left\langle \sum_{|\vec{q}|=k} u_i(\vec{q}) u_i^*(\vec{q}) \right\rangle. \quad (4.34)$$

Run	N	ν	δt	λ	u_{rms}	Re_λ	L_{int}	τ_L	T_{tr}	T_{av}
NS1	512	7×10^{-4}	1×10^{-4}	0.47	0.74	504	1.75	$5 \times 10^4 \delta t$	$2\tau_L$	$3\tau_L$
NS2	256	1×10^{-3}	2×10^{-4}	0.99	0.35	302	1.85	$6 \times 10^4 \delta t$	$2\tau_L$	$5\tau_L$

Table 4.1: Viscosity ν , the time-step δt , Taylor microscale $\lambda \equiv \sqrt{\frac{5E}{\omega}}$, $E \equiv \int E(k)dk$, $\omega \equiv \int k^2 E(k)dk$, the root-mean-square velocity $u_{rms} \equiv \sqrt{2E/3}$, the Taylor-microscale Reynolds number $Re_\lambda \equiv \lambda u_{rms}/\nu$, the integral scale $L_{int} \equiv (\sum_n |u_n|^2 / k_n^2) / (\sum_n |u_n|^2 / k_n)$, and the box-size eddy turnover time $\tau_L \equiv L_{int}/u_{rms}$, that we use in our numerical simulation of the Navier–Stokes equation. The run NS1 was run in a IBM Regatta machine and the run NS2 was run in an ALTIX machine. Data from the first T_{tr} time steps are discarded so that transients can die down. We then average our data for time-dependent structure functions for an averaging time T_{av} .

As the quasi-Lagrangian velocity and the Eulerian velocity differs from each other by a phase-factor in Fourier space, they have the same energy spectrum. Here the symbol $\langle \cdot \rangle$ denotes averaging over snapshots of velocity [see Table 4.1]. The energy spectrum from run NS1 is shown in the top panel of Fig (4.1) and NS2 is shown in bottom panel. In our simulation we have to track one referrence Lagrangian particle. A representative Lagrangian path of this reference particle is shown in Fig. (4.2). We next calculate the physical space equal-time structure functions, defined by,

$$S_p(\vec{x}, r) \equiv \left\langle \left| [\vec{u}(\vec{x} + \vec{r}) - \vec{u}(\vec{x})] \cdot \left(\frac{\vec{r}}{r} \right) \right|^p \right\rangle \quad (4.35)$$

for both quasi-Lagrangian and Eulerian velocities. The symbol $\langle \cdot \rangle$ denotes averaging over snapshots of velocity. In principle, in physical space we should also average over \vec{x} and \vec{r} such that $|\vec{r}| = r$. But such an averaging has very high computational cost [$O(N^6)$]. Hence our real space structure functions are not so well averaged as the shell averaged energy spectrum in Fourier space. Representative plots of $\log_{10}[S_p(r)]$ versus $\log_{10}(r)$ for $p = 3, 5$ and 6 , are shown respectively in Fig (4.3) and Fig (4.4). The Eulerian and quasi-Lagrangian physical space structure functions are not equal to each other. We expect that this discrepancy will decrease monotonically as we increase the time span over which we average our

quasi-Lagrangian structure functions. Almost no scaling range is observed from these physical-space structure functions. To extract order- p multiscaling exponent ζ_p the structure functions are plotted using extended self similarity (ESS). The ESS style plots for $p = 4$ and 6 are shown in Fig (4.5) and Fig (4.6). The multiscaling exponents ζ_p extracted from the ESS plots are shown in Fig. (4.7). The Eulerian and quasi-Lagrangian multiscaling exponents equal to each other within our present numerical accuracy.

Next we show representative time series of velocity difference for both quasi-Lagrangian and Eulerian velocities in Fig. (4.8). Note that the the quasi-Lagrangian velocity fluctuates much faster than than the Eulerian velocity. Similar phenomenon was observed for time-series of Lagrangian and Eulerian velocities in Ref. [13]. From these time-series we calculate the time-dependent structure functions. In what follows we show only plots of second-order time-dependent structure function of in physical space, defined by:

$$F_2(r, t) \equiv \frac{1}{S_2(\vec{x}, r)} \langle \delta u_{\parallel}(\vec{x}, \vec{r}, 0) \delta u_{\parallel}(\vec{x}, \vec{r}, t) \rangle \quad (4.36)$$

$$\delta u_{\parallel}(\vec{x}, \vec{r}, t) \equiv [\vec{u}(\vec{x} + \vec{r}, t) - \vec{u}(\vec{x}, t)] \cdot \left(\frac{\vec{r}}{r} \right) \quad (4.37)$$

Here δu_{\parallel} denotes the longitudinal component of either the Eulerian or the quasi-Lagrangian velocity difference. In the top panel of Fig. (4.9) representative plots of $F_2(r, t)$ for 3 different values of $r = |\vec{r}|$, namely, $r = 20, 40, 80$ lattice-spacing, for Eulerian velocity. In the bottom panel of Fig. (4.9) similar plots are shown for the quasi-Lagrangian velocity.

Observe that for very small time the time-dependent structure functions are slightly greater than unity. This shows that these time-dependent structure functions have to be averaged for much longer times than in our study. The time-dependent structure functions plotted here are averaged over about 3 large-eddy-turnover time. Our simulations are done in two different computers. Our code is

shared memory parallelised. In IBM Regatta with 16 processors one large-eddy-turnover time takes about 16 days of CPU time. In an ALTIX machine with 16 processor we need about 20 days of CPU time. We have also calculated higher order ($p > 2$) time-dependent structure functions too, but they need to be averaged even longer to get reliable data. As the characteristic time scale of fluctuation of Eulerian and quasi-Lagrangian velocity are widely different, we need two different sampling rates for them. In our simulations we have used $10\delta t$ as the sampling rate for quasi-Lagrangian velocities and $100\delta t$ as the sampling rate for Eulerian velocities.

4.4 Conclusion and future studies

In this Chapter we have reported our preliminary results from 512^3 and 256^3 quasi-Lagrangian DNS. The algorithm for obtaining quasi-Lagrangian velocities have been developed by us. Our equal-time data agrees reasonable well with theoretical expectations. Our different-time data shows qualitatively correct trend, i.e.,: the characteristic time scale of fluctuation of Eulerian velocities are much smaller than their quasi-Lagrangian counterparts. But unfortunately, we find that to get reliable dynamic data we need much longer averaging compared to what we have been able to achieve so far.

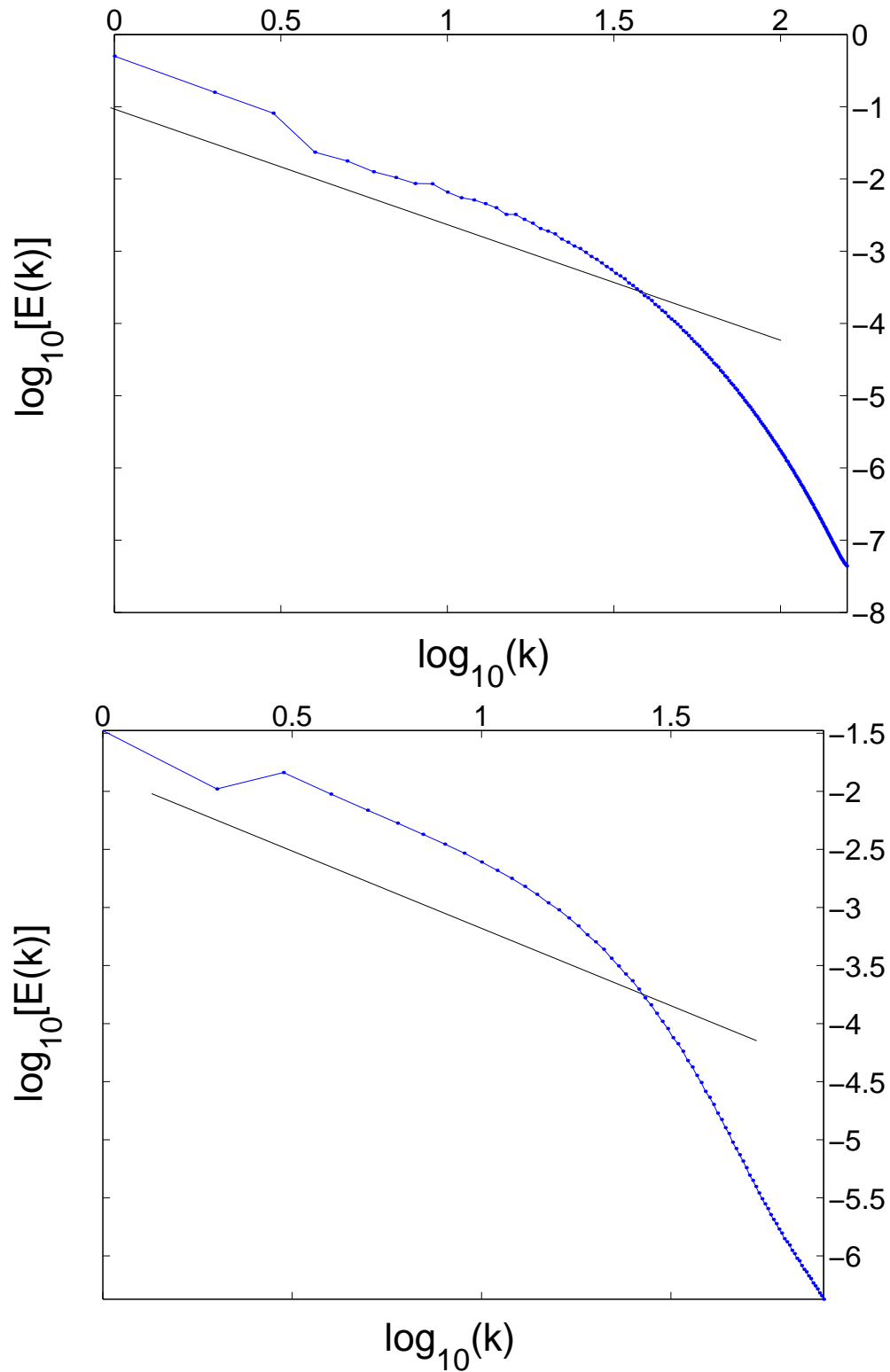


Figure 4.1: A representative plot of $E(k)$ versus k (in log-log scale) plotted from our run NS1(top) and NS2(bottom). Both the plots show a small range (roughly three-fourth of a decade) of scaling range. The slope of the straight line is $-5/3$.

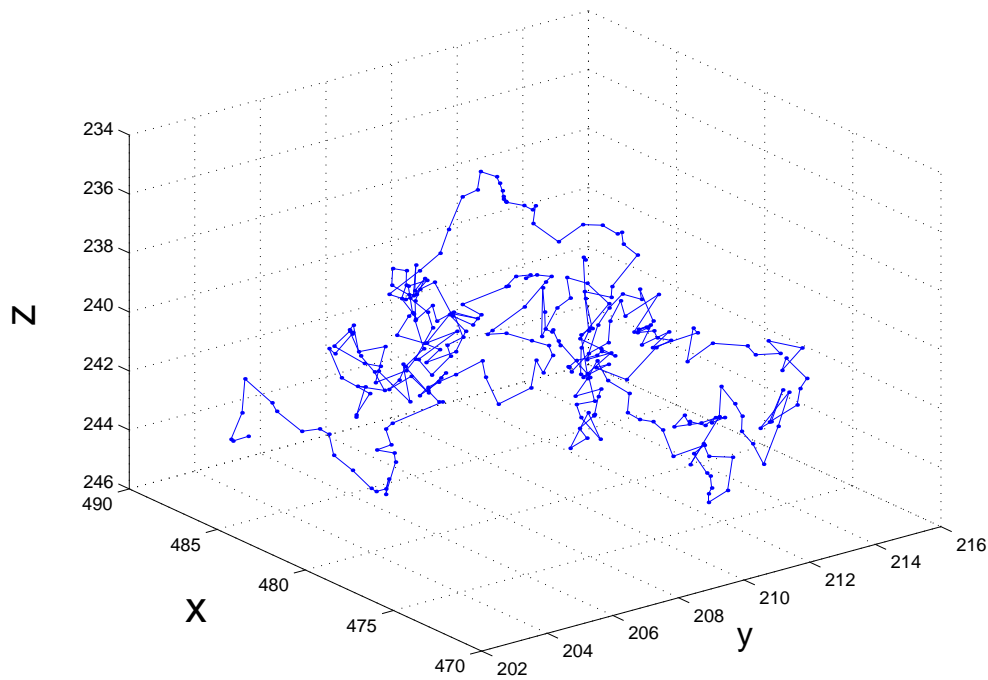


Figure 4.2: A representative plot of the Lagrangian path of our reference particle. The position of the particle is shown after every 10 iterations. This plot corresponds to approximately 1/20-th of the Large-eddy turnover time. (From NS1)

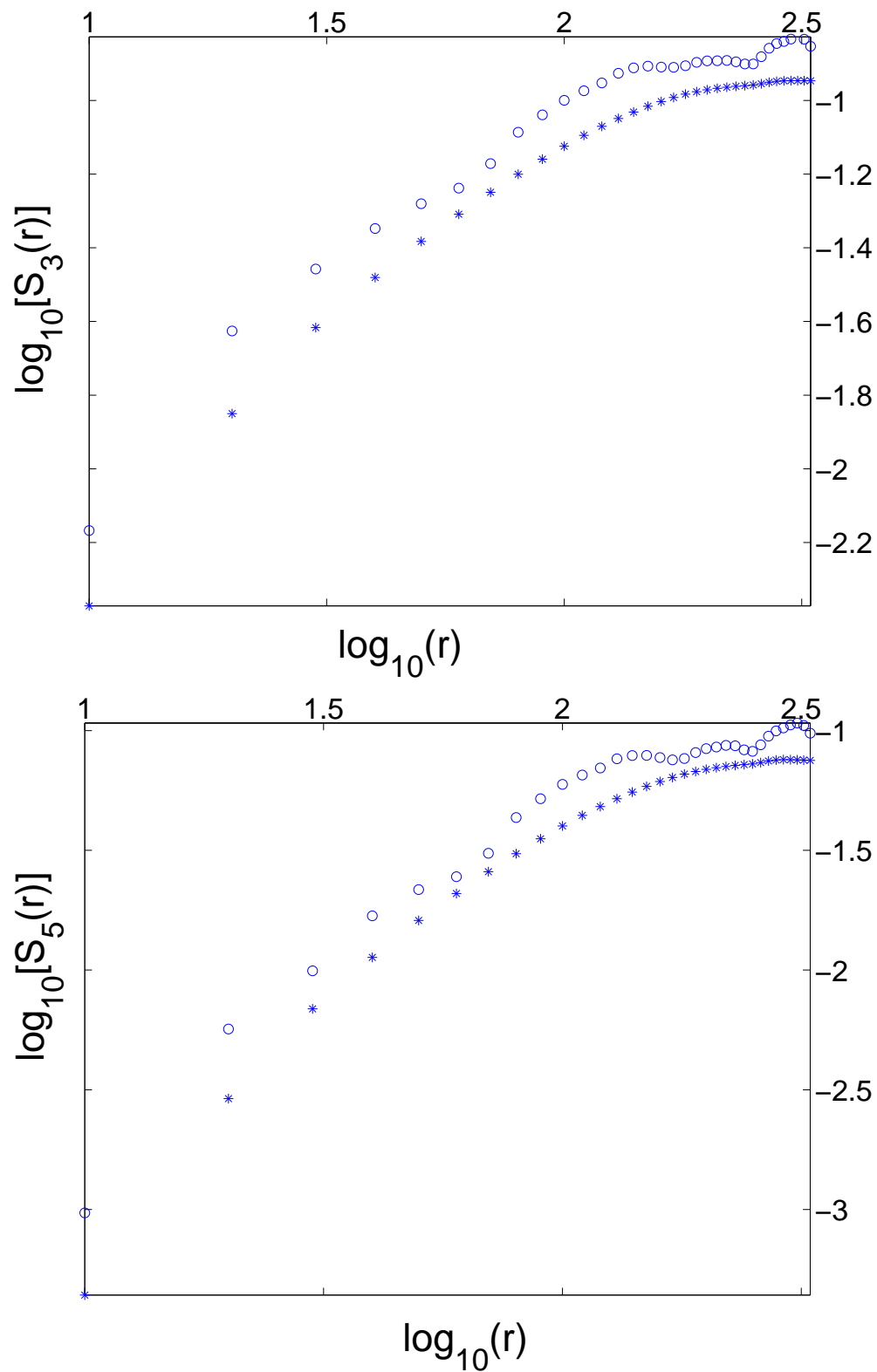


Figure 4.3: A representative plot of the order-3 (top panel), and order-5 (bottom panel) structure function of Eulerian (circles) and quasi-Lagrangian (asterisks) longitudinal velocity difference. None of the plots show any effective scaling range. Note that plot of quasi-Lagrangian structure functions look smoother than the Eulerian ones. (From NS1)

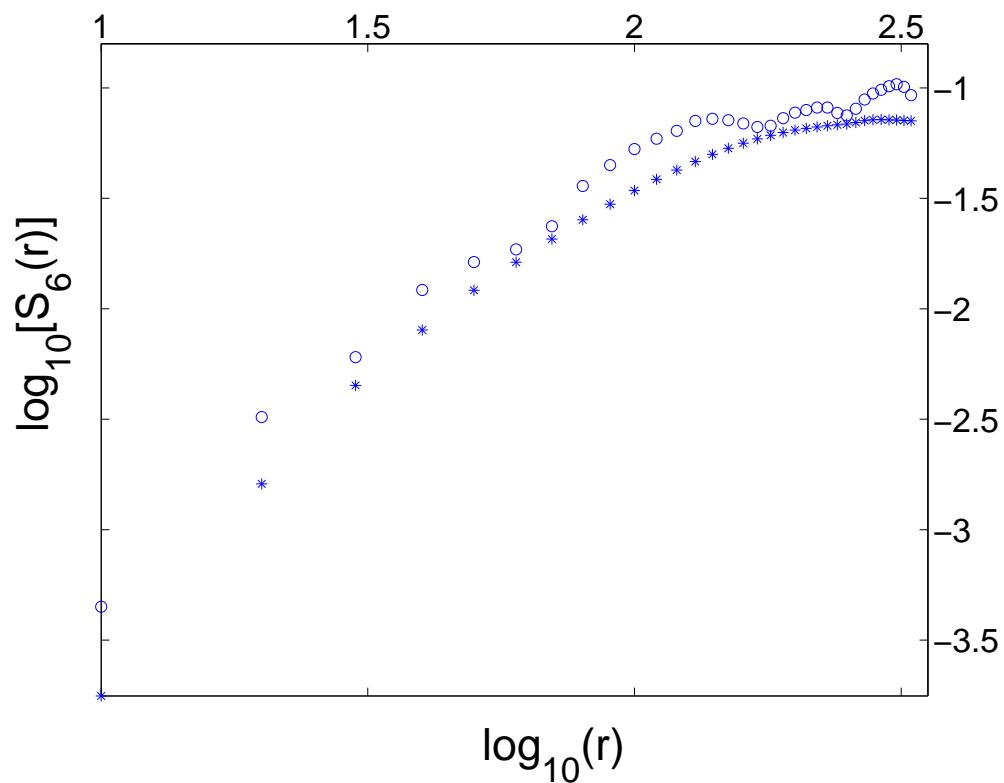


Figure 4.4: A representative plot of the order-6 structure function of Eulerian (circles) and quasi-Lagrangian (asterices) longitudinal velocity difference. None of the plots show any effective scaling range. Note that plot of quasi-Lagrangian structure functions look smoother than the Eulerian ones.

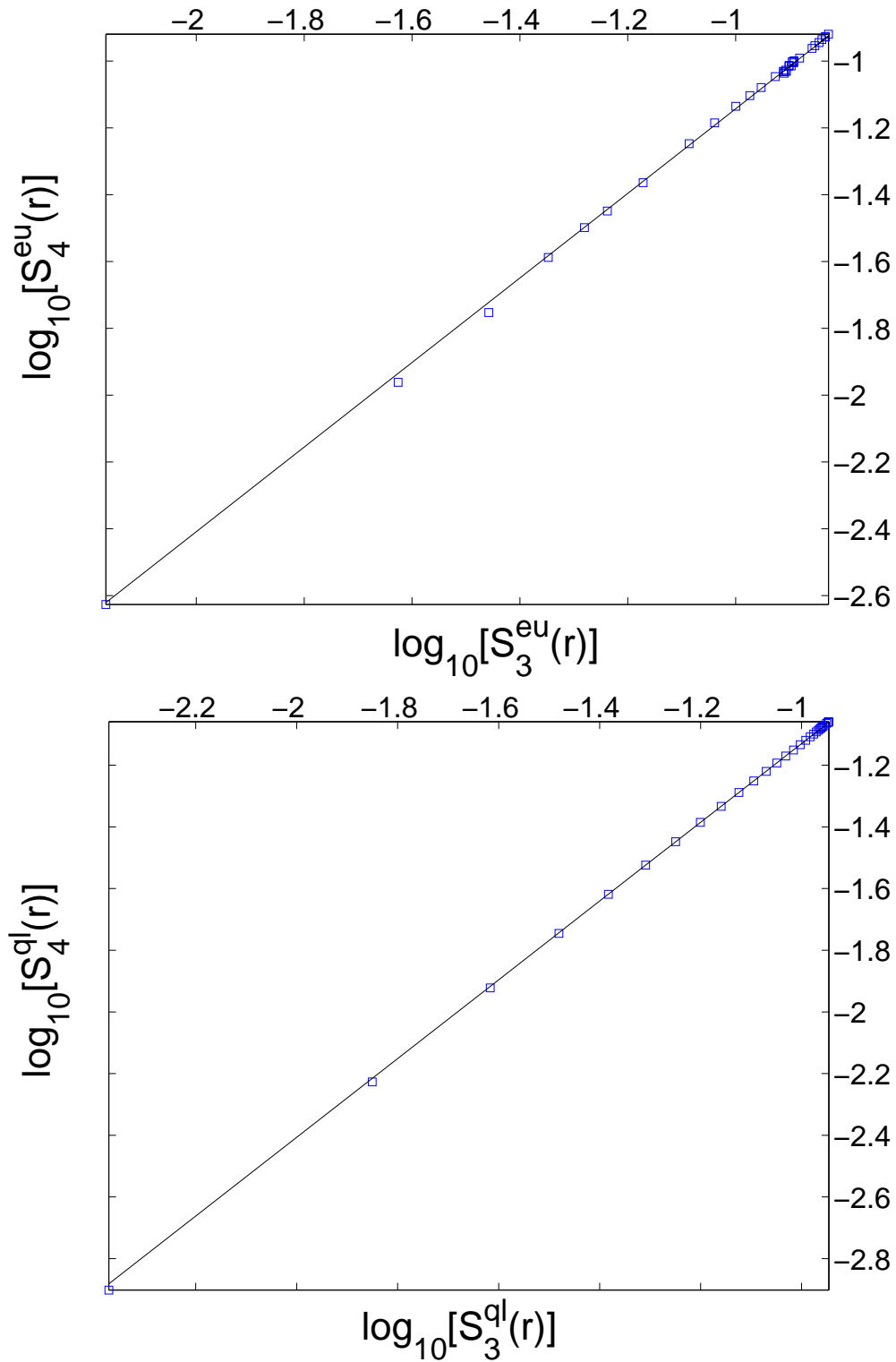


Figure 4.5: An ESS style plot of the $\log_{10}[S_4(r)]$ vs $\log_{10}[S_3(r)]$ for Eulerian (top panel) and quasi-Lagrangian (bottom panel) velocity. The equal-time multiscaling exponents are extracted by least-square fits from these and similar plots.

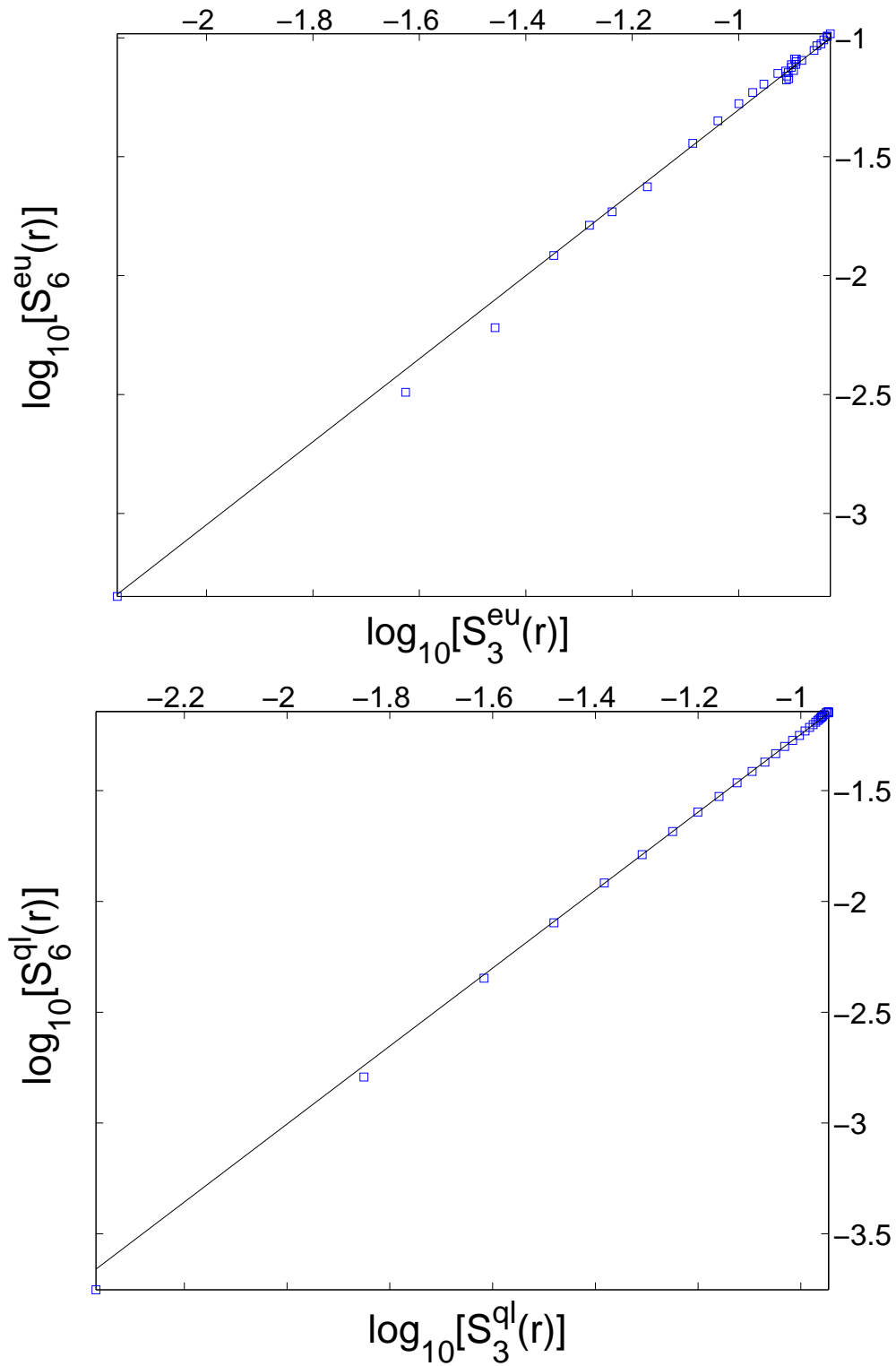


Figure 4.6: An ESS style plot of the $\log_{10}[S_6(r)]$ vs $\log_{10}[S_3(r)]$ for Eulerian (top panel) and quasi-Lagrangian (bottom panel) velocity. The equal-time multiscaling exponents are extracted by least-square fits from these and similar plots.

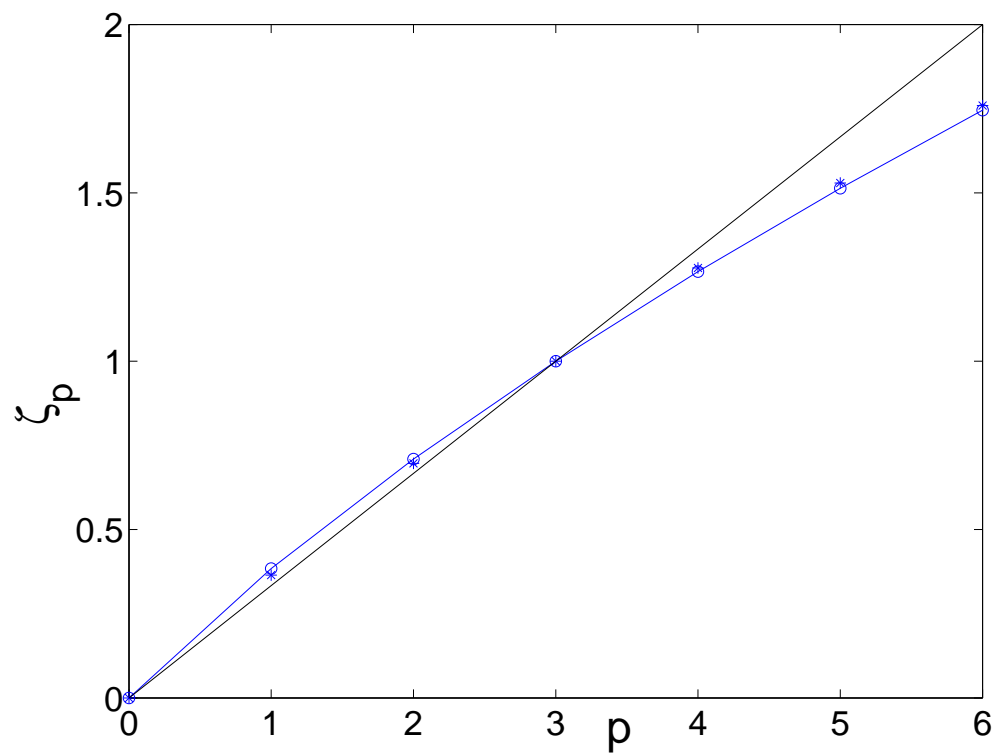


Figure 4.7: A plot of multiscaling exponents ζ_p versus p for Eulerian (circles) and quasi-Lagrangian (asterices) velocity. Thus our runs are long enough to give equal-time multiscaling exponents for both Eulerian and quasi-Lagrangian structure functions if we use ESS procedure.

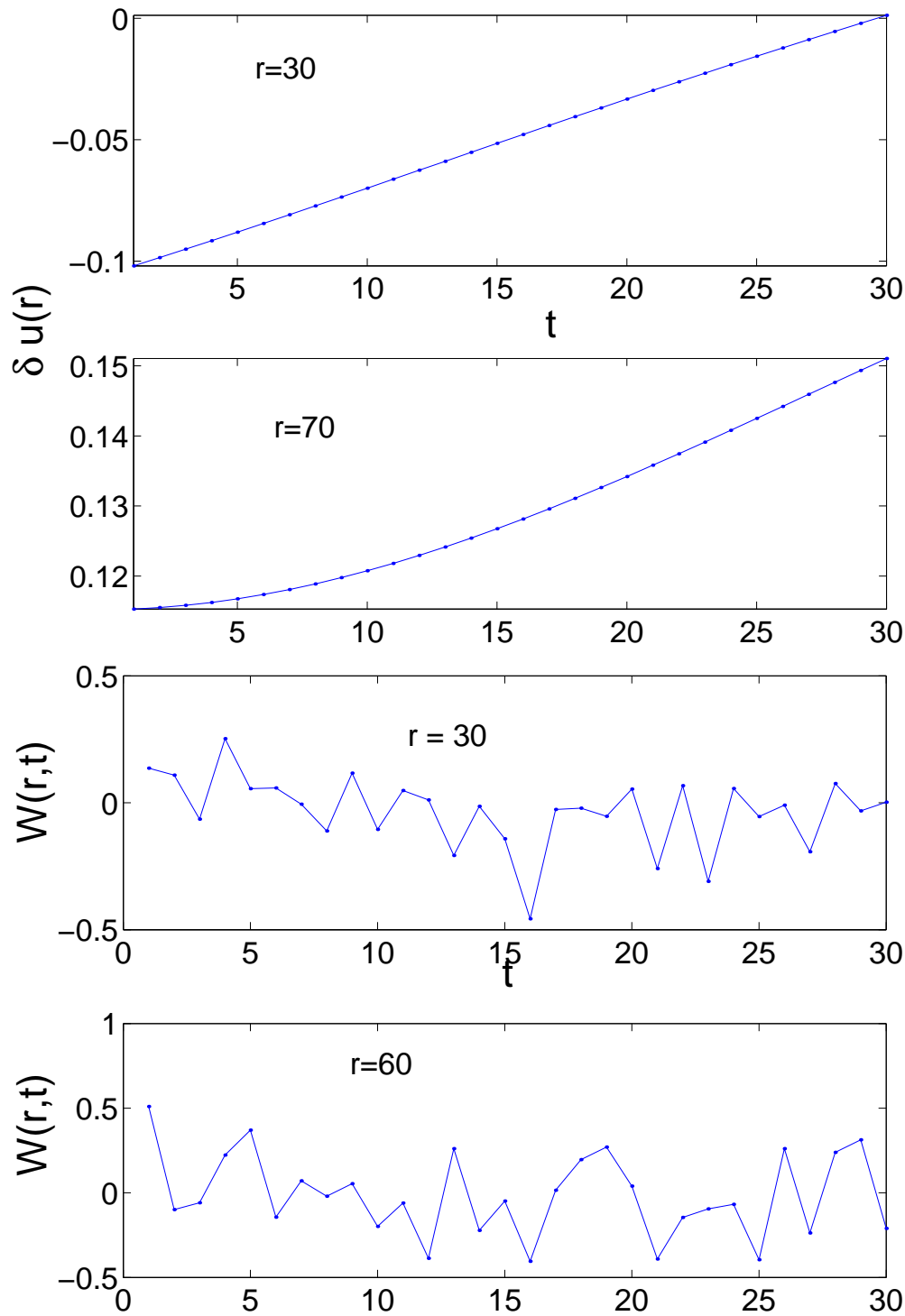


Figure 4.8: Representative plot of time-series of Eulerian (top plot) and quasi-Lagrangian (bottom plot) velocity differences. The variation of the quasi-Lagrangian velocity are much faster than the Eulerian ones. The time axis in this figure corresponds to 30 iterations.

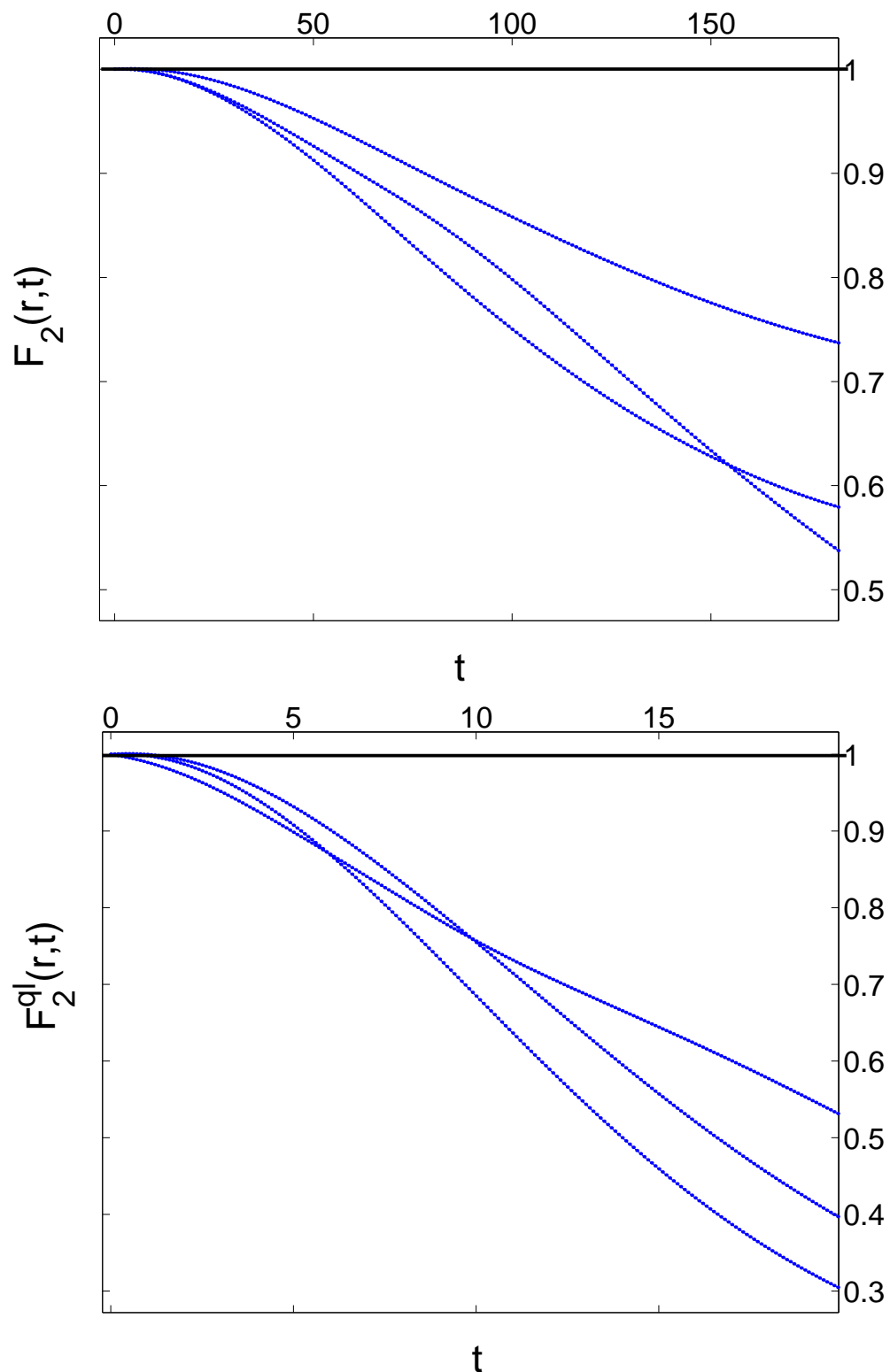


Figure 4.9: Representative plot of $F_2(r, t)$ of Eulerian (top plot) and quasi-Lagrangian (bottom plot) velocity differences. Note that for very small time the functions F_2 becomes larger than unity. This is a signature of poor averaging. The time axis is plotted in the unit of $100\delta t$. Note that the quasi-Lagrangian velocity time-dependent structure function decays much faster than its Eulerian counterpart. In both the plots $r = 20, 40, 80$.

Bibliography

- [1] D. Mitra and R.Pandit, Phys. Rev. Lett **93**, 024501 (2004).
- [2] P. Yeung and S. Pope, J. Fluid Mech. **207**, 531 (1989).
- [3] L. Biferale, G. Boffetta, A. Celani, B. Devenish, A. Lanotte, and F. Toschi, nlin.CD/0403020 (2004).
- [4] F. Hayot and C. Jayaprakash, Phys. Rev. E **57**, R4867 (1998).
- [5] F. Hayot and C. Jayaprakash, Int. J. Mod. Phys. B **14**, 1781 (2000).
- [6] V. Belinicher and V. L'vov, Sov. Phys. JETP **66**, 303 (1987).
- [7] V. L'vov and I. Procaccia, Phys. Rev. E **52**, 3840 (1995).
- [8] V. L'vov and I. Procaccia, Phys. Rev. E **52**, 3858 (1995).
- [9] V. L'vov and I. Procaccia, Phys. Rev. E **53**, 3468 (1996).
- [10] V. L'vov, E. Podivilov, and I. Procaccia, Phys. Rev. E **55**, 7030 (1997).
- [11] G. Falkovich, K. Gawędzki, and M. Vergassola, Rev. Mod. Phys. **73**, 913 (2001).
- [12] G. Come-Bellot and S. Corrsin, J. Fluid. Mech. **48**, 273 (1971).
- [13] D. Shlien and S. Corrsin, J. Fluid. Mech. **62**, 255 (1974).
- [14] Y. Kaneda, T. Ishihara, and K. Gotoh, Phys. Fluids. **11**, 2154 (1999).

Chapter 5

Multiscaling in the Stochastically Forced Burgers Equation

5.1 Introduction

Earlier in this thesis, we have discussed how homogeneous, isotropic fluid turbulence is often characterised by the order- p velocity structure functions

$$S_p(\ell) = \langle [\{ \vec{u}(\vec{x} + \vec{\ell}) - \vec{u}(\vec{x}) \} \cdot (\frac{\vec{\ell}}{\ell})]^p \rangle, \quad (5.1)$$

where $\vec{u}(\vec{x})$ is the velocity at the point \vec{x} and the angular brackets denote an average over the statistical steady state of the turbulent fluid. For separations ℓ in the inertial range $\eta_d \ll \ell \ll L$, one has

$$S_p(\ell) \sim \ell^{\zeta_p}. \quad (5.2)$$

Here η_d is the small length scale at which dissipation becomes important; L is the large length scale at which energy is fed into the fluid. The velocity spectrum $E(k)$, related by a spatial Fourier transform to $S_2(\ell)$, displays a power-law dependence on wave-vectors k in the inertial range. The 1941 theory (K41) of Kolmogorov [1] predicts *simple scaling* with exponents $\zeta_p^{K41} = p/3$; and $E(k) \sim k^{-5/3}$. By contrast, experiments and direct numerical simulations (DNS) suggest *multiscaling* [2] with ζ_p a nonlinear, monotonically increasing, convex function of p , as we have discussed in Chapter 1. The larger the Reynolds number, Re , the larger

is the extent of the inertial range. However, the Reynolds numbers in DNS are limited, so the exponents ζ_p have to be extracted from numerical fits over inertial ranges that extend, at best, over a decade in ℓ . The velocity spectrum $E(k)$ exhibits an inertial range of little more than a decade in k even in a 2048^3 pseudospectral DNS of homogeneous isotropic turbulence [3]. This is the largest simulation done so far¹. The inertial range exhibited by real-space structure functions of order higher than two is generally smaller than the inertial range for $E(k)$. *Extended self similarity* (ESS), discussed in Sec. 1.7.3, that uses log-log plots of $S_p(\ell)$ versus $S_3(\ell)$ to obtain the ratios ζ_p/ζ_3 [4], can extend the apparent inertial range, but its theoretical basis remains unclear. Experiments certainly show much large inertial ranges but they have other limitations, as discussed in Sec. 1.5. At present, in fluid turbulence, multiscaling of velocity structure functions seems to be plausible but not established conclusively. A *definitive* confirmation must await careful simulations at Reynolds numbers much higher than can be achieved at present. It is important therefore to establish, or rule out, multiscaling of structure functions in simpler forms of turbulence, such as passive-scalar, passive-vector or Burgers turbulence.

Significant progress, both analytical and numerical, has been made in confirming multiscaling in passive-scalar and passive-vector problems (Sec. 1.9). But the linearity of the passive-scalar and passive-vector equations is a crucial ingredient of these studies, so it is not clear how they can be generalised to fluid turbulence and the Navier–Stokes equation. In view of this situation it would be interesting to investigate multiscaling in simpler but *nonlinear* partial differential equations. A potential candidate is the Burgers equation. However, when forced, stochastically or deterministically, only at large spatial scales (as in the typical fluid turbulence experiment), the Burgers equation shows simple bi-scaling of velocity

¹Preliminary data are available from an 4096^3 pseudospectral DNS [3]

structure functions. In the decaying case such biscaling is also obtained for random initial velocities with power-law correlations. Here we consider an external force which is *not limited* to the large spatial length scales. This problem has been studied previously in Refs. [5, 6, 7, 8, 9, 10]. It is by far the simplest *nonlinear* partial differential equation (PDE) that has the potential to display multiscaling of velocity structure functions; and it is akin to the Navier–Stokes equation. In particular we investigate the statistical properties of the solutions to

$$\partial_t \mathbf{u} + \mathbf{u} \partial_x \mathbf{u} = \nu \partial_{xx} \mathbf{u} + f(x, t), \quad (5.3)$$

in the limit of vanishing viscosity $\nu \rightarrow 0$, which corresponds to the limit of large Reynolds number in fluid turbulence. Here \mathbf{u} is the velocity and $f(x, t)$ is a zero-mean, space-periodic Gaussian random force with

$$\langle \hat{f}(\mathbf{k}_1, t_1) \hat{f}(\mathbf{k}_2, t_2) \rangle = 2D_0 |\mathbf{k}|^\beta \delta(t_1 - t_2) \delta(\mathbf{k}_1 + \mathbf{k}_2) \quad (5.4)$$

and $\hat{f}(\mathbf{k}, t)$ the spatial Fourier transform of $f(x, t)$. We restrict ourselves to the case $\beta = -1$, and show from very high-resolution numerical simulation, that the scaling exponents of the structure functions for this problem shows multiscaling, whereas earlier, low-resolution studies had obtained bifractality.

The rest of this Chapter is organised in the following way. In Sec. 5.2 we give a short summary of earlier studies with $\beta = -1$. Next, in Sec. 5.3 we describe our numerical algorithm for the forced Burgers equation in the limit $\nu \rightarrow 0$. The main results of our simulation, the structure functions and their scaling exponents, are described in the Sec. 5.4. In Sec. 5.5 we investigate and rule out the possibility that the multiscaling we observe for $\beta = -1$ is a numerical artifact. In Sec. 5.6 we consider the consequences of the breakdown of simple scale invariance for the probability distribution of shock strengths.

5.2 Review of earlier work

The Burgers equation, forced only at large spatial scales, has been studied extensively [11, 12]. Recent numerical studies, with a deterministic forcing at large spatial scale [13] and periodic boundary conditions, have found statistical steady state in which there are a few shocks of order unity strengths in the computational domain. As discussed for the unforced case in Chapter 1 this leads to bifractal scaling:

$$S_p^{\text{abs}}(r) \sim r^{\xi_p}, \quad (5.5)$$

where

$$\begin{aligned} \xi_p &= p, & p \leq 1; \\ &= 1. & p \geq 1. \end{aligned} \quad (5.6)$$

The same result has been obtained for stochastic Gaussian force, that is limited to large spatial scales, but is white-in-time [11, 12]. By using replica-symmetry methods, the authors of Ref. [11] concluded that a small correlation in time would not change the multiscaling properties.

Studies where the forcing is not limited to small Fourier modes and the forcing spectrum follows a power-law, as in Eq.(5.4), was first studied in Ref. [14]. Here we can divide the earlier studies into two broad classes :

$$\begin{aligned} \beta &\geq 0 && \text{(case A);} \\ \beta &< 0 && \text{(case B).} \end{aligned} \quad (5.7)$$

For case A an ultraviolet cutoff at a large Fourier mode Λ is assumed, and for case B an infrared cutoff at small Fourier mode k_0 is assumed.

Several renormalisation-group studies have been carried out for the KPZ equation, which describes surface growth. The height of the surface $[\psi(x, t)]$ corresponds to the velocity potential in Burgers equation, namely,

$$\psi(x, t) = -\partial_x u(x, t). \quad (5.8)$$

And the force in the KPZ equation $F(x, t)$ is related to $f(x, t)$ by

$$F(x, t) = -\partial_x f(x, t). \quad (5.9)$$

Hence the scaling exponent for the co-variance of $F(x, t)$, α , is related to β by,

$$\alpha = \beta - 2 \quad (5.10)$$

This mapping has been discussed in Section (1.11).

Most of the RG studies of KPZ equation is limited to case A, where one is primarily interested in the space-time, height-height structure function

$$\langle |\psi(x, t) - \psi(x', t')|^2 \rangle \sim |x - x'|^{2\chi} f \left[\frac{|t - t'|}{|x - x'|^z} \right], \quad (5.11)$$

where χ is called the roughness exponent for the interface, and z the dynamic exponent. The following is a summary of the results obtained in one spatial dimension:

- For $-1/2 < \alpha < 0$ ($3/2 < \beta < 2$) [15]

$$\chi = 1/2, \quad z = 2 - \chi \quad (5.12)$$

- For $-2 < \alpha < -1/2$ ($0 < \beta < 3/2$) [15]

$$\chi(\beta) = 1 - \frac{\beta + 2}{3}, \quad z = 2 - \chi \quad (5.13)$$

- For $\alpha < -2$ (i.e., $\beta < 0$) the RG methods of Ref. [15] fails to work.

The case B has been studied by RG methods, for $\beta = -2$, in Refs. [14, 16]. They find the wave-vector and frequency space dependent, velocity-velocity, correlation function

$$C(k, \omega) \equiv \frac{1}{8\pi^2} \langle u(k, \omega) u(-k, -\omega) \rangle = k^{-3/2} \Phi \left(\frac{\omega}{\alpha k^{3/2}} \right), \quad (5.14)$$

where ω is the frequency, α is a numerical constant, and Φ is a universal scaling function. These results were also supported by numerical simulations [16].

The case $\beta = -1$ have been studied by numerical simulation of the Burgers equation, in Refs [5, 6, 8, 9, 10]. We now summarise the results of these studies.

- References [5, 6] used a two-third de-aliased, pseudo-spectral method with $12228 = 3 \times 2^{12}$ grid points and a viscosity $\nu = 9 \times 10^{-40}$. The external driving force is Gaussian, white-in-time, with a spectrum proportional to $1/k$ where k is the wave-vector. They found that:

1. A snapshot of the velocity as a function of space shows a sawtooth structure typical of a Burgers velocity field; in addition a random component is on it. The system spends most of its time in the state where there are a few (about 3-4) large-amplitude shocks and many small-amplitude ones [5].
2. The energy spectrum in Fourier space [5] was found to be consistent with,

$$E(k) \sim k^{-5/3}. \quad (5.15)$$

No error-bars were quoted for this $-5/3$ exponent.

3. The order- p velocity structure functions, were found to scale as

$$S_p^{\text{abs}}(r) \equiv \langle |u(x+r) - u(x)|^p \rangle \sim r^{\xi_p}, \quad (5.16)$$

with scaling exponents ξ_p .² The scaling range was close to a decade in r . Point 2 above implies $\xi_2 = 2/3$. References [5, 6] suggested that bifractal scaling is obtained for this model with

$$\begin{aligned} \xi_p &= p/3, & p \leq 3; \\ &= 1, & p \geq 3. \end{aligned} \quad (5.17)$$

Even-order structure functions, up to 8-th order, was studied in Ref. [5], and odd-order and fractional-order structure functions were calculated

²Let us stress here that we are making clear distinction between scaling exponents of order- p structure functions with absolute value (ξ_p) and without (ζ_p).

for $p = 1/3, 2/3, \dots, 2$ in Ref [6]. The comparison between this type of bifractality and the one obtained for large-scale forcing, i.e., Eq.(5.6), is shown in Fig.(5.1). A simple scaling argument given below, (from Section(9.6.4.1) of Ref.[2]) can reproduce this kind of bi-fractal scaling. Let us assume that, with a force f given by Eq.(5.4), the velocity field attains a statistical steady state. We also assume that, in this statistical steady state, there is no fractal or multifractal clustering of shocks. To investigate the scaling properties of velocity differences $\delta u(r)$ across a length scale r , let us first assume that the length scale r contains no shock. Then the scaling behaviour can be obtained in the following fashion:

The unforced Burgers equation, in the limit $\nu \rightarrow 0$, is invariant under the following scale transformation:

$$x \rightarrow \lambda x, \quad t \rightarrow \lambda^{1-h} t, \quad \text{and} \quad u \rightarrow \lambda^h u, \quad (5.18)$$

for any real number h , as each term in the equation picks up a factor of λ^{2h-1} . This transformation of length and time scale implies that the external force scales as,

$$f(\lambda x, \lambda^{1-h} t) \rightarrow \lambda^{(h-\beta-2)/2} f(x, t). \quad (5.19)$$

Now if we demand the scale invariance of the *stochasticall forced* Burgers equation, Eqs. (5.3) and (5.4), we must have

$$2h - 1 = \frac{h - \beta - 2}{2}, \quad (5.20)$$

i.e., $h = -\frac{\beta}{3}$. Hence velocity difference across a length scale r must scale as,

$$\delta u(r) \sim r^{-\beta/3}. \quad (5.21)$$

If, however, the length interval r contains a shock then the velocity difference across r is a constant (the strength of the shock) and the probability that the length difference r contains a shock is $\sim r$. Hence the order- p structure function consists of two contributions, one that follows from Eq. (5.21) and another dominated by shocks, that is linear in r :

$$S_p^{\text{abs}}(r) \equiv \langle |\delta u|^p \rangle \sim Ar^{-p\beta/3} + Br, \quad (5.22)$$

where A and B are numerical constants independent of r . In the limit of small r we have

$$\begin{aligned} \xi_p &= -\beta p/3, & p &\geq \frac{3}{\beta}; \\ &= 1. & p &\leq \frac{3}{\beta}. \end{aligned} \quad (5.23)$$

This reduces to Eq. (5.17) for $\beta = -1$. Note that the crucial assumption we have made is the there is *no fractal or multifractal clustering of shocks*.

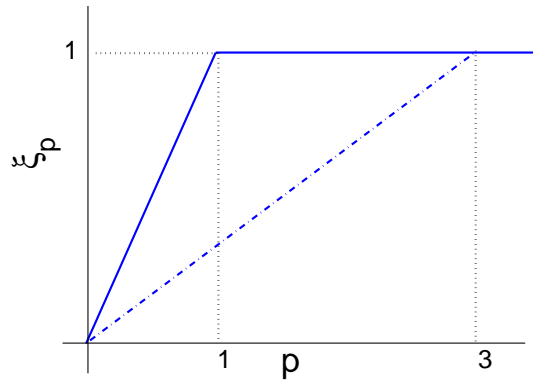


Figure 5.1: Plot comparing the two different bifractalities in Eq.(5.6) (continuous line) and Eq.(5.17)(broken line).

4. The tail of the probability distribution function, $P[\delta u(r)]$, of velocity difference $\delta u(r)$ across a length scale r follows a power-law

$$P[\delta u(r)] \propto (\delta u)^{-\rho} \quad (5.24)$$

with $\rho \simeq 4$.

- The studies of Refs. [8, 9, 10] with 4096 Fourier modes and $\nu = 0.01$, calculated the structure functions

$$S_p(r) \equiv \langle [u(x+r) - u(x)]^p \rangle \sim r^{\zeta_p}. \quad (5.25)$$

Where ζ_p are multiscaling exponents for structure functions of velocity differences (and *not* of the absolute value of velocity differences). The results of Refs. [8, 9, 10] essentially supported the findings of Refs. [5, 6] but studied principally the range of $-1 \leq \beta < 0$, and found numerical evidence in support of the following :

1. The scaling exponents ζ_p depends on β .
2. ζ_p is a non-linear function of p , i.e., velocity structure functions show multiscaling; for the case $\beta = -1$ the authors argued for simple bifractal scaling.

We have revisited the case $\beta = -1$ with state-of-the-art numerical technique which yields close to three decades to scaling range for $S_p^{\text{abs}}(r)$. As a consequence we can measure the multiscaling exponents (ξ_p) with much better accuracy than has been possible before. Our results provide strong numerical evidence for multiscaling, in contradiction of earlier results.

5.3 Algorithm and numerical details

We overcome the limitations of the earlier studies of Refs. [5, 6, 8] by adapting the algorithm of Refs. [13, 17] to develop a state-of-the-art technique for the numerical solution of Eqs. (5.3) and (5.4), in the $\nu \rightarrow 0$ limit. Our simulations are done in a periodic domain of size $L = 2\pi$ and with $D_0 = 1$, without loss of generality. We approximate the white-in-time nature of the force as follows:

1. We add the external force, $F(x, t)$, such that

$$f(x, t) = -\partial_x F(x, t) \tag{5.26}$$

not to the Burgers velocity, but to the velocity potential ψ .

2. Furthermore, for numerical convenience, we introduce an ultraviolet cutoff Λ for the force by setting $\hat{F}(k, t) = 0$ for $k \geq \Lambda$.
3. At time $t_n = n\delta t$ we add $F_n(x)\sqrt{\delta t}$ to the Burgers potential $\psi(x, t)$, where the $F_n(x)$ s are independent Gaussian random functions with zero mean and $\frac{1}{k^3}$ spectrum. This is equivalent to Eq. (5.4) with $\beta = -1$ by virtue of Eq. (5.10). The addition of this force is often referred to as kicking, so we will adopt this term.
4. To integrate the solution between two time steps we use a well-known result on the solutions to the unforced Burgers equation in the limit of vanishing viscosity (see, e.g., Section(1.11.2) and Ref. [18]): the velocity potential ψ (such that $u = -\partial_x \psi$) obeys the maximum principle

$$\psi(x, t_{n+1}) = \max_y \left(\psi(y, t_n) - \frac{(x - y)^2}{2\delta t} \right). \tag{5.27}$$

This means that the Lagrangian particle, which at time $t_{n+1} = t_n + \delta t$ is at the point x , was at the point y at time t_n ; the value of y is such that it satisfies the maximum condition on the right-hand-side (RHS) of Eq. (5.27). The map from x to y is called an inverse Lagrangian map. The search for the maxima in Eq. (5.27) might seem, at first, to require $O(N^2)$ operations; however, only $O(N \log_2 N)$ [17] are required, as we illustrate now. In a computational domain of N grid points we first find out the value of $y \equiv y_{N/2}$ which satisfies the RHS of Eq. (5.27) for $x = N/2$. As the Lagrangian particles do not cross each other but stick to each other when they collide (see page 40), which is the mechanism of dissipation of energy, for $0 \leq x < N/2$

the search for the maxima in the RHS for Eq. (5.27) can be limited to the region $0 < y \leq y_{N/2}$, and for $N/2 < x \leq N$ in the region $y_{N/2} \leq y \leq N$. Hence the search for the maxima in Eq. (5.27) becomes a binary search which can be done in $O(N \log_2 N)$ operations.

5. And finally the velocity $u(x, t) = -\partial_x \psi(x, t)$ is found by evaluating the numerical derivative of ψ by a right-handed first order finite-difference; i.e., at a grid point i ,

$$u(i, t) = -\frac{\psi(i, t) - \psi(i + 1, t)}{\delta x} \quad (5.28)$$

6. Our numerical method will give meaningful results only if δt satisfies the following restrictions:

- (a) If δt is chosen to be so small that in this time a typical Lagrangian particle moves less than half the grid spacing, then we always find $\psi(x, t_{n+1}) = \psi(y, t_n)$, where $t_{n+1} = t_n + \delta t$. Thus δt should not be too small.
- (b) Furthermore δt should not be too large: If the time step δt is too large, then our kicked scheme does not measure properties of the forced Burgers equation but the decaying one. The initial velocity, (because of the kick), at length scale r is $u(r) \sim r^\beta$. Under decaying Burgers dynamics between successive kicks, a velocity of order unity strength takes order unity time to decay. Hence, if the time-step $\delta t > O(r^\beta)$, length scales up to $O(r)$ will show characteristics of decaying burgulence and larger length scales will show characteristic forced burgulence.

By combining the two points mentioned above, if we wish to study forced Burgers turbulence by using this kicked method for length scales as small

as r_s

$$\frac{\delta x}{2u} < \delta t < O(r_s^\beta) \tag{5.29}$$

The values of δt we use are given in Table 5.1. Our method is a variant of the algorithm used in Ref. [13] and shares its advantages over pseudo-spectral DNS (with the same number of grid points). In particular, it yields a much larger scaling range since we work directly in the $\nu \rightarrow 0$ limit.

Run	N	δt	Λ	τ_L	T_{tr}	T_{av}
B1	2^{20}	5×10^{-4}	2^{17}	1	2.0	22
B2	2^{18}	1×10^{-4}	2^{15}	1	2.0	20
B3	2^{16}	1×10^{-4}	2^{13}	1	2.0	120

Table 5.1: The number of grid points N , the time step δt , the ultraviolet cutoff Λ for the stochastic force in Eq. (5.4), and the Burgers-model analogue of the box-size eddy-turnover time τ_L that we use in our simulations B1, B2, and B3. Data from T_{tr} time steps are discarded so that transients die down. We then average our data for an averaging time T_{av} .

Since our simulations are very long, it is crucial that we use a good-quality random-number generator, with a long repeat period. We have used two different random number generators, one with a repeat period of 2^{70} , due to Knuth [19] and another one called the *Marsene Twister*.³ We get the same results by using either of them. Our simulations are done for three different numbers of grid-points to unearth any possible systematic size-dependence, which we rule out (see below). Table 5.1 gives the parameters used in our simulations such as the number N of grid points, the averaging time T_{av} , and the ultraviolet cutoff Λ on the force. The Large-eddy-turnover time, defined as in fluid turbulence, is $\tau_L \approx U/L$, where U is the largest velocity in the system and $L = 2\pi$ the length of our computational box. The largest velocity in our simulation is $O(L)$ and so we have $\tau_L \approx 1$.

³This fascinating random number generator is fast and claims to have "Far longer period and far higher order of equidistribution than any other implemented generators. (It is proved that the period is $2^{19937-1}$, and 623-dimensional equidistribution property is assured.)". See the webpage: <http://www.math.sci.hiroshima-u.ac.jp/m-mat/MT/emt.html>

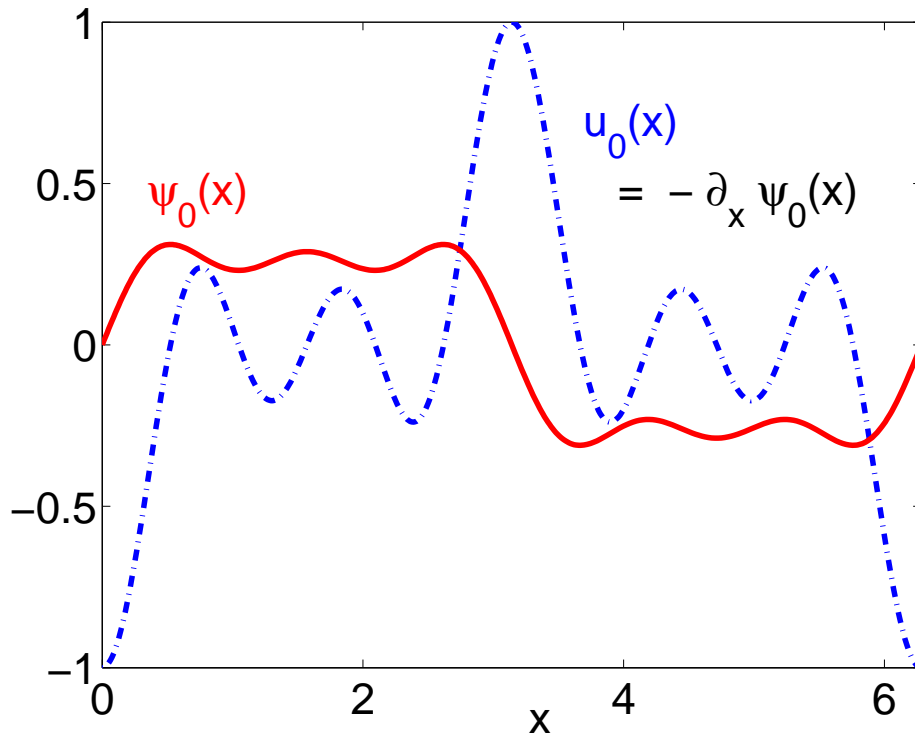


Figure 5.2: Plot of one of the initial conditions used in our simulations. The continuous line is the initial velocity potential ψ_0 and the broken line is the initial velocity u_0 . The maximum initial velocity is prescribed to be unity.

We start our simulations with a smooth $\psi_0(x)$; representative plots which are shown in Fig.(5.2). A representative snapshot of the force $f(x, t) = \partial_x F(x, t)$ is shown in Fig.(5.3). The system seems to attain a nonequilibrium steady state within one large-eddy-turnover time and we obtain velocity profiles (Fig. 5.4) with shocks at all length scales we resolve. Note that the velocity profile develops small scale fluctuations much stronger than those in the force. As the force has an ultraviolet cutoff Λ in Fourier space, at very small scales length scales (smaller than $\sim 1/\Lambda$, which corresponds roughly to 8 grid points in our simulation) the velocity profile looks like it does in decaying Burgers turbulence.

5.4 Results

We have calculated, principally, structure functions with absolute values of velocity differences, across a separation r , namely,

$$S_p^{\text{abs}}(r) \equiv \langle |\delta u(x, r)|^p \rangle, \quad (5.30)$$

$$\delta u(x, r) \equiv u(x + r) - u(x). \quad (5.31)$$

From these we extract the exponents ξ_p defined by

$$S_p^{\text{abs}}(r) \sim r^{\xi_p}. \quad (5.32)$$

Structure functions $S_{\text{abs},p}(r)$ are calculated for $p = m/4$, with integers $1 \leq m \leq 20$. A few representative plots are shown in Figs. (5.5, 5.6, and 5.7) for the run B1, in Figs. (5.9, and (5.10) for the run B2, and in Fig. (5.11) for the run B3. The structure functions from the run B1 exhibit power-law behaviour over nearly three decades of r ; this is more than two decades better than in Refs. [5, 8]. Deviations from this power-law régime occur at small values of r because of the ultraviolet cutoff Λ for the stochastic force (5.4). As we go from smaller to larger system size, i.e., from run B3 to B1, there is no appreciable systematic change in the structure functions, as one can see by comparing the same structure functions plotted for different runs. The scaling exponent of the structure functions also show no appreciable systematic change [see Fig.(5.12)], but of course the scaling range is larger for the runs with higher system sizes.

For each value of N we have calculated ξ_p for $p = m/4$, with integers $1 \leq m \leq 20$. We can obtain the multiscaling exponents ξ_p with great accuracy; our results show genuine multiscaling [Fig. (5.12)], missed hitherto for the case $\beta = -1$. Figure (5.12) summarises the results of our calculations concerning the multiscaling exponents ξ_p , for $N = 2^{16}$, 2^{18} , and 2^{20} ; any systematic change in the values of these exponents with N is much less than our error bars, which are obtained in

the following way: For a given value of p we first determine the local slopes of the plot of $\log S_p^{\text{abs}}$ versus $\log r$ by least-squares fits to all triplets of consecutive points inside the power-law régime. The value of ξ_p we quote [Fig. (5.12)] is the mean of these local slopes; and the error bars shown are the maximum and minimum local slopes in that power-law régime. Two representative plots of the variation of the local slope are shown in the insets of Fig.(5.7).

Figure (5.12) shows that our results for ξ_p , indicated by circles for $N = 2^{20}$, deviate significantly from the bi-fractal-scaling prediction (full lines)⁴. We can conclude, therefore, that we have *genuine multiscaling* in the stochastically forced Burgers equation [Eqs. (5.3, 5.4)] with $\beta = -1$. However, given that simple scaling or bifractal scaling can sometimes be mistaken for multiscaling [20, 21, 22] in a variety of models, it behooves us to check that this is not the case here. We describe below several tests that we have conducted to confirm that the multiscaling we observe is genuine and not an artifact.

5.5 Tests of multiscaling

5.5.1 Von Kármán–Howarth relation

We begin with the third-order structure function of velocity differences, without the absolute value, namely,

$$S_3(r) \equiv \langle \delta u^3 \rangle, \quad (5.33)$$

which satisfies, for Eqs. (5.3) and (5.4), the exact relation

$$\frac{1}{6}S_3(r) = - \int_0^r G(y) dy, \quad (5.34)$$

where $G(y)$ is the spatial part of the force correlation function, defined by $\langle f(x + y, t')f(x, t) \rangle = G(y)\delta(t - t')$. We obtain this analog of the von Kármán–Howarth relation in fluid turbulence by a simple generalisation of the proof given in Ref. [13],

⁴If we limit ourselves to even values of p we still find a significant discrepancy, but only for $p = 4$.

which studied the Burgers equation forced deterministically at large spatial scales. We reproduce the proof in Appendix A. An explicit check of Eq. (5.34) provides a stringent test of our simulations and is shown in Fig. (5.13).

5.5.2 Log-corrected bi-fractality ?

Furthermore, a consequence of Eq. (5.34) is that $S_3(r)$ behaves asymptotically as $r \log(r)$ for small r . Thus we might be tempted to conjecture that $S_p^{\text{abs}}(r)$ also displays, for all p , power-law behaviour consistent with bi-fractal scaling that has, in addition, logarithmic corrections; in finite- N simulations this could appear disguised as multifractality. If this hypothesis were indeed correct, then ESS plots [4] of $\log S_p(r)$ versus $\log S_3^{\text{abs}}(r)$ should have shown larger power-law régimes than in the log-log plots of $S_p^{\text{abs}}(r)$ versus r , [see, e.g., Fig. (5.6)]; and the exponent ratios ξ_p/ξ_3 , extracted from such ESS plots, should have shown bi-fractal scaling. We have, therefore, carried out an ESS analysis: neither does it extend the power-law régime significantly [see Fig.(5.14)] nor does it yield bifractal scaling for ξ_p/ξ_3 [see Fig.(5.15)], thus ruling out log-corrected bifractality masquerading as multifractality. We should also mention here that this method of ruling out log-correction through the use of ESS is obviously not conclusive. This method rules out just the simplest type of logarithmic corrections. To rule out nontrivial form of logarithmic correction it may be enough to understand, from theoretical analysis of this problem, only the third order structure functions, both with and without the absolute value of velocity difference. Such a theoretical analysis is by no means easy: as we have not been able to make significant progress on it.

Note that in fluid turbulence there is indeed a discrepancy between the scaling exponent ξ_p and ζ_p ; but discrepancy between the scaling exponent ξ_3 for $S_3^{\text{abs}}(r)$ and the value unity predicted by the Kármán–Howarth relation is the largest reported so far (more than 10%). Such a discrepancy shows the limitation of naive

multifractal analysis, described in Section(1.7.4), which often borders on dimensional analysis.

5.5.3 Steady-state or transients ?

Next we consider surface-growth models that are akin to Burgers-type equations since the height h of a growing interface is like the Burgers velocity potential ψ here⁵. For a lattice model of surface growth [20], it has been shown that, although the statistical steady state shows no multiscaling, a long-lived transient may show spurious multifractality. We have, therefore, taken care in all our runs (B1-B3 in Table 5.1) that at least $T_{\text{tr}} = 2\tau_L$ time steps are discarded so that transients can die down. We then average our data for structure functions for at least $T_{\text{av}} = 20\tau_L$ (it is here imperative to use a random-number generator with a long repeat period). In run B3, we have run our simulation for $T_{\text{tr}} = 2\tau_L$ and $T_{\text{av}} = 120\tau_L$. We show an evolution of the total energy per grid point,

$$E(t) = \frac{1}{N} \sum_{i=1}^N u^2(i, t) \quad (5.35)$$

as a function of time in Fig.(5.16). Though $E(t)$ fluctuates rapidly, for $t > \tau_L$, it shows no systematic trend as a function of time, supporting the hypothesis that we have indeed reached a nonequilibrium statistical steady state. Furthermore, we have averaged the equal-time structure functions from time $T - \tau_L$ to T with $T/\tau_L = 10, 40, 60, 80,$ and 120 , and obtained five different sets of values for the structure functions $S_p^{\text{abs}}(r)$. A representative plot of $S_2^{\text{abs}}(r)$ is shown in Fig. (5.17), where five different values of the structure function are plotted on one another. The plots coincide for all the points in the scaling range and show small deviations from one another only at very large length scales. This deviation is indeed expected because, to get reliable data at such large length scales, longer averaging

⁵See the mapping from the Burgers to the KPZ equation, describing the growth of an interface, in Section (1.11) and Eq.(1.74).

times are often required. From such plots we have also extracted five sets of scaling exponents ξ_p , these values are well within the error bars shown in Fig. (5.12). This shows clearly that the multiscaling we find is a characteristic of the statistical steady state of Eqs. (5.3) and (5.4) and not of any long-lived transient.

5.5.4 Slowly-receding bifractality ?

Another possible problem was highlighted in Ref. [21] where it was proved that, in the inviscid limit, the inverse Lagrangian map of the solution of the unforced Burgers equation, decaying from an initial Brownian velocity, shows bifractality. However, numerical simulations reported in [21] with 2^{20} grid points showed substantial deviations from bifractality. These deviations receded *very slowly* as the spatial resolution was increased because of a spurious numerical effect that dramatically reduced the range of scales over which power laws could be fit reliably [21]. Fortunately this has no counterpart in our problem where the power-law behaviour of structure functions [Figs. (5.6) and (5.7)] extends over nearly three decades of r for run B1.

We have also tried fitting our data for $S_p^{\text{abs}}(r)$ by using sums of two power-law terms. This does not improve the quality of the fits we have discussed above. We believe, therefore, that the multiscaling we obtain is not an artifact of two competing power laws, a concern addressed in Ref. [23].

5.6 Consequences of multiscaling

Finally, if the multiscaling we find for structure functions is genuine, it must manifest itself in other properties [2], such as $P(s)$, the cumulative probability distribution function of shock strengths s . To estimate shock locations we look at groups of four grid points where the discretized velocity gradient changes its sign twice (they correspond to a “zig-zag” or sawtooth structure in the velocity

profile). Figure (5.18) shows a log-log plot of $P(s)$ versus s . To overcome binning errors, we have used the following rank-ordering method to obtain $P(s)$: we list all the shocks from, say, 1000 different instantaneous snapshots of the velocity. If there are M shocks, then the strongest shock is assigned the rank M , the next one rank $M - 1$, and so on. The probability $P(s)$ of having a shock of strength $\geq s$ is just the rank of s divided by M . A simple scaling argument, which we show below, predicts $P(s) \sim s^\gamma$, with $\gamma = -3$.

Let $\mathcal{N}(s)$ be the number of shocks of strength $> s$ per unit length. Scale invariance demands $\mathcal{N}(s)$ follows the power-law

$$\mathcal{N}(s) \sim s^\gamma \quad (5.36)$$

We have already shown that the *forced* Burgers equation in the limit of vanishing viscosity remains scale invariant under the scale transformation

$$x \rightarrow \lambda x, \quad t \rightarrow \lambda^{1-h} t, \quad \text{and} \quad u \rightarrow \lambda^h u, \quad (5.37)$$

with $h = -\frac{\beta}{3}$. If $\mathcal{N}(s)$ is scale invariant under Eq.(5.37),

$$\frac{\mathcal{N}(\lambda^{-h}s)}{\lambda} = \mathcal{N}(s). \quad (5.38)$$

which implies $h\gamma = -1$ or

$$\gamma = -\frac{1}{h} = \frac{3}{\beta}. \quad (5.39)$$

Hence, for $\beta = -1$, we have $\gamma = -3$. By contrast we find $\gamma = -2.7$ [Fig. (5.18)], which again suggests lack of self-similarity. But the scaling range in Fig.(5.18) is certainly not even close to the three decades of scaling we have for the structure functions. Hence it is difficult to conclude "lack of self-similarity" based solely on this evidence. To know with better precision the range of γ consistent with our data, we have subdivided the 1000 snapshots into groups of 100 each. We find the maximum and minimum values of γ , for these groups, to be -2.64 and -2.78 , respectively; a the value -3 lies well outside this range.

5.7 Conclusion

We have presented strong numerical evidence for the multiscaling of velocity structure functions in the stochastically forced Burgers equation [Eqs. (5.3) and (5.4)] with $\beta = -1$. Let us now make connections with the theory of fluid turbulence. The analogue of this problem in fluid turbulence (see Refs.([24, 25, 14, 26, 27, 16])) is called the Randomly Forced Navier–Stokes Equation (RFNSE). In the RFNSE problem the Navier–Stokes equation in d -dimensions, is forced isotropically and homogeneously by a random Gaussian force with the following statistics:

$$\langle \hat{f}_i(k_1, t_1) \hat{f}_j(k_2, t_2) \rangle = 2D_0 |k|^{4-d-y} P_{ij}(\vec{k}) \delta(t_1 - t_2) \delta(k_1 + k_2) \quad (5.40)$$

Here i, j are the Cartesian components in d dimension and $P_{ij}(\vec{k})$ the transverse projector which enforced the incompressibility condition. One-loop renormalisation-group(RG) studies of this RFNSE [14, 26, 27] yield a K41 type energy spectrum, namely,

$$E(k) \sim k^2 S_2(k) \sim k^{-5/3}, \quad (5.41)$$

if we set $d = 3$ and $y = 4$. This relation can also be reproduced by the scaling arguments outlined in Section(5.2). These RG studies have been criticised for variety of reasons such as using a large value for y in a small- y expansion and neglecting infinity of marginal operators [28, 29]. But DNS of RFNSE has provided reasonable evidence in support of the fact that the multiscaling exponents of equal-time structure functions of RFNSE are within error bars of the corresponding multiscaling exponents of Navier–Stokes equation forced only at large scales [23, 30, 31]. At present the consensus is that the multiscaling exponents ζ_p are not affected by the random force at least for $y = 4$ but a theoretical understanding of multiscaling in RFNSE is still lacking. In the Burgers model we study, the multiscaling exponents ξ_p are certainly changed by the random forc-

ing in Eq. (5.4) in contrast to the results of RFNSE although the value of $\beta = -1$ corresponds to the value of $\gamma = 4$. Our model is by far the simplest nonlinear PDE which can show such multiscaling. Thus its systematic elucidation can offer invaluable insights into the far harder problems of multiscaling in fluid and magnetohydrodynamic turbulence. An understanding of multiscaling even in this presumably simpler system is a non-trivial task. On the numerical front we need to find out the nature of fractal or multifractal clustering of the shocks.

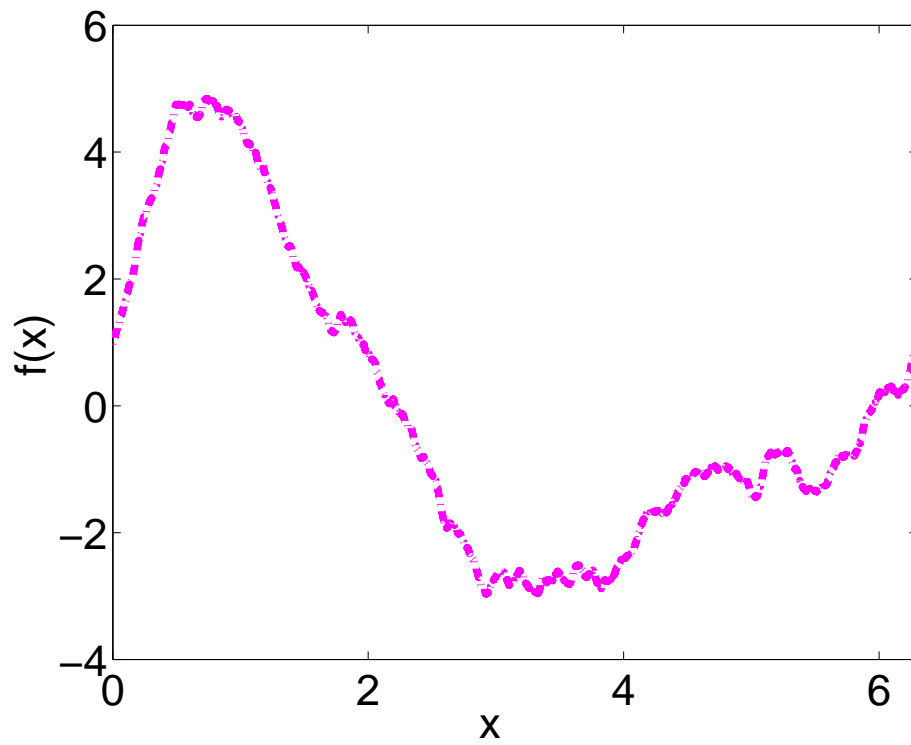


Figure 5.3: A representative plot of a snapshot of force $f = -\partial_x F$ from our run B1.

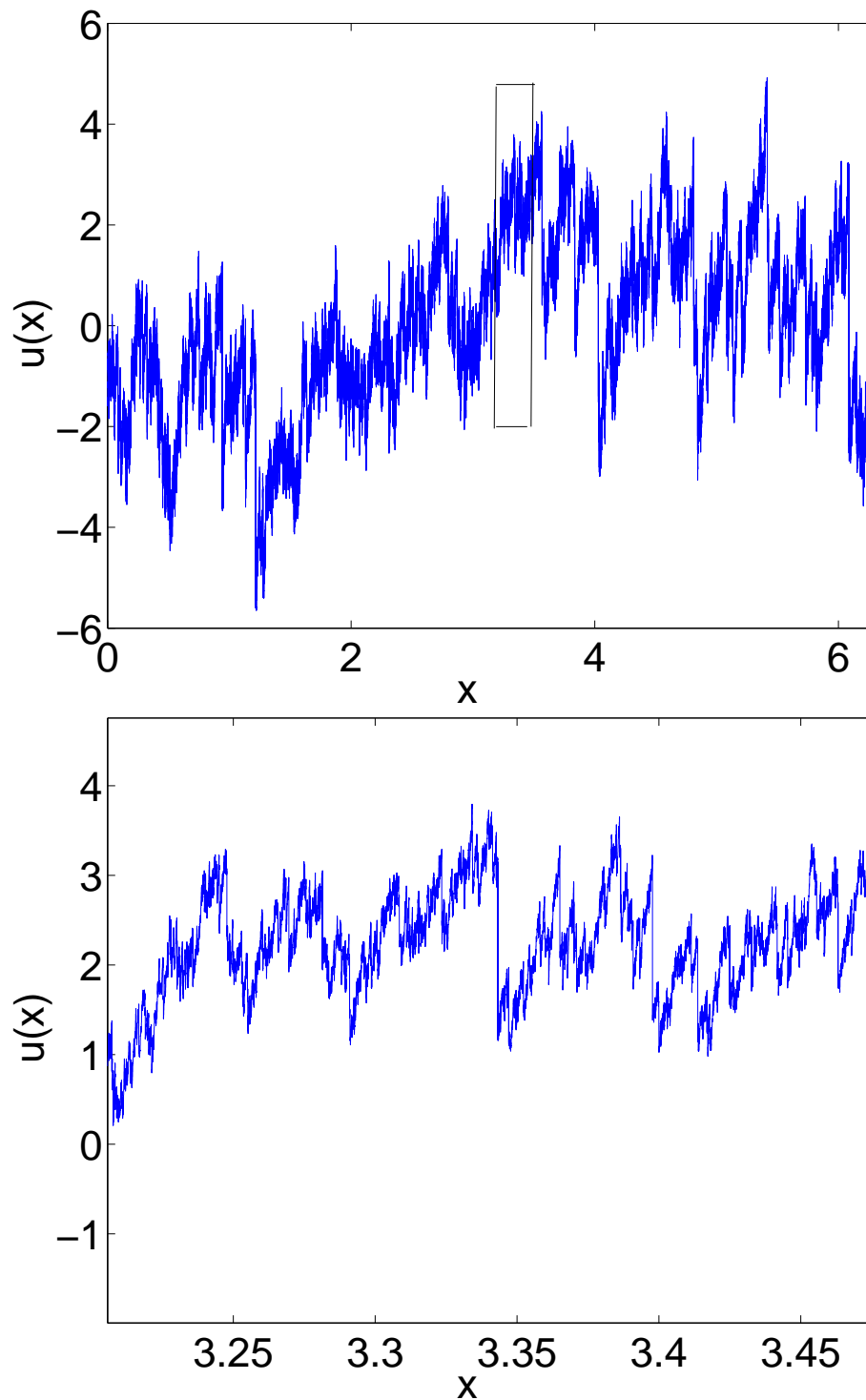


Figure 5.4: Representative snapshots of the velocity u in the statistically stationary régime (top figure); and a zoom-in view of the same velocity profile (bottom figure). The velocity develops small-scale fluctuations much stronger than those present in the force. (From our run B1)

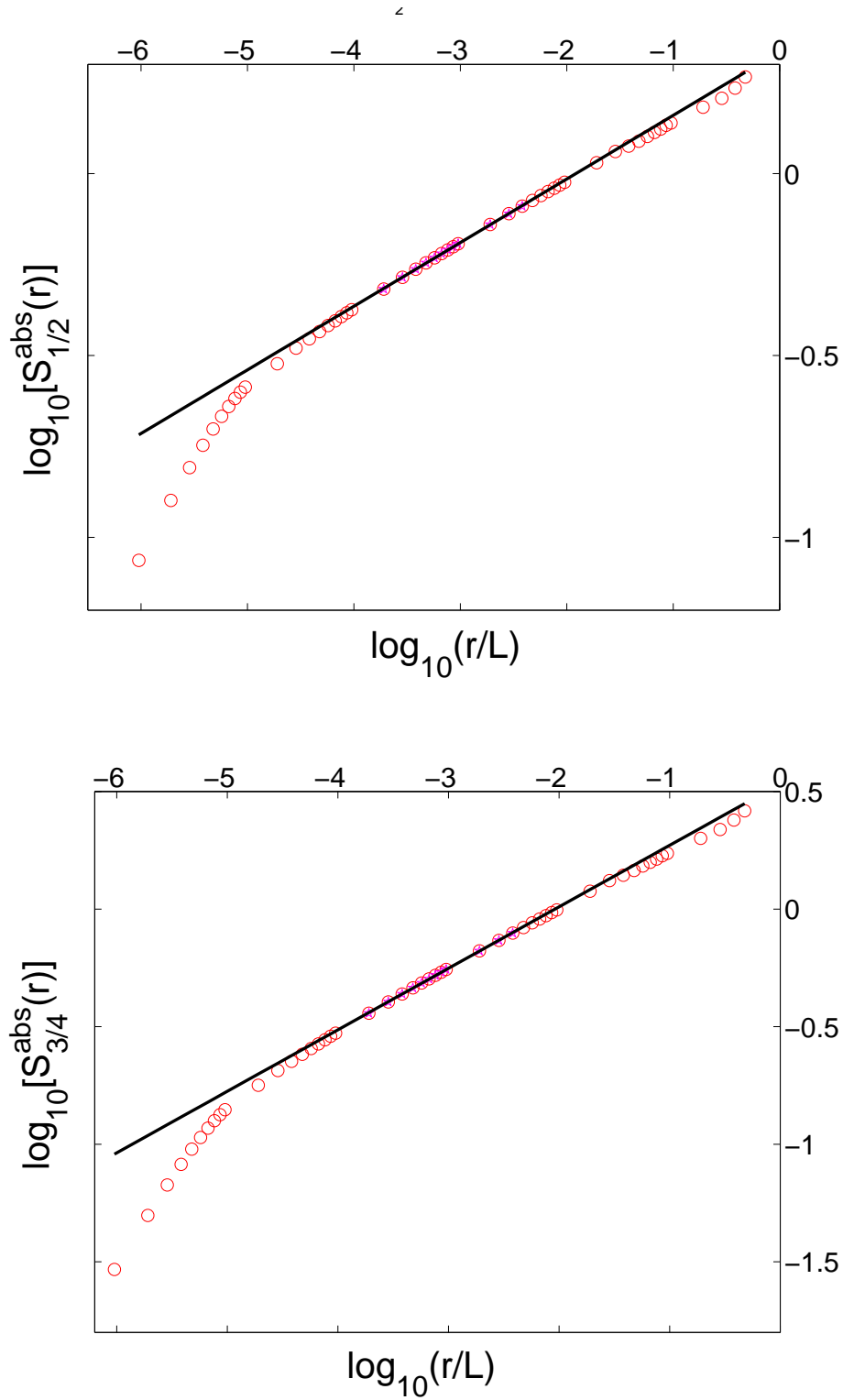


Figure 5.5: Log-log plots of the structure function $S_p^{\text{abs}}(r)$ versus r for $N = 2^{20}$ and (top) $p = 1/2$ and (bottom) $p = 3/4$. The straight line indicates the least-squares fit to the power-law régime (dark points) in the plots.(From run B1)

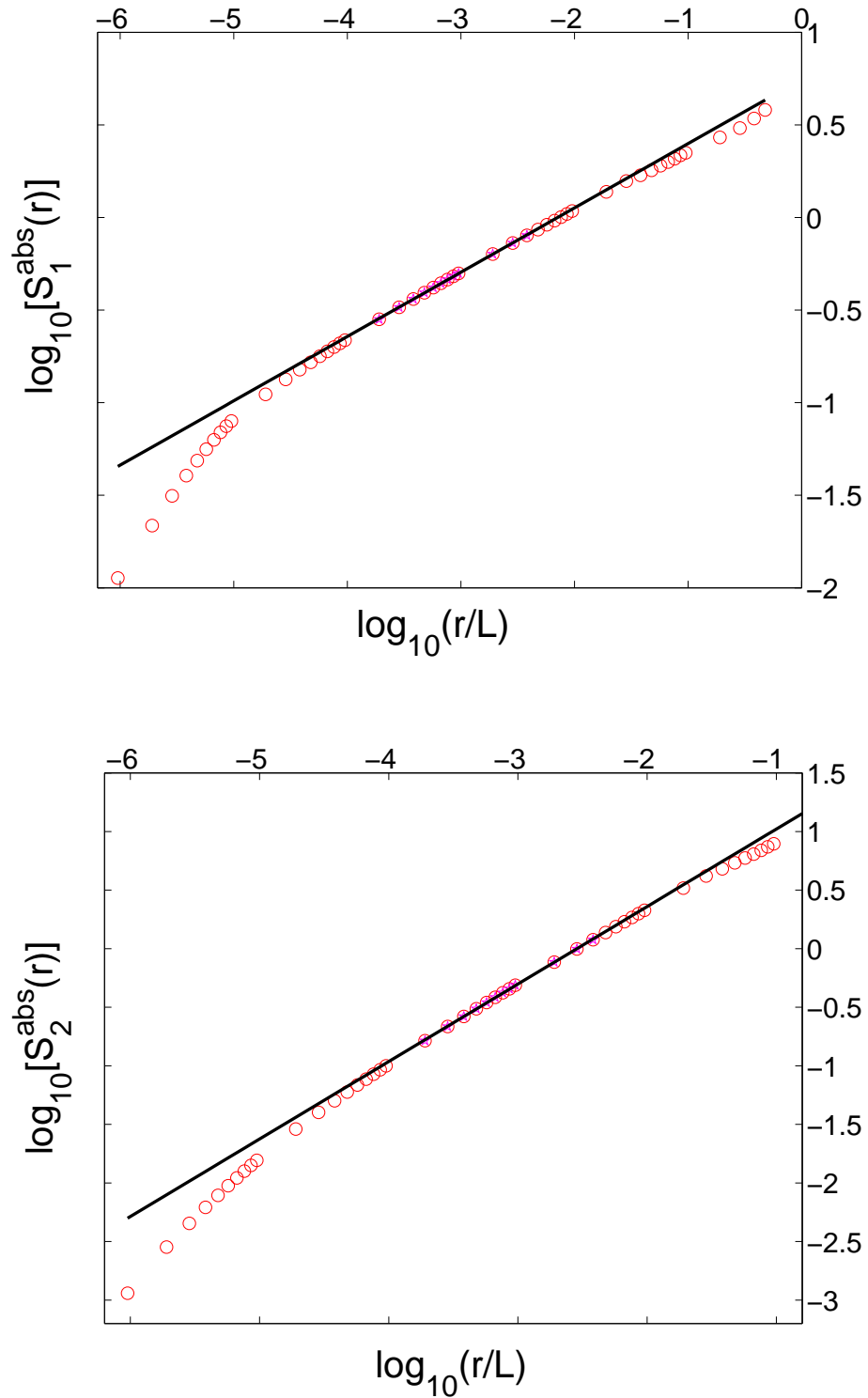


Figure 5.6: Log-log plots of the structure function $S_p^{\text{abs}}(r)$ versus r for $N = 2^{20}$ and (a) $p = 1$ and (b) $p = 2$. The straight line indicates the least-squares fit to the power-law régime (dark points) in the plots. (From run B1)

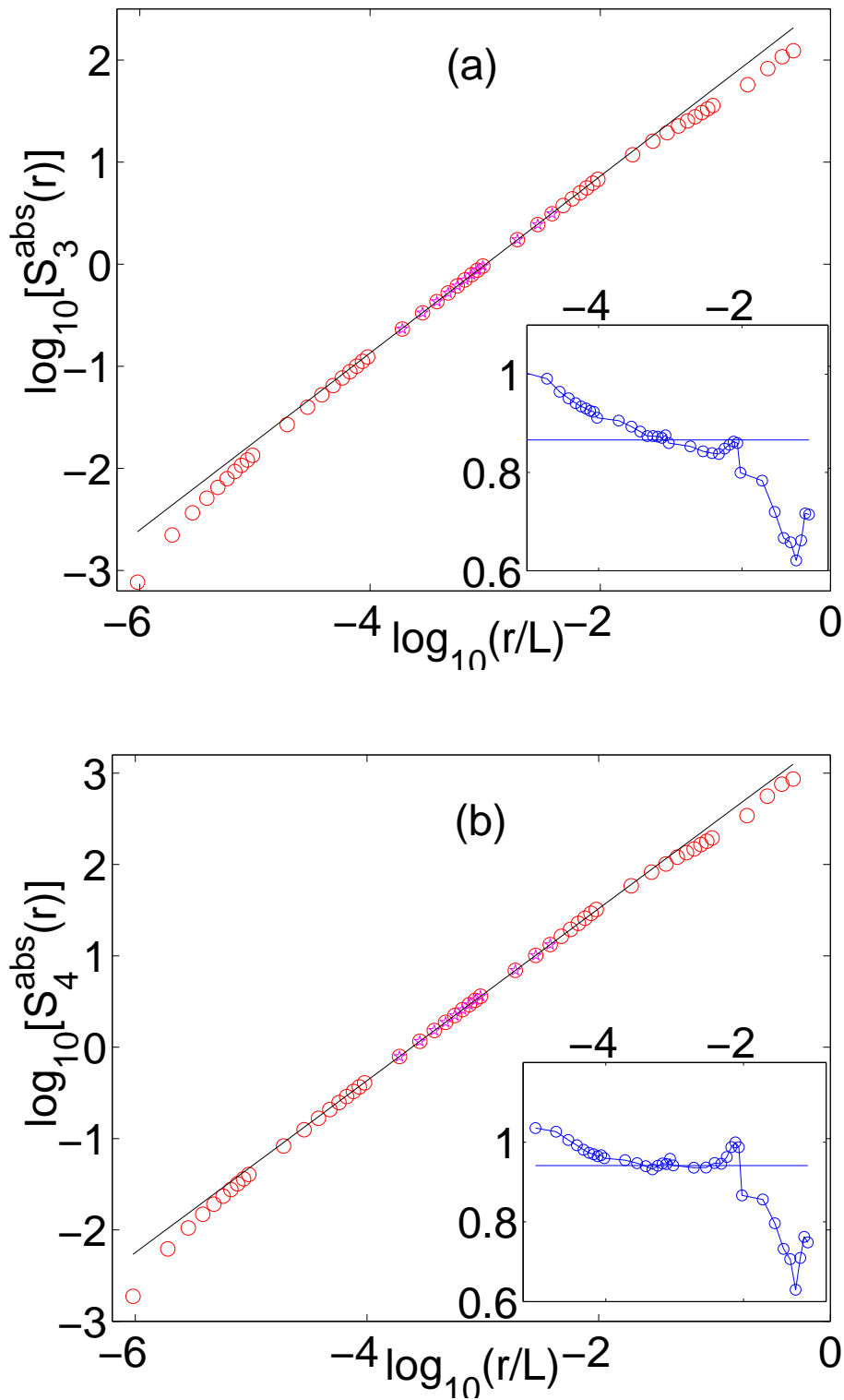


Figure 5.7: Log-log plots of the structure function $S_p^{\text{abs}}(r)$ versus r for $N = 2^{20}$ and (a) $p = 3$ and (b) $p = 4$. The straight line indicates the least-squares fit to the power-law régime (dark points) in the plots. The resulting multiscaling exponents ξ_p (see text) are shown by horizontal lines in the insets with plots of the local slopes versus r . (From run B1)

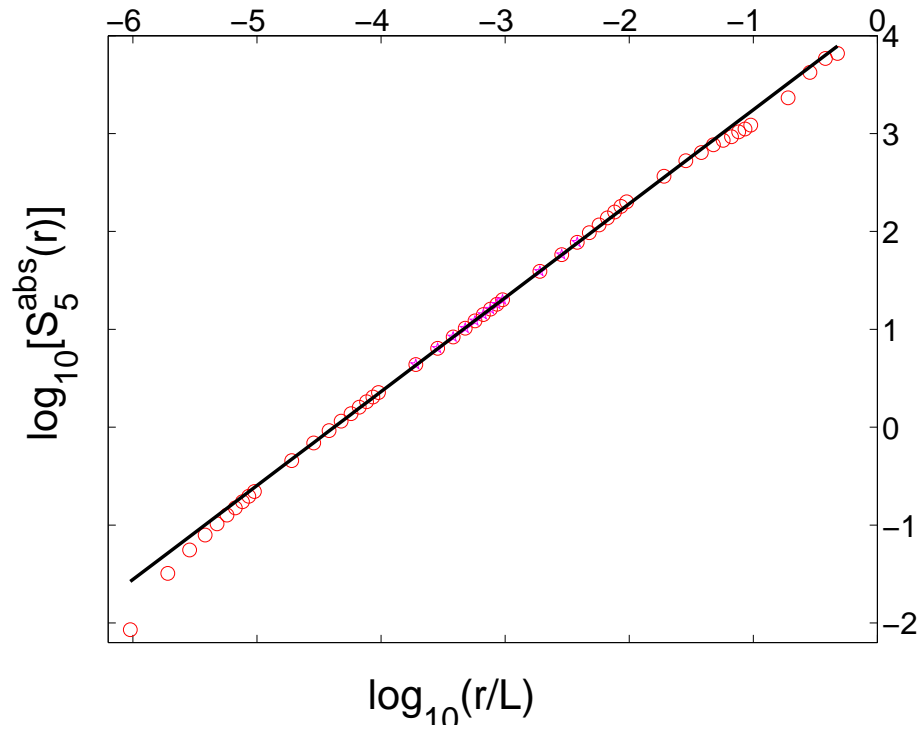


Figure 5.8: Log-log plots of the structure function $S_p^{\text{abs}}(r)$ versus r for $N = 2^{20}$ and $p = 5$. The straight line indicates the least-squares fit to the power-law régime (dark points) in the plots. (From run B1)

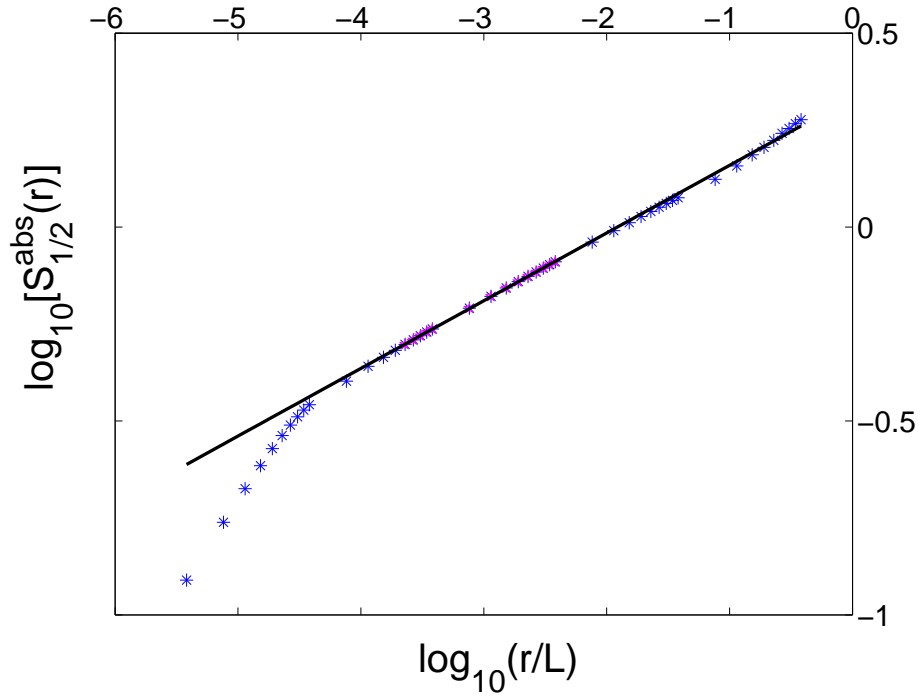


Figure 5.9: Log-log plots of the structure function $S_p^{\text{abs}}(r)$ versus r for $N = 2^{18}$ and (top) $p = 1/2$. The straight line indicates the least-squares fit to the power-law régime (dark points) in the plots.(From run B2)

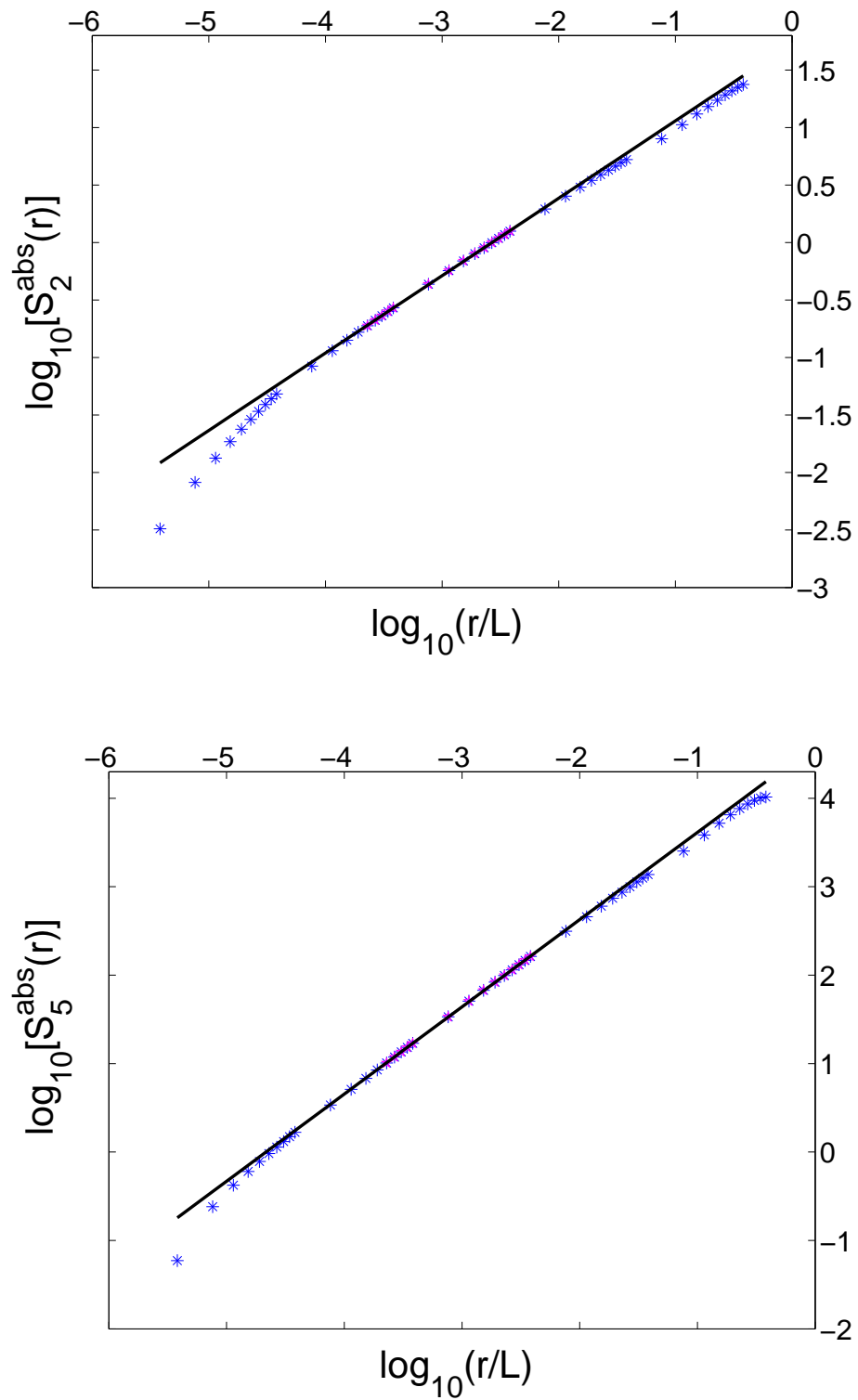


Figure 5.10: Log-log plots of the structure function $S_p^{\text{abs}}(r)$ versus r for $N = 2^{18}$ and (top) $p = 2$ and (bottom) $p = 5$. The straight line indicates the least-squares fit to the power-law régime (dark points) in the plots.

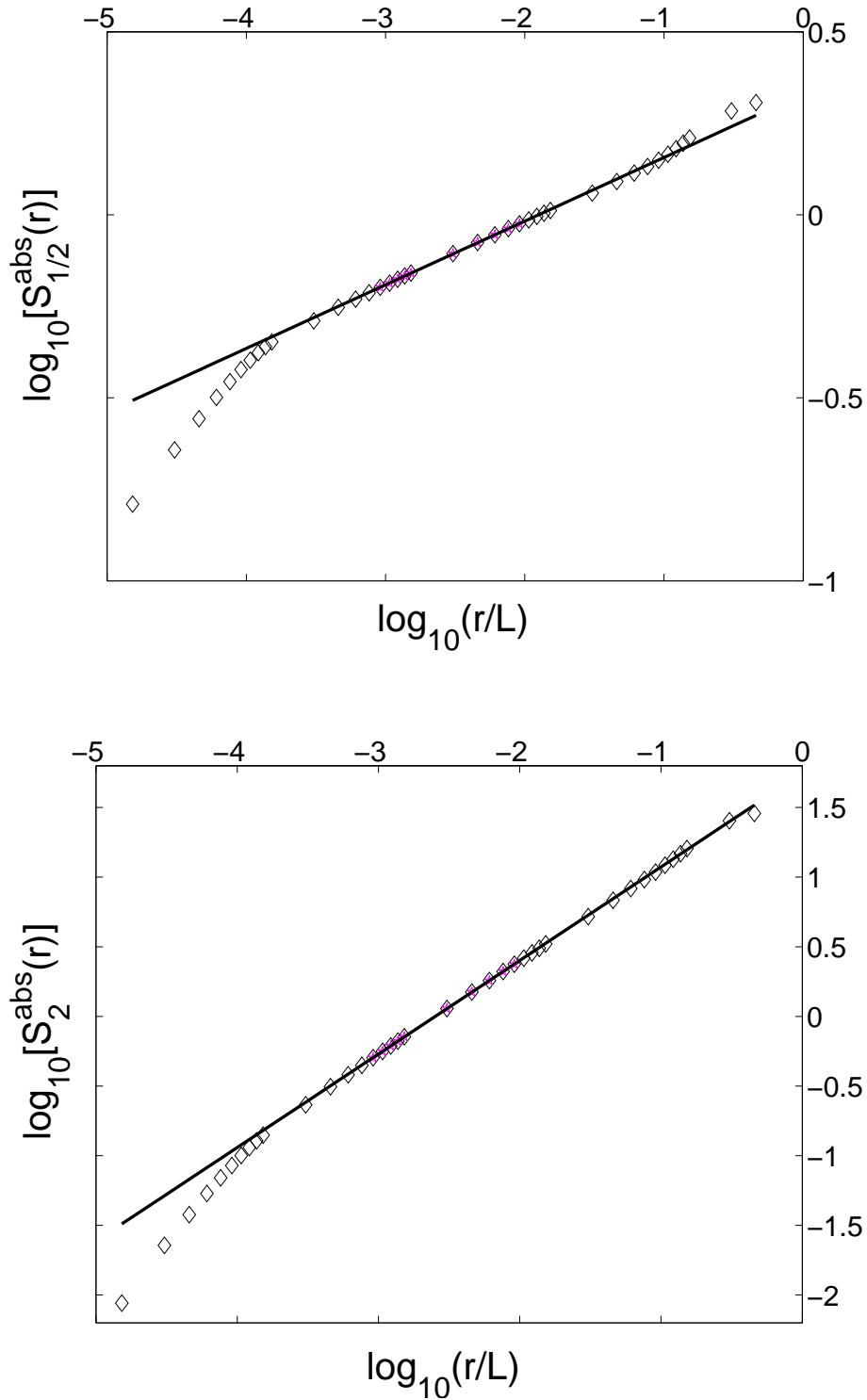


Figure 5.11: Log-log plots of the structure function $S_p^{\text{abs}}(r)$ versus r for $N = 2^{16}$ and (top) $p = 1/2$ and (bottom) $p = 2$. The straight line indicates the least-squares fit to the power-law régime (dark points) in the plots.

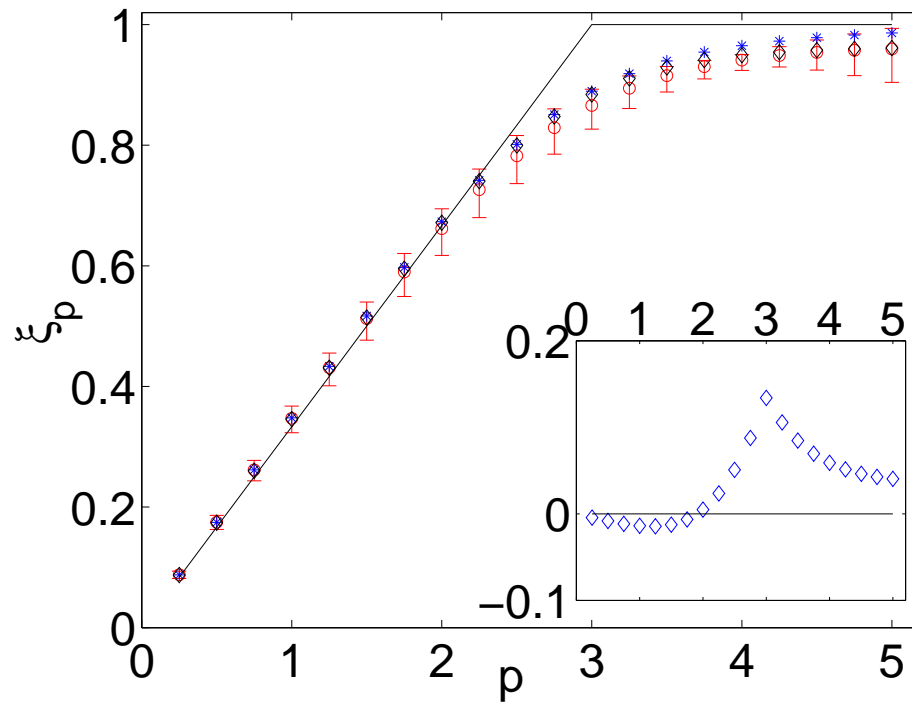


Figure 5.12: The multiscaling exponents ξ_p versus order p for Eqs. (5.3) and (5.4) with $N = 2^{16}$ (\diamond), 2^{18} ($*$), and 2^{20} (\circ) grid points. Error bars (see text) are shown for the case $N = 2^{20}$. The deviation of ξ_p from the exponents for bi-fractal scaling (full lines), shown as an inset, is a clear indication of multiscaling.

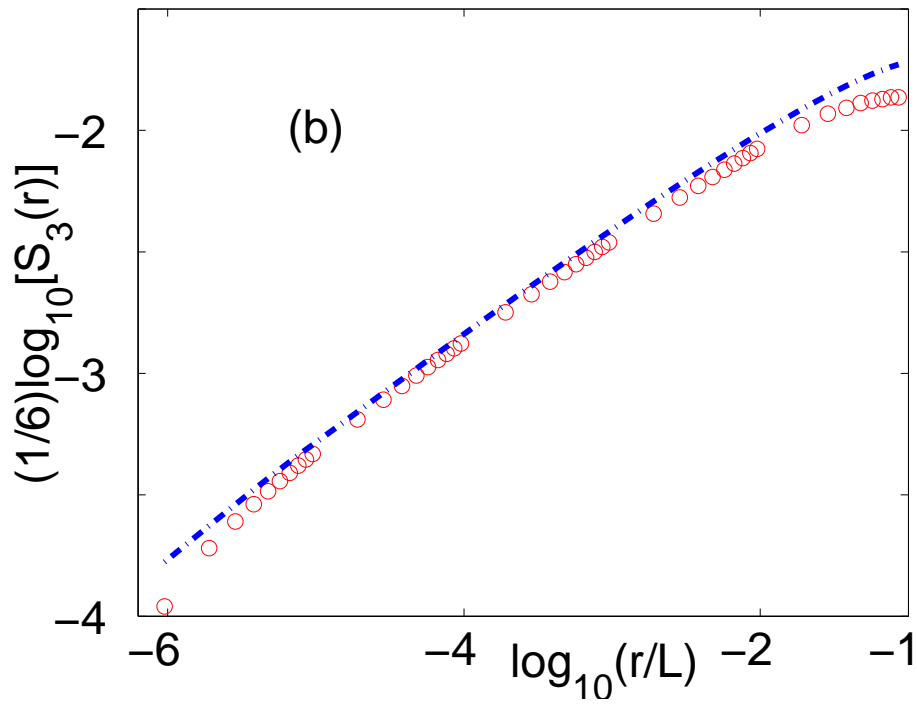


Figure 5.13: An explicit check of Eq. (5.34) from our simulations, plotted on a log-log scale. The dashed line is the right-hand side of Eq. (5.34); the left-hand side of this equation has been obtained for $N = 2^{20}$ (\circ) (run B1).

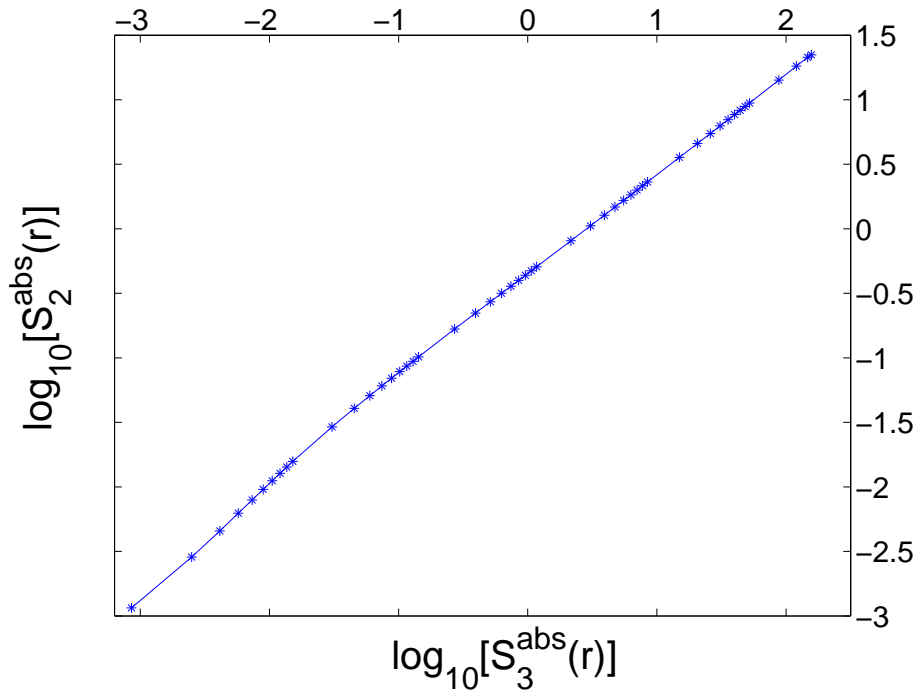


Figure 5.14: Log-log (ESS) plot of the structure function $S_2^{\text{abs}}(r)$ versus $S_3^{\text{abs}}(r)$ for $N = 2^{20}$. The scaling range in this plot is no greater than the one in Fig.(5.6).

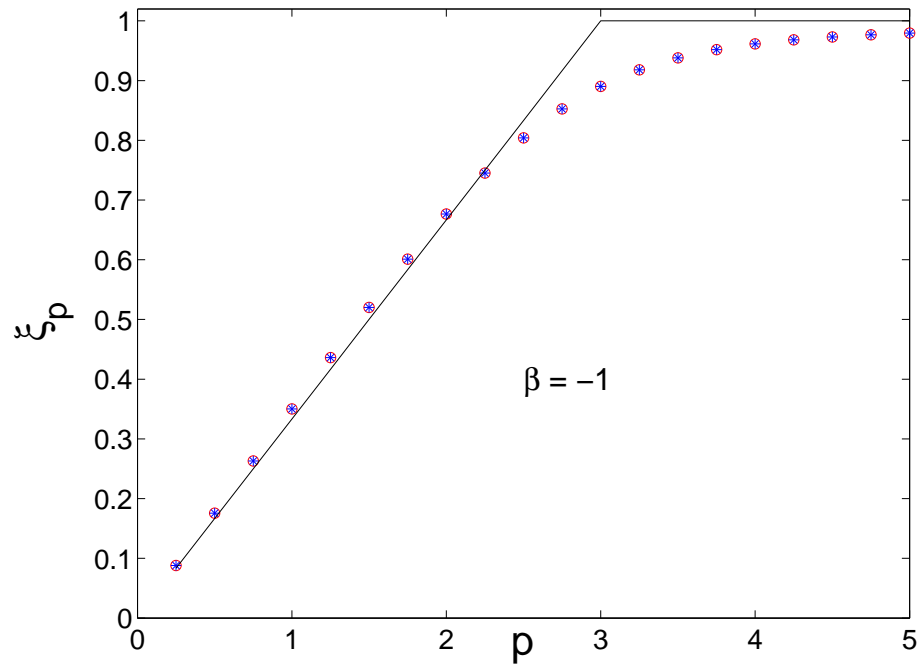


Figure 5.15: The multiscaling exponents ξ_p versus p as in Fig (5.12) (from run B1); and a plot of ξ_p versus p obtained from ESS plots. The value of ξ_3 used in the ESS plot is taken from Fig. (5.12). We use $N = 2^{20}$ grid points. The two plots are almost indistinguishable from each other, and they both clearly deviates from simple bi-fractality.

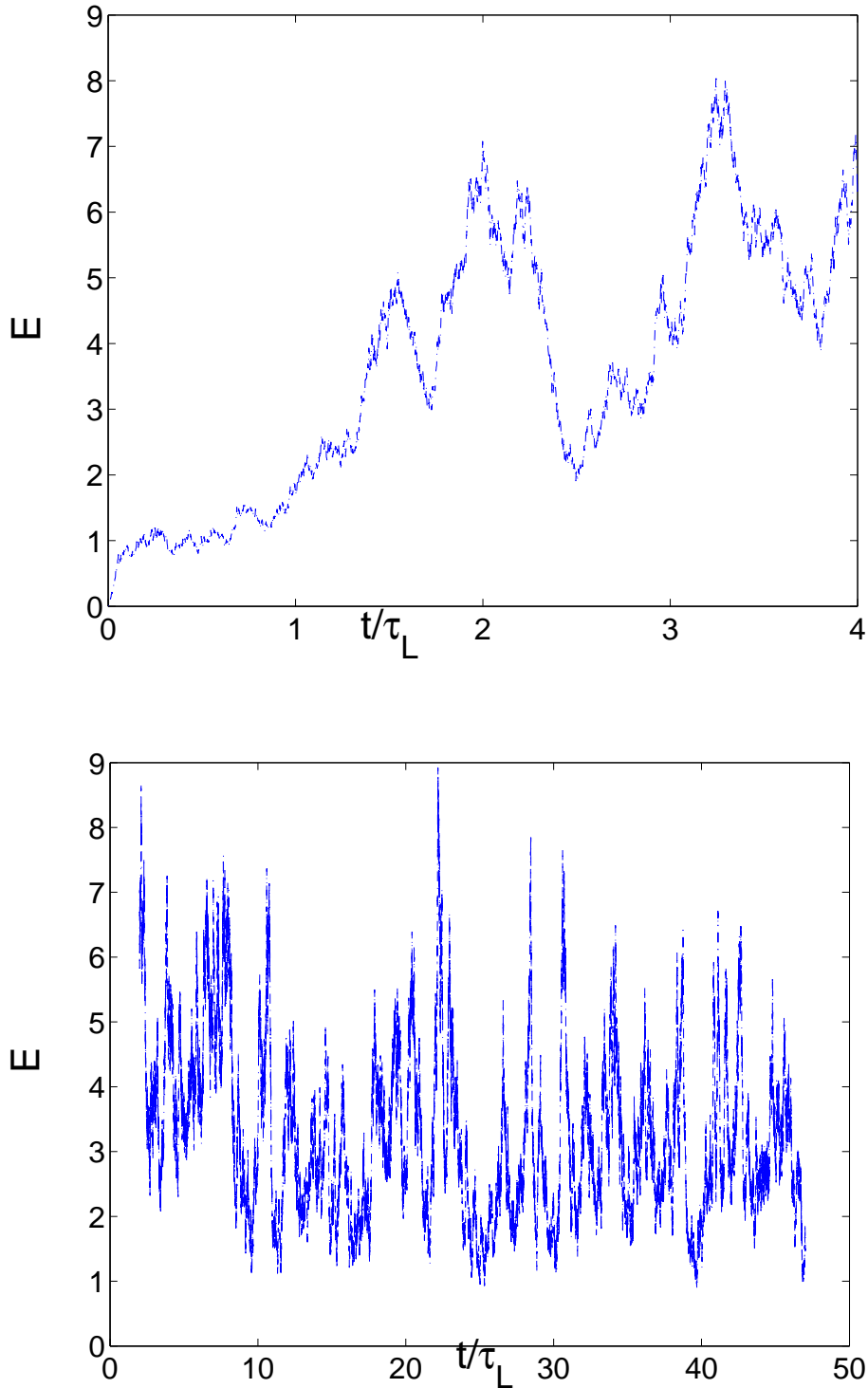


Figure 5.16: A plot of total energy of the system divided by the number of grid points [E as defined in Eq. (5.35)] as a function of time. The upper plot is for the first 4 large eddy turnover time and the lower one is for next 46 large eddy turnover time (from run B3).

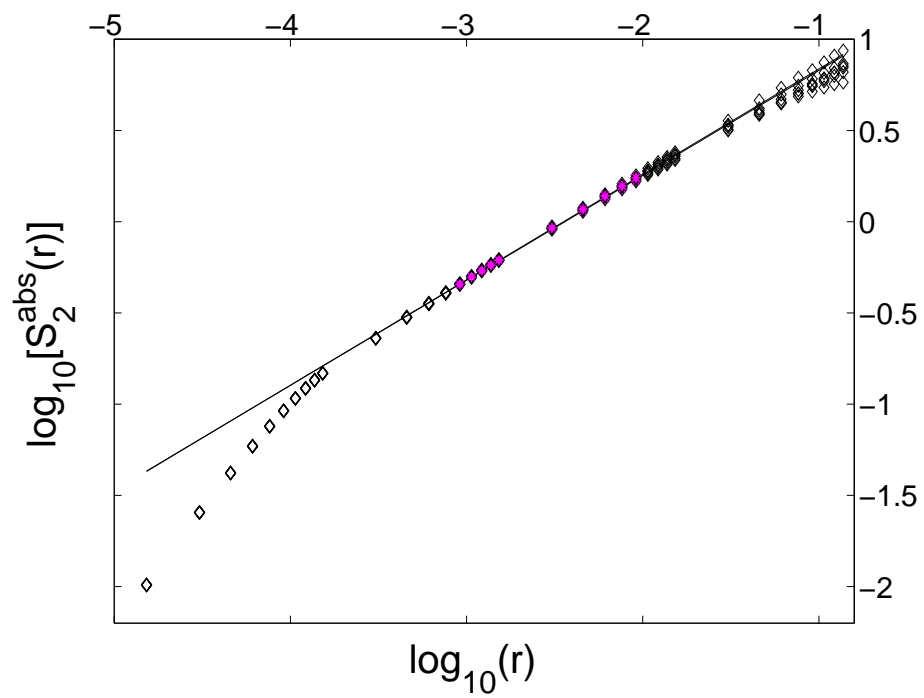


Figure 5.17: The plot of $\log_{10}[S_2^{\text{abs}}(r)]$ versus $\log_{10}(r)$ from five different runs plotted together. (From run B3)

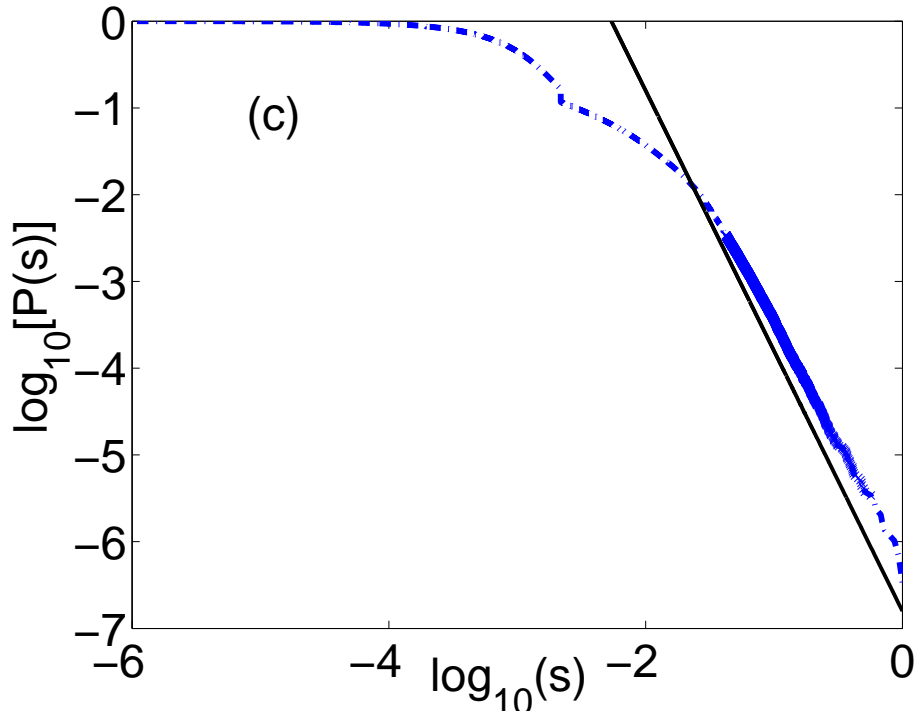


Figure 5.18: Log-log plots of the cumulative probability distribution function $P(s)$ versus shock strengths s obtained from an average over 1000 snapshots. A least-squares fit to the form $P(s) \sim s^\gamma$, for the dark points in the range $-5 \lesssim \log_{10}[P(s)] \lesssim -2.5$, yields $\gamma = -2.70$; the simple-scaling prediction $\gamma = -3$ is indicated by the straight line. By subdividing the 1000 snapshots into groups of 100 each we find the maximum and minimum values of γ , for these groups, to be -2.64 and -2.78 , respectively, which give an indication of the error in our estimate for γ .

Bibliography

- [1] A. Kolmogorov, Dokl. Acad. Nauk USSR **30**, 9 (1941).
- [2] U. Frisch, *Turbulence the legacy of A.N. Kolmogorov* (Cambridge University Press, Cambridge, 1996).
- [3] T. Ishihara, Y. Kaneda, M. Yokokawa, K. Itakura, and A. Uno, Journal of Physical Society of Japan **72**, 983 (2003).
- [4] R. Benzi, S. Ciliberto, R. Trippiccion, C. Baudet, F. Massaioli, and S. Succi, Phys. Rev E **48**, R29 (1993).
- [5] A. Cheklov and V. Yakhot, Phys. Rev. E **52**, 5681 (1995).
- [6] A. Cheklov and V. Yakhot, Phys. Rev. E **51**, R2739 (1995).
- [7] V. Yakhot and A. Cheklov, Phys. Rev. Lett **77**, 3118 (1996).
- [8] F. Hayot and C. Jayaprakash, Phys. Rev. E **56**, 4259 (1997).
- [9] F. Hayot and C. Jayaprakash, Phys. Rev. E **57**, R4867 (1998).
- [10] F. Hayot and C. Jayaprakash, Int. J. Mod. Phys. B **14**, 1781 (2000).
- [11] J. Bouchaud, M. Mézard, and G. Parisi, Phys. Rev. E **52**, 3656 (1995).
- [12] W. E, K. Khanin, A. Mazel, and Y. Sinai, Phys. Rev. Lett **78**, 1904 (1997).
- [13] J. Bec, U. Frisch, and K. Khanin, J. Fluid Mech. **416**, 239 (2000).

- [14] D. Forster, D. Nelson, and M. Stephen, *Phys. Rev. A* **16**, 732 (1977).
- [15] E. Medina, T. Hwa, M. Kardar, and Y. Zhang, *Phys. Rev. A* **39**, 3053 (1989).
- [16] V. Yakhot and Z.-S. She, *Phys. Rev. Lett* **60**, 1840 (1988).
- [17] A. Noullez and M. Vergassola, *J. Sci. Comp* **9**, 259 (1994).
- [18] U. Frisch and J. Bec, in *New Trends in Turbulence*, edited by A. Yaglom, F. David, and M. Lesieur (Springer EDP-Sciences, Les Ulis and Berlin, 2000), Vol. Les Houches Session LXXIV, pp. 341–383.
- [19] D. Knuth, *The Art of Computer Programming* (Addison Wesley Longman, Singapore, 1999), Vol. 2, pp. 184–187.
- [20] A. Kundagrami and C. Dasgupta, *Physica A* **270**, 135 (1999).
- [21] E. Aurell, U. Frisch, A. Noullez, and M. Blank, *J. Stat. Phys.* **88**, 1151 (1997).
- [22] P. Grassberger, *New J. Phys.* **4**, 17 (2002).
- [23] L. Biferale, A. Lanotte, and F. Toschi, *Phys. Rev. Lett* **92**, 094503 (2004).
- [24] S. Orszag, in *Fluid Dynamics, Les Houches*, edited by R. Balian and J. Peube (Gordon and Breach, New York, 1977), pp. 237–374.
- [25] H. Rose and P. Sulem, *J. Phys. France* **39**, 441 (1978).
- [26] C. D. Dominicis and P. Martin, *Phys. Rev. A* **19**, 419 (1979).
- [27] V. Yakhot and S. Orszag, *Phys. Rev. Lett* **57**, 1722 (1986).
- [28] C. Mou and P. Weichmann, *Phys. Rev. Lett.* **70**, 1101 (1993).
- [29] G. Eyink, *Phys. Fluids* **6**, 3063 (1994).
- [30] V. Yakhot, S. Orszag, and R. Panda, *J. Sci. Comput.* **3**, 139 (1988).

- [31] A. Sain, Manu, and R. Pandit, Phys. Rev. Lett **81**, 4377 (1998).

Appendix A

Adams-Bashforth scheme of integration

To illustrate the numerical scheme called Adam-Bashforth scheme used by us in time integration of

1. the GOY shell model equation in Chapter 2,
2. the passive-scalar shell model in Chapter 3 and
3. the Navier-Stokes equation in Chapter 4

we consider a much simpler ordinary differential equation:

$$\frac{dq}{dt} = -\alpha q + f(t) \quad (\text{A.1})$$

The following expression, is exactly true,

$$e^{\alpha(t+\delta t)} q(t + \delta t) - e^{\alpha t} q(t) = \int_t^{t+\delta t} e^{\alpha s} f(s) ds \quad (\text{A.2})$$

The slaved scheme is obtained by writing a similar equation involving $q(t)$ and $q(t - \delta t)$, and then adding them up, which yields the exact relation,

$$q(t + \delta t) = e^{-2\alpha\delta t} q(t - \delta t) + \int_{t-\delta t}^{t+\delta t} e^{-\alpha(t+\delta t-s)} f(s) ds \quad (\text{A.3})$$

and one replaces $f(s)$ under the integral by $f(t)$ to obtain the slaved frog scheme,

$$q_{n+1} = e^{-2\alpha\delta t} q_{n-1} + \frac{1 - e^{-2\alpha\delta t}}{\alpha} f_n \quad (\text{A.4})$$

The slaved-adam-bashforth will replace $f(s)$ under the integral by $(3/2)f(t) - (1/2)f(t - \delta t)$, which is the well known Adam-Bashforth approximation, giving the scheme,

$$q_{n+1} = e^{-2\alpha\delta t}q_{n-1} + \frac{1 - e^{-2\alpha\delta t}}{\alpha}[(3/2)f_n - (1/2)f_{n-1}] \quad (\text{A.5})$$

This (the slaved Adam-Bashforth scheme) will require more storage requirement than the slaved frog scheme, but is of higher order than the slaved-frog scheme. The Adam-Bashforth approximation is equivalent to approximating an integral by the well-known trapezoidal rule.

Appendix B

Numerical scheme for the Kraichnan shell model

In this appendix we discuss the numerical scheme we have used to integrate the Kraichnan-type shell model in Chapter 3. We closely follow the presentation of Ref. [1]. The Kraichnan-type shell model is a coupled stochastic differential equation (SDE). Let us first consider a simple SDE

$$\frac{dq}{dt} = \alpha q + b q \frac{dW}{dt} + \frac{dW'}{dt}. \quad (\text{B.1})$$

Here α and b are numerical constants. $u \equiv \frac{dW}{dt}$ and $f \equiv \frac{dW'}{dt}$ are the derivatives, in the sense of distributions, of two independent Brownian motion process. This implies that both u and f are random, Gaussian, white-in-time, with zero mean. The Ito SDE associated with Eq. (B.1) is [1]

$$dq = (\alpha q + \mathcal{D})dt + b q dW + dW' \quad (\text{B.2})$$

Here

$$\mathcal{D} \equiv \int_0^\infty \langle u(s)u(0) \rangle ds \quad (\text{B.3})$$

is called the drift operator. The present of this term can be understood by Gaussian integration by parts discussed in Ref. [2]. The term dW' is of order $O(\sqrt{\delta t})$.

Now let us consider the Kraichnan-type shell model equation.

$$\begin{aligned}
 \left[\frac{d}{dt} + \kappa k_m^2 \right] \theta_m(t) = & i[a_m(\theta_{m+1}^* \mathbf{u}_{m-1}^* - \theta_{m-1}^* \mathbf{u}_{m+1}^*) \\
 & + b_m(\theta_{m-1}^* \mathbf{u}_{m-2}^* + \theta_{m-2}^* \mathbf{u}_{m-1}^*) \\
 & + c_m(\theta_{m+2}^* \mathbf{u}_{m+1}^* + \theta_{m+1}^* \mathbf{u}_{m+2}^*)] \\
 & + \delta_{m,1} f(t).
 \end{aligned} \tag{B.4}$$

The correspondence between this equation and Eq. (B.1) is simple, the term $\frac{dW}{dt}$ corresponds to the coupling terms of velocity and θ . The external forcing term corresponds to $\frac{dW_f}{dt}$. The SDE associated with Eq. (B.4) is

$$\begin{aligned}
 d\theta_m(t) = & [(a_m b_{m+1} + b_m c_{m-2}) D_{m-1} + (-a_m c_{m-1} + b_{m+2} c_m) D_{m+1} \\
 & + a_{m-1} b_m D_{m-2} - a_{m+1} b_m D_{m-2} - a_{m+1} c_m D_{m+2} - \kappa k_m^2] \theta_m(t) dt \\
 & + i[a_m [\theta_{m+1}^*(t) \alpha_{m-1} dW_{m-1}^*(t) - \theta_{m-1}^* \alpha_{m+1} dW_{m+1}^*(t)] \\
 & + b_m [\theta_{m-1}^*(t) \alpha_{m-2} dW_{m-2}^*(t) + \theta_{m-2}^*(t) \alpha_{m-1} dW_{m-1}^*(t)] \\
 & + c_m [\theta_{m+2}^*(t) \alpha_{m+1} dW_{m+1}^*(t) + \theta_{m+1}^*(t) \alpha_{m+2} dW_{m+2}^*(t)]] \\
 & + \delta_{m,1} dW_f(t)
 \end{aligned} \tag{B.5}$$

Here $\alpha_m = k_m^{\xi/2}$ and $D_m = \alpha_m^2/2$; and the $W_m(t)$ s and $W_f(t)$ are independent identically distributed complex-valued Brownian motion functions, normalised in such a way that $\langle |W_m(t)|^2 \rangle = \langle |W_f(t)|^2 \rangle = t$. The weak order-one Euler scheme [1] associated with Eq. (B.5) is

$$\begin{aligned}
 \theta_m(t + \delta t) = & [(a_m b_{m+1} + b_m c_{m-2}) D_{m-1} + (-a_m c_{m-1} + b_{m+2} c_m) D_{m+1} \\
 & + a_{m-1} b_m D_{m-2} - a_{m+1} b_m D_{m-2} - a_{m+1} c_m D_{m+2} - \kappa k_m^2] \theta_m(t) \delta t \\
 & + i[a_m [\theta_{m+1}^*(t) \alpha_{m-1} \delta W_{m-1}^*(t) - \theta_{m-1}^* \alpha_{m+1} \delta W_{m+1}^*(t)] \\
 & + b_m [\theta_{m-1}^*(t) \alpha_{m-2} \delta W_{m-2}^*(t) + \theta_{m-2}^*(t) \alpha_{m-1} \delta W_{m-1}^*(t)] \\
 & + c_m [\theta_{m+2}^*(t) \alpha_{m+1} \delta W_{m+1}^*(t) + \theta_{m+1}^*(t) \alpha_{m+2} \delta W_{m+2}^*(t)]] \\
 & + f \delta_{m,1} \delta W_f(t)
 \end{aligned} \tag{B.6}$$

where $\delta W_m(t) = \sqrt{t} \eta_m(t)$. The $\eta_m(t)$ are independent identically distributed complex random variables of the form $a + ib$, where a and b are independent

Gaussian variables with value $\pm\sqrt{1/2}$.

Bibliography

- [1] A. Wirth and L. Biferale, *Phys. Rev. E* **54**, 4928 (1996).
- [2] U. Frisch *Turbulence, the legach of A.N. Kolmogorov* (Cambridge University Press, Cambridge, 1996).

Appendix C

Gaussian averaging of stochastic differential equations

Let us first consider a simple Stochastic Differential Equation (SDE) for a N component vector q_i , $i = 1, \dots, N$:

$$\partial_t q_i = g_i(\vec{q})u_i + f_i \quad (\text{C.1})$$

Here u_i and f_i are two independently distributed Gaussian noise, with the following covariance:

$$\langle u_i(t)u_j(t') \rangle = D_{ij}^u \delta(t - t') \quad (\text{C.2})$$

$$\langle f_i(t)f_j(t') \rangle = D_{ij}^f \delta(t - t') \quad (\text{C.3})$$

$$\langle u_i(t)f_j(t') \rangle = 0 \quad (\text{C.4})$$

We want to calculate the equation of motion for

$$C_{ij} = \langle q_i(t)q_j(t) \rangle \quad (\text{C.5})$$

Here the symbol $\langle \cdot \rangle$ implies averaging over the probability distribution of u and f . Hence,

$$\frac{d}{dt} C_{ij} = \left\langle \frac{dq_i}{dt} q_j \right\rangle + \left\langle q_i \frac{dq_j}{dt} \right\rangle \quad (\text{C.6})$$

$$= \left\langle \frac{dq_i}{dt} q_j \right\rangle + (i \rightarrow j) \quad (\text{C.7})$$

$$= \langle q_j \{u_i g_i(\vec{q}) + f_i\} \rangle + (i \rightarrow j) \quad (\text{C.8})$$

$$= [\langle q_j g_i(\vec{q}) u_i \rangle + \langle q_j f_i \rangle] + [i \rightarrow j]. \quad (\text{C.9})$$

Here the symbol $(i \rightarrow j)$ means; we have to first calculate the first term in the equation, and then exchange the i indices to j and vice versa to obtain the second term.

We have to calculate the an average of the form $\langle A[f, u]u_i \rangle$. Here $A[f]$ is a functinal of \vec{f} and \vec{u} . Novikov's theorem states that, if \vec{f} and \vec{u} are random and Gaussian, then:

$$\begin{aligned} \langle A[f, u]u_i \rangle &= \int_0^\infty \left[\langle u_i(t)u_j(t') \rangle \left\langle \frac{\delta}{\delta u_j(t')} A[f, u] \right\rangle \right. \\ &\quad + \langle f_i(t)f_j(t') \rangle \left\langle \frac{\delta}{\delta f_j(t')} A[f, u] \right\rangle \\ &\quad + \langle u_i(t)f_j(t') \rangle \left\langle \frac{\delta}{\delta f_j(t')} A[f, u] \right\rangle \\ &\quad \left. + \langle f_i(t)u_j(t') \rangle \left\langle \frac{\delta}{\delta u_j(t')} A[f, u] \right\rangle \right] dt' \end{aligned} \quad (C.10)$$

$$= D_{ij}^u \left\langle \frac{\delta}{\delta u_j(t)} A[f, u] \right\rangle + D_{ij}^f \left\langle \frac{\delta}{\delta f_j(t)} A[f, u] \right\rangle \quad (C.11)$$

Here the repeated indices are to be summed over. For a proof see Ref. [1]. We have used Eqs. (C.2-C.4) to obtain Eq. (C.11) from Eq. (C.10). The time integral on the RHS of Eq. (C.10) simplifies due to the white-in-time nature u and f . Now to evaluate the first term in Eq. (C.9) use $A[f, u] = g_i[\vec{q}]q_j$. Next we have to evaluate the functional derivatives. The method we use is well-known, see, e.g. page 69 of Ref.[1]. First we formally integrate the Eq. (C.1) to obtain:

$$q_i(t) = q_i(0) + \int_0^t dt_1 u_i(t_1) g_i[\vec{q}(t_1)] dt_1 + \int_0^t dt_1 f_i(t_1) dt_1 \quad (C.12)$$

Hence,

$$\frac{\delta}{\delta u_i(t')} q_i(t) = \int_{t'}^t \left\{ g_i[\vec{q}(t_1)] + u_i(t_1) \frac{\delta}{\delta u_i(t')} g_i[\vec{q}(t_1)] \right\} dt_1 \quad (C.13)$$

We shall need the above functional derivative only for $t = t'$. Taking this limit in Eq. (C.13), [see Ref. [1] page 69-70], we obtain:

$$\frac{\delta}{\delta u_i(t)} q_i(t) = g_i[\vec{q}(t)]. \quad (C.14)$$

The second term in Eq. (C.9) yields,

$$\langle q_j f_i \rangle = D_{ik}^f \left\langle \frac{\delta q_j}{\delta f_k} \right\rangle \quad (C.15)$$

$$= D_{ik}^f (1/2) \delta_{jk} \quad (C.16)$$

$$= \frac{1}{2} D_{ij}^f \quad (C.17)$$

Putting all the pieces together we have

$$\frac{d}{dt} C_{ij} = \left[D_{ik}^u \left\langle q_j \frac{\delta g_i}{\delta u_k} \right\rangle + D_{ij}^u \langle g_i g_j \rangle + \frac{1}{2} D_{ij}^f \right] + [i \rightarrow j] \quad (C.18)$$

Similar equations, that has been written down in Chapter 3 for a variety of stochastic models, v.i.z the Kraichnan shell model, Kraichnan passive-scalar advection-diffusion equation, and the Kraichnan passive-vector equation, can be derived in exactly the same way.

In Chapter 3 we have also calculated equation-of-motion of different dynamic correlators, whose analogue for the simple SDE considered in this Appendix is :

$$F_{ij}(t) \equiv \langle q_i(t) q_j(0) \rangle \quad (C.19)$$

Proceeding in the way outlined above we observe that the equation-of-motion of F_{ij} differs from that of C_{ij} in the following way:

1. The second term of Eq. (C.6) is zero.
2. Assuming causality is valid for Eq. (C.1) one can show that the second and third term in Eq. (C.18) is also zero.

Hence we have

$$\frac{d}{dt} F_{ij}(t) = D_{ik} \left\langle q_j \frac{\delta g_i}{\delta u_k} \right\rangle \quad (C.20)$$

Bibliography

[1] J. Zinn-Justin, *Quantum Field Theory and Critical Phenomenon* (Oxford University Press, Oxford, 1999).

Appendix D

Von Kármán–Howarth relation in Kicked “Burgulence”

For notational convenience in this section we assume 1-periodicity in space. Space averages over the period are denoted $\langle \cdot \rangle_x$. Averages over both space and time are denoted $\langle \cdot \rangle$.

$$\frac{1}{6}S_3(r) = - \int_0^r G(y) dy, \quad (\text{D.1})$$

where $G(y)$ is the spatial part of the force correlation function, defined by $\langle f(x+y, t')f(x, t) \rangle = G(y)\delta(t-t')$. Our proof follows closely the proof of analyticity of third order structure function in Ref. [1], where the external force is not random and limited to large spatial scales.

This will be established as a consequence of the following relation for the unforced Burgers equation with space-periodic solution in the limit of vanishing viscosity. Let $u \equiv u(x, t)$ and $u' \equiv u(x + \Delta x, t)$, we have

$$\partial_t \langle u'u \rangle_x = \frac{1}{6} \partial_{\Delta x} \langle (u' - u)^3 \rangle_x. \quad (\text{D.2})$$

It is here assumed that Δx is not an integer multiple of the spatial period and that no pair of shocks remains separated by exactly Δx for a finite amount of time (this holds for almost every Δx).

Proof. Let us denote by $X_i(t)$ ($i = 1, \dots, N(t)$) the (Eulerian) ordered positions of shocks and by $[u]_i \equiv u(X_i(t)_+, t) - u(X_i(t)_-, t)$ the (negative) velocity jump at the

i -th shock. ($N(t)$ may change in time.) Except at shocks we can use the inviscid Burgers equation $\partial_t u + u \partial_x u = 0$. At shocks this has to be supplemented by the Rankine–Hugoniot conditions (see, e.g. Ref. [1])

$$\dot{X}_i[u]_i - \llbracket \frac{u^2}{2} \rrbracket_i = 0, \quad (D.3)$$

which follow also from momentum conservation applied to small intervals straddling the shocks. An immediate consequence is that the velocity of the shocks are given by

$$\dot{X}_i(t) = \frac{1}{2} [u(X_i(t)_+, t) + u(X_i(t)_-, t)]. \quad (D.4)$$

We observe that

$$\langle u'u \rangle_x = \sum_{i=1}^N \int_{X_i(t)}^{X_{i+1}(t)} u'u \, dx, \quad (D.5)$$

where $X_{N+1}(t) \equiv X_1(t) + 1$. Differentiating with respect to t , we obtain

$$\partial_t \langle u'u \rangle_x = \langle u \partial_t u' + u' \partial_t u \rangle_x - \sum_{i=1}^N \dot{X}_i(t) \llbracket u \rrbracket_i u(X_i(t) + \Delta x, t) \quad (D.6)$$

$$= - \sum_{i=1}^N \int_{X_i(t)}^{X_{i+1}(t)} (uu' \partial_x u' + u'u \partial_x u) \, dx - \sum_{i=1}^N \dot{X}_i(t) \llbracket u \rrbracket_i u(X_i(t) + \Delta x, t) \quad (D.7)$$

$$= - \sum_{i=1}^N \int_{X_i(t)}^{X_{i+1}(t)} \left(\frac{1}{2} u \partial_{\Delta x} u'^2 - \frac{1}{2} u^2 \partial_{\Delta x} u' \right) \, dx - \sum_{i=1}^N \dot{X}_i(t) \llbracket u \rrbracket_i u(X_i(t) + \Delta x, t) + \sum_{i=1}^N \llbracket \frac{u^2}{2} \rrbracket_i u(X_i(t) + \Delta x, t). \quad (D.8)$$

In going from (D.6) to (D.7) we used the inviscid decaying Burgers equation; from (D.7) to (D.8) we have performed an integration by parts and used $\partial_x u' = \partial_{\Delta x} u'$. From (D.3) follows that the last two terms in (D.8) cancel. Hence, we obtain

$$\partial_t \langle u'u \rangle_x = \frac{1}{2} \partial_{\Delta x} \langle -uu'^2 + u^2 u' \rangle_x = \frac{1}{6} \partial_{\Delta x} \langle (u' - u)^3 \rangle_x, \quad (D.9)$$

which completes the proof.

We now return to the case of the periodically kicked Burgers equation. We assume that the solution $u(x, t)$ reaches a steady state and hence the right-hand-side (RHS) of Eq. (D.2) is constant in time. Then integrating (D.2) time between two successive kicks, say at $t = 0$ and $t = 1$, we have

$$\begin{aligned} \frac{1}{6}\partial_{\Delta x}S_3(\Delta x) &= \frac{1}{6}\partial_{\Delta x}\langle [u(x + \Delta x, t) - u(x, t)]^3 \rangle \\ &= \langle u(x + \Delta x, 1_-)u(x, 1_-) \rangle_x - \langle u(x + \Delta x, 0_+)u(x, 0_+) \rangle_x. \end{aligned} \quad (\text{D.10})$$

Next, we use

$$u(x, 0_+) = u(x, 0_-) + f(x). \quad (\text{D.11})$$

Here $f(x)$ is the external kick. Hence, we have

$$\begin{aligned} \frac{1}{6}\partial_{\Delta x}S_3(\Delta x) &= \langle u(x + \Delta x, 1_-)u(x, 1_-) \rangle_x - \langle u(x + \Delta x, 0_-)u(x, 0_-) \rangle \\ &\quad - \langle f(x + \Delta x)f(x) \rangle \\ &\quad - \langle u(x + \Delta x, 0_-)f(x) \rangle - \langle u(x, 0_-)f(x + \Delta x) \rangle \end{aligned} \quad (\text{D.12})$$

In RHS of Eq. (D.12) the two terms on the first line cancel each other if we assume that we have reached statistical steady state. The two terms on the last line are zero by causality. Hence we have

$$\frac{1}{6}\partial_{\Delta x}S_3(\Delta x) = -\langle f(x + \Delta x)f(x) \rangle \quad (\text{D.13})$$

Bibliography

- [1] J. Bec, U. Frisch, and K. Khanin, *J. Fluid Mech.* **416**, 239 (2000).